Molecular Beam Epitaxial Growth, Characterization, and Nanophotonic Device Applications of InN Nanowires on Si Platform

Songrui Zhao

Department of Electrical and Computer Engineering
Faculty of Engineering
McGill University, Montreal

April 2013

A thesis submitted to McGill University in partial fulfillment of the requirements
of
the degree of Doctor of Philosophy

To my wife, Rubing

Table of Contents

Acknowledgement

This doctoral dissertation is a great teamwork, which would have never happened without the help from each individual that played a significant role in completing this work successfully. Here I am sincerely grateful to every individual who was involved in this work.

My advisor, Prof. Zetian Mi, has provided tremendous support during my PhD study from nearly every aspect of my life to the research; and most impressively, he is available almost 24/7 for discussions about my projects, to come up with new ideas, to solve problems, and to plan the next steps. Without his help I would have never made such big progress in the two years. I would also like to express my appreciation to Prof. Ishiang Shih and Prof. Vamsy P. Chodavarapu for their thought-provoking questions during the PhD exam, as well as the suggestion and evaluation for my research.

During the two years of study at McGill University, my lab mates helped me a lot as well, to whom I am greatly indebted. Here I sincerely list their names below: Dr. S. Fathololoumi, Dr. Q. Wang, Dr. B. Wu, Dr. K. Cui, Dr. H. P. T. Nguyen, Dr. D. Wang, Dr. S. Arafin, Dr. M. Harati, M. G. Kibria, X. Han, Y. Li, C. Shao, B. Le Huy, A. Shih, S. Mukherjee, M. H. T. Dastjerdi, M. Djavid, S. Fan, B. Alotaibi, S. Zhang, S. Sadaf, A. Connie, M. F. A. Chowdhury, and X. Liu. Special thanks goes to A. Shih for his help in translating the abstract into French.

Besides the help from my lab mates, amazing input to this work comes from our collaborators that include Prof. K. H. Bevan, Dr. D. Liu, Prof. H. Guo, T. Gonzalez, and Prof. M. Andrews at McGill University; Q. Li and G. T. Wang at the Sandia National Laboratories; O. Salehzadeh, S. Alagha, Prof. K. Kavanagh, and Prof. S. Watkins at Simon Fraser University.

I am also very grateful to Prof. T. Szkopek for the discussions about field effect transistor measurements, and Dr. J. Lefebvre at Université de Montréal for the discussions about XPS experiments, as well as the supporting staff from McGill Nanotools Microfab, XPS, SEM, and TEM facilities for their generous assistance.

Additionally, I would like to acknowledge the thesis defense committee, which includes Prof. C. Rowe, Prof. R. Khazaka, Prof. Z. Mi, Prof. K. H. Bevan, Prof. T. Szkopek, and Prof. G. Gervais, for the valuable suggestions and comments about the thesis work, as well as Prof. K. H. Bevan and Prof. Z. Wasilewski for serving as the internal and external thesis examiners.

Last but not least, I would like to thank all my friends, my family, and especially my wife, for her encouragement, unconditional support, and love.

This work is supported by the Natural Sciences and Engineering Research Council of Canada (NSERC), the Fonds de recherché sur la nature et les technologies, Canada Foundation for Innovation, US Army Research Office, and the Hydro-Quebec Nano-Engineering Program at McGill University.

Contribution of Authors

This dissertation work includes the contribution from the candidate and many other individuals. The candidate and his advisor, Prof. Zetian Mi, defined the project, and worked closely on the discussions and manuscript writings. The candidate performed the InN nanowire growth, as well as the PL measurements. Some of the PL setup alignments were contributed by Dr. Saeed Fathololoumi. For the XPS experiments, some were performed by Qiming Li and G. T. Wang at the Sandia National Laboratories, US; some were helped with Md Golam Kibria, and the rest were performed by the candidate. Some of the Raman experiments were performed by the candidate together with Dr. Qi Wang and Timothy Gonzalez at the Department of Chemistry, McGill University; and the equipment was provided by Prof. Mark Andrews at the Department of Chemistry, McGill University. The nanoprobing to individual InN nanowires was performed by the candidate together with Omid Salehzadeh and Shima Alagha at the 4D LABS, Simon Fraser University; and Prof. Karen Kavanagh and Prof. Simon Watkins from Simon Fraser University contributed to the discussions of the results. The single nanowire field effect transistor experiments were carried out by the candidate and B. Le Huy, and Prof. T. Szkopek contributed to the discussions about the measurements. The theoretical calculation was performed by Prof. Kirk H. Bevan at the Department of Mining and Materials Engineering, and Dr. Dongping Liu and Prof. Hong Guo at the Department of Physics, McGill University.

List of Figures

List of Acronyms

2DEG	Two-Dimensional Electron Gas
CBE	Chemical Beam Epitaxy
CBM	Conduction Band Minimum
CNL	Charge Neutrality Level
CVD	Chemical Vapor Deposition
DOS	Density of States
ECV	Electrolyte-based Capacitance Voltage
FWHM	Full Width at Half Maximum
IQE	Internal Quantum Efficiency
IR	Infrared
LD	Laser Diode
LED	Light Emitting Diode
LO	Longitudinal Optical
MBE	Molecular Beam Epitaxy
PI	Polyimide
PL	Photoluminescence
PSB	Phonon Sideband Emission
RF	Radio Frequency
RIE	Reactive-Ion Etching
SAG	Selective Area Growth
SCL	Space Charge Limited
SEM	Scanning Electron Microscopy
SIMS	Secondary Ion Mass Spectroscopy
SPEM/S	Scanning Photoelectron Microscopy and Spectroscopy
TEM	Transmission Electron Microscopy
UV	Ultraviolet
VBM	Valence Band Maximum
VLS	Vapor-Liquid-Solid
VPE	Vapor Phase Epitaxy
XPS	X-ray Photoelectron Spectroscopy

Abstract

Dislocation-free semiconductor nanowires are an extremely promising route towards compound semiconductor integration with silicon technology. However, precise control over nanowire doping, together with the surface charge properties, has remained a near-universal material challenge to date. In this regard, we have investigated the molecular beam epitaxial growth and the correlated surface electrical and optical properties of InN nanowires, a promising candidate for future ultrahigh-speed nanoscale electronic and photonic devices and systems, on Si platform.

By dramatically improving the epitaxial growth process, intrinsic InN nanowires are achieved, for the *first* time, both within the bulk and on the *non-polar* InN surfaces. The near-surface Femi-level is measured to locate below the CBM, suggesting the absence of surface electron accumulation. Such intrinsic InN nanowires can possess an extremely low free carrier concentration of ~10^{13} cm^{-3}, as well as a close-to-theoretically-predicted electron mobility in the range of 8,000 to 12,000 $cm^2/V\cdot s$ at room temperature. This result is in direct contrast to the universally observed 2DEG on the InN grown surfaces. Furthermore, the surface charge properties of InN nanowires, including the formation of 2DEG and the optical emission characteristics can be precisely tuned, for the *first* time, through the controlled *n*-type doping.

More importantly, *p*-type doping into InN nanowires is also realized, for the *first* time. The presence of Mg-acceptors is clearly demonstrated by the PL spectra. Furthermore, *p*-type surface is observed from the XPS experiments, indicating the presence of free holes. Additionally, *p*-type conduction is directly measured by single nanowire field effect transistors.

In the end of this thesis, InN nanowire *p-i-n* photodiodes are fabricated, with a light response up to the telecommunication wavelength range at low temperatures. This thesis work provides a vivid example, and paves the way for the rational "materials by design" development of silicon integrated InN-based device technology in the nanoscale.

Abrégé

Les nanofils semi-conducteurs sans dislocations sont une voie très prometteuse vers l'intégration des semi-conducteurs composés avec la technologie silicium. Cependant, un contrôle précis de dopage des nanofils, ainsi que les propriétés de charge de surface, reste un défi universel à ce jour. À cet égard, nous avons étudié la croissance épitaxiale par faisceau moléculaire et les propriétés de surface corrélés électriques et optiques des nanofils de InN sur du substrat de silicium, qui ont émergé comme candidat prometteur pour l'avenir des dispositifs électroniques et photoniques à très haute vitesse et à échelle nanométriques.

Pour la première fois, en améliorant le processus de croissance épitaxiale, InN intrinsèque est atteint, à la fois dans le volume et sur les surfaces non polaires de InN. Le niveau de Fermi à la surface est mesuré et localisée sous le CBM, ce qui suggère l'absence d'accumulation d'électrons en surface. Ces nanofils InN intrinsèques possédent une concentration de porteurs libres très faible ~10^{13} cm^{-3}, ainsi que d'une mobilité proche de le théoriquement prédite d'électrons entre 8000 à 12000 $cm^2/V \cdot s$ à température ambiante. Ce résultat est en contraste direct avec les 2DEG observés sur les surfaces d'InN. En outre, les propriétés de charge de surface de nanofils InN, y compris la formation de 2DEG et les caractéristiques d'émission optiques, peut être réglé avec précision, pour la première fois, par l'intermédiaire du contrôle d'incorporation de dopants de type *n*.

Plus important encore, dopage de type *p* dans les nanofils InN est également réalisé pour la première fois. La présence de niveaux d'énergie Mg-accepteur est démontrée par les spectres de PL. Dans ces nanofils dopés de Mg, il n'y a pas d'accumulation d'électrons de surface et le niveau de Fermi dans le volume est proche de la VBM, ce qui indique un matériau de type *p*.

En fin, la jonction *p-i-n* basé sur des nanofils InN photodétecteurs qui peut être utilisé en mode photovoltaïque est démontrée, avec une réponse à la lumière jusqu'à la longueur d'onde des télécommunications à de basses températures. Ce travail de thèse fournit un exemple frappant, ainsi que prépare le terrain pour le développement "matériaux par conception" de la technologie des dispositifs en silicium intégrée à base InN à l'échelle nanométrique.

1. Introduction

III-nitride semiconductors (AlN, GaN, InN) have attracted extensive attention in the past decades due to their excellent optical and charge carrier transport properties, such as high electron mobility and large electron saturation velocity, high breakdown electric field, as well as excellent chemical stability and thermal conductivity.(*1-4*) For these reasons, their heterostructures have been intensively investigated for applications in light emitting diodes (LEDs),(*5-14*) laser diodes (LDs),(*11, 15-21*) photodetectors(*22-32*) and solar cells(*33-39*), as well as high mobility transistors(*40-45*) and sensors(*46-49*). Additionally, significant efforts have been devoted to reducing device cost, as well as to using large area and flexible substrates.(*50-53*)

On the other hand, InN, with the recently discovered narrow bandgap and extremely high electron mobility as well as the large saturation velocity, has attracted significant attention for ultrahigh-speed electronic and photonic devices and systems.(*4*) Nevertheless, compared with the relatively mature GaN-based devices and systems, the In-containing III-nitrides are still in their infancy due to the challenges that will be discussed in this chapter. In this regard, achieving high-quality InN and further understanding their fundamental optical and electrical properties are of great importance to realize InN-based ultrahigh-speed electronic and photonic devices, as well as to extend the current III-nitride devices to longer wavelength.

In this chapter, we will first discuss the importance of InN to the III-nitride family in Section 1.1. Then we will discuss the challenges in InN planar structures in Section 1.2. The need of nanowire structures as well as the current status and challenges of InN nanowires are discussed in Sections 1.3 and 1.4, respectively. In the end, the summary of the contribution of this thesis work and the thesis organization are described in Section 1.5.

1.1. The importance of InN to the III-nitride family

InN has three important features that draw a lot of attention from industry. Firstly, InN has a very narrow bandgap (~0.65 eV).(*2, 54-63*) As illustrated in Figure 1-1 for the bandgap energy vs. the lattice constant of III-nitrides, InN extends the bandgap of the III-nitride semiconductor family from the ultraviolet (~0.2 μm for AlN and ~0.36 μm for GaN) to the near-infrared (~1.9 μm for InN), which therefore provides a wide-range of tunability in the energy and drives the III-nitride devices to longer wavelengths (e.g., red, near-infrared). Secondly, InN is theoretically predicted to possess the highest electron mobility (~12,000 $cm^2/V \cdot s$) and the largest electron saturation velocity (~10^8 cm/s) among all III-nitride semiconductors at room temperature.(*64-68*) Lastly, InN has a very large absorption coefficient, which is ~10^5 cm^{-1} in the visible spectrum range and ~10^4 cm^{-1} in the telecommunication wavelength range.(*55-57*)

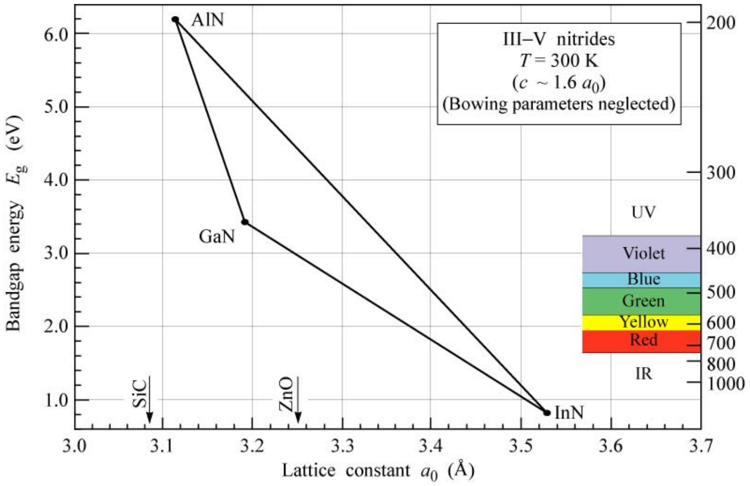

Figure 1-1 Diagram of the bandgap energy as a function of the lattice constant for III-nitrides.(*69*)

These three excellent features immediately render InN as a promising candidate for a wide range of ultrahigh-speed electronic and photonic devices such as ultrahigh-speed transistors, multijunction solar cells, nanoscale lasers, and photodetectors.(*4*) Moreover, InN is *nontoxic* and *environment-friendly*; this is in high contrast to the commercialized As and P-based materials. Additionally, InN can be grown on Si substrate, and the low-growth temperature is within the complementary metal-oxide-semiconductor (CMOS) thermal budget, which indicates that InN can be practically integrated with Si CMOS technology. Besides these excellent properties of InN that attract extensive research sources (importance in itself), InN is also of critical importance to the device applications based on ternary III-nitride semiconductors, such as the In(Ga)N-based devices.

1.1.1. The importance of InN to In(Ga)N-based devices: An example

With the first demonstrations of In(Ga)N-based high-efficiency LEDs and LDs by Nakamura more than twenty years ago,(*8*) In(Ga)N planar structures have become the key ingredient for billions of LED lamps and have transformed the multi-billion dollar solid state lighting industry.(*70*) Additionally, In(Ga)N has drawn significant attention recently for photoelectrochemical water splitting, which utilizes the most abundant natural sources on earth – water and sunlight, to produce oxygen and hydrogen that can be readily used as renewable energy.(*71*) Compared to the conventional large bandgap metal oxides, the energy bandgap of In(Ga)N can cover nearly the entire solar spectrum.(*4*) Moreover, In(Ga)N is also a potential photocatalyst to reduce and/or recycle the carbon-dioxide by utilizing protons from water decomposition and sunlight to generate clean liquid fuels.

Albeit all these attractive applications of In(Ga)N ternary compounds, there is a big road block: the device performance severely drops in longer wavelength. With increasing the In concentration, due to the presence of large dislocation density, the device performance is poor in general. For example, the internal quantum efficiency (IQE) of GaN-based green and red-color emitting LEDs is significantly lower compared with blue-color emitting LEDs due to the increased dislocation density and strain as In content is increased.(*6*)

In addition, the performance of InGaN-based LDs in the blue-green wavelength range has been severely limited by the large lattice mismatch between InGaN and GaN, as well as the associated strain-induced polarization field.(*72*) As a consequence, the currently reported LDs that operate in the wavelength range of 500 to 530 nm exhibit extremely large threshold current of ~10,000

A/cm^2, or higher,(*6, 73*) which is more than a factor of 10 to 100 larger than that of other semiconductor LDs.

In this regard, achieving high-quality InN, as well as understanding the fundamental electrical and optical properties of InN, is of crucial importance, as another route, to push device performance to longer wavelength, as well as for ultrahigh-speed near-infrared device applications.

1.2. Challenges in InN planar structures

Besides the aforementioned limited performance of In(Ga)N-based devices, InN-based devices in the near-infrared spectrum range have remained largely unexplored, which is in direct contrast to the relatively mature and commercialized GaN-based devices such as blue LEDs. This has been primarily limited by three practical challenges in InN planar structures, i.e., the lack of intrinsic InN, the uncontrolled surface charge properties/surface electron accumulation, and the difficulty in realizing *p*-type InN. These challenges have been recognized as the major roadblocks towards the realization of InN-based electronic and photonic devices in the near-infrared spectrum range. We will discuss these challenges in details from Sections 1.2.1 to 1.2.3, and the underlying mechanisms in Section 1.2.4.

1.2.1. Lack of intrinsic InN

For an intrinsic semiconductor, free carrier concentration is very low, and the Fermi-level is located near the midgap position.[1] This, however, has *not* been achieved in InN planar structures; several electrical and optical experiments on *nominally* non-doped InN indicate extremely high free carrier concentration, which is in the range of ~$10^{17\text{-}18}$ cm^{-3};(*57, 74-79*) and the Fermi-level is located deep in the conduction band.(*80-85*) The optical and electrical properties, therefore, normally exhibit strong *n*-type characteristics.

---

[1] The deviation from the midgap position should be small, normally on the order of 0.1 eV, or less, due to the difference between the effective density of states in the conduction band and valence band.

1.2.1.1. The optical properties of *nominally* non-doped InN

Absorption spectrum – For a historical reason, due to poor material quality, photoluminescence (PL) cannot be measured due to the large nonradiative recombination rate caused by large density of defects. The optical properties of InN were primarily investigated by absorption spectrum. With the limited material quality, the bandgap of InN determined by the absorption edge was initially quite high (~1.9 eV).

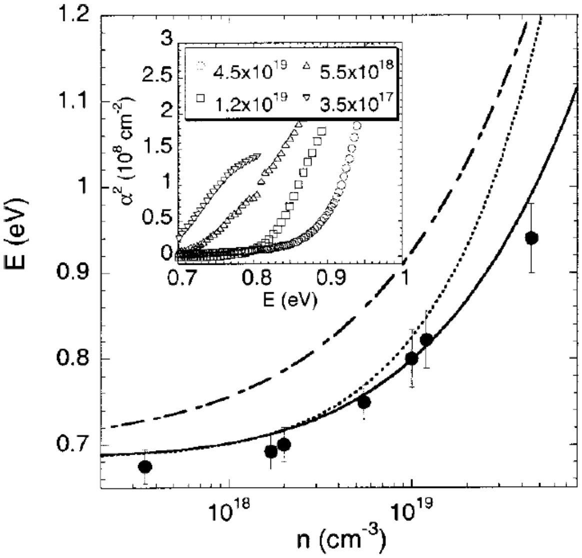

Figure 1-2 The room temperature absorption edge as a function of free carrier concentration in InN.(*56*)

With improved material quality, low absorption edges (~1 eV) were measured by Wu *at al.*,(*55*) Matsuoka *et al.*,(*54*) and Davydov *et al.*,(*57*) suggesting for the first time that InN has a very narrow bandgap (less than 1 eV). It was realized later on that *nominally* non-doped InN nanowires are in general *n*-type degenerate, so the presence of large free carrier concentration renders the absorption edge to occur at an energy level deep in the conduction band, i.e., at an energy much larger than the bandgap energy of InN.(*56*) Figure 1-2 shows the influence of free carrier concentration on the absorption edge, from which it can be seen that, as free carrier concentration increases, the absorption edge shifts to a higher energy.

Photoluminescence spectrum – With much improved material quality, PL emission from InN is possible to measure, and the PL characteristics of InN films have been comprehensively investigated, which strongly depend on free carrier concentration.(*76, 77, 79, 86-88*) For InN films with high free carrier concentration, the PL spectra in general exhibit very broad peaks with peak energies larger than the bandgap energy of InN, showing nearly *no* temperature- and power-dependences. With reduced free carrier concentration, the PL peaks possess energies close to the bandgap energy of InN and become narrower showing power- and temperature-dependences.

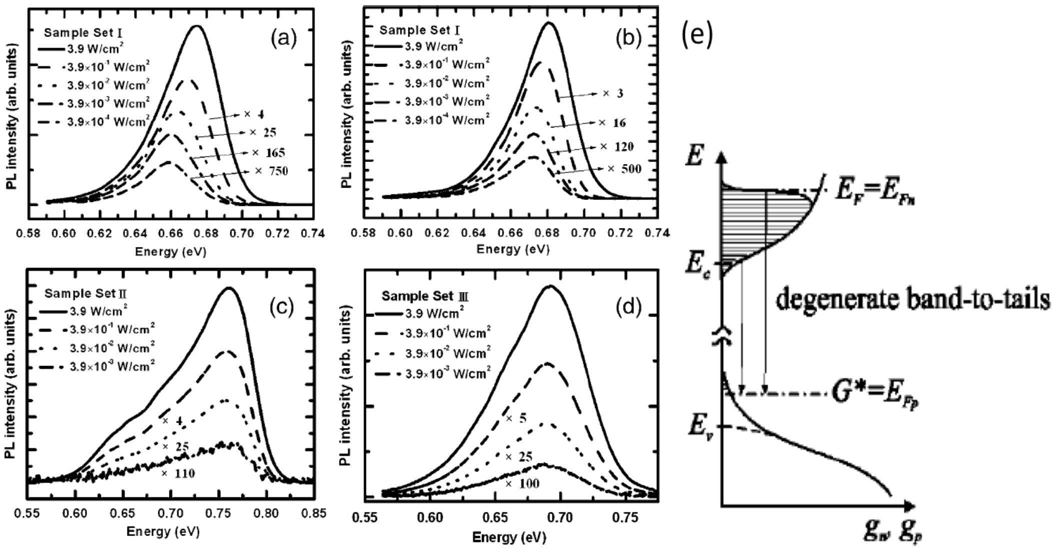

Figure 1-3 PL properties of InN films. (a) to (d) shows the PL spectra with carrier concentration of 5.7×10^{17} cm^{-3}, 1.4×10^{18} cm^{-3}, 9×10^{18} cm^{-3}, 1×10^{19} cm^{-3}, respectively.(*79*) (e) The PL recombination mechanism in *n*-type degenerate InN films.(*77*)

This evolution of PL characteristics with free carrier concentration is shown in Figure 1-3(a) to (d).(*79, 89*) The underlying PL emission mechanism is suggested to originate from Mahan exciton emission, i.e., photons are produced via the recombination between electrons near the Fermi-level or Fermi-edge and localized photo-generated holes in the valence band tail (as shown in Figure 1-3(e)).(*77, 79, 86, 89, 90*) The presence of such localized holes, for one reason, can be attributed to the large hole effective mass.(*77*)

Raman scattering – Moreover, the presence of large free carrier concentration can also be reflected in Raman scattering experiments, in which the main Raman shift peak, E_2^H, is significantly broad, due to large free carrier concentration.(*91-95*)

1.2.1.2. The electrical transport properties of ***nominally*** non-doped InN

Electrical transport properties of non-doped InN films have been investigated from the Hall effect measurements,(*65, 74, 75, 96, 97*) which indicates extremely high free carrier concentration. With the recent improvement of the growth technique, the boundary-temperature-controlled epitaxy,(*65*) the free carrier concentration is reduced to ~1×10^{17} cm^{-3}. In terms of electron mobility, the highest electron mobility achieved in InN films is in the range of 3,000 to 3,500 cm^2/V·s (with a free carrier concentration of ~10^{17} cm^{-3}).(*65*) The significantly lower electron mobility, compared to the theoretical prediction (~ 12,000 cm^2/V·s at room temperature), has been attributed, by and large, to the presence of extremely high free carrier concentration and large dislocation density.(*65, 67*) The scattering events from electron-electron, electron-fixed ionized unintentional dopants, and electron-dislocation severely reduce the experimentally measured electron mobility.[2]

1.2.2. Uncontrolled surface charge properties

In addition to high free electron concentration for nominally non-doped InN, an inhomogeneous distribution of electrons with a very high electron concentration (~$1\times10^{13-14}$ cm^{-2}) on both the polar and non-polar *grown* surfaces of InN has been observed (i.e., the presence of surface electron accumulation).(*74, 75, 80-85*) In this regard, significant efforts have been devoted to controlling the surface charge properties (primarily the surface electron accumulation) of InN, such as performing surface treatments,(*98*) and improving the growth techniques.(*63, 65,*

---

[2] Here we assume a low electric field limit, so that electrons cannot move from one conduction band valley to another. Therefore, the effective mass is not changed, and electron mobility is limited by the mean time between collisions.

78, 86, 96) However, all these approaches cannot remove the accumulated electrons on InN surface. To date, large free carrier concentration and the surface electron accumulation, together with the Fermi-level pinning into the conduction band are still prevalently observed in InN. The high-density surface electrons severely affect the electrical and optical properties. For example, this is another important reason that accounts for the much lower electron mobility compared with theoretical prediction.(*80, 99*) Also, as elucidated in Chapter 6, the surface electron accumulation could be a very important reason for the broad PL spectra of InN nanowires.

Recently, experiments through cross-sectional scanning photoelectron microscopy/spectroscopy (SPEM/S)(*100*) and tunneling *I-V* spectroscopy(*101, 102*) made a big step towards understanding the surface charge properties of InN. As shown in Figure 1-4, it was found for the *first* time that there can be *no* surface electron accumulation on *cleaved* non-polar InN surface, or the near-surface Fermi-level in InN can locate below the CBM. Nevertheless, for practical device applications, one needs to achieve the absence of surface electron accumulation, and furthermore, to *tune* the surface charge properties, as well as the associated optical and electrical properties, through a *practical* manner such as by controlling the growth process. This, however, remains elusive in InN planar structures.

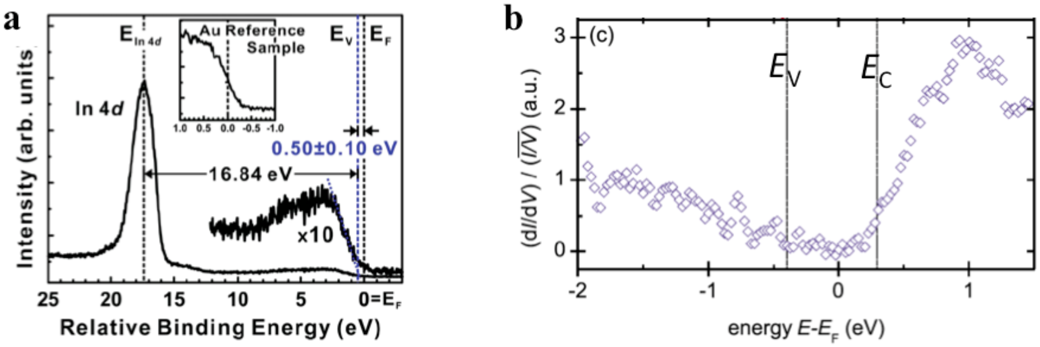

Figure 1-4 Demonstration of the absence of electron accumulation on *cleaved* InN surface with SPEM/S (a)(*100*) and tunneling *I-V* spectroscopy (b)(*102*).

1.2.3. Difficulty in achieving *p*-type InN

To realize practical device applications with InN, besides controlling the surface charge properties, another critical point is to achieve *p*-type InN. Even though manganese (Mn)(*103*) and zinc (Zn)(*104*) dopants are recently found as potentially alternative routes to achieve *p*-type doping into InN, magnesium (Mg), with an activation energy of ~60 meV in InN, is the most popular element to realize *p*-type doping in InN.(*105, 106*) However, due to extremely high background doping concentration (high free electron concentration) in *nominally* non-doped InN, *p*-type doping was impossible to achieve and/or to detect.

It is not until recently that a number of experiments suggest that *p*-type doping could be possible. Firstly, PL experiments clearly demonstrated the existence of Mg-acceptors.(*75, 107-109*) Secondly, electrolyte-based capacitance voltage (ECV) experiments indicated that the buried *p*-type conduction could exist underneath the surface electron-screening layer.(*75, 110-113*) These experiments, however, cannot provide a direct evidence for *p*-type conduction. Recently, several thermoelectric measurements suggest the existence of free holes;(*107, 111, 114, 115*) this, however, is quite debatable due to other possibilities that can contribute to a positive Seebeck coefficient.(*116*) In this regard, a *direct* evidence for the presence of free holes or *p*-type conduction remains elusive.

1.2.4. The underlying mechanism of the challenges

1.2.4.1. Lack of suitable substrate

In the heart of all challenges in InN planar structures lies the lacking of suitable substrate. As seen from Figure 1-5, all the commercial substrates, such as sapphire and SiC, have huge lattice mismatch to InN. Additionally, these substrates are very expensive, which makes the integration of InN-based devices onto these substrates *not* cost-effective. It is fortunate, due to the important role of Si in modern technology, that the lowest lattice mismatch is achieved on Si substrate, compared to other commonly used substrates for III-nitrides. This immediately provides a distinct advantage for InN, i.e., the potential integration to Si.[3]

However, it should be noted that even with Si substrate the lattice mismatch is still very large, which is ~7-8%. The direct consequence of large lattice mismatch is the presence of large density of dislocation and strain, which are important defect sources in InN planar structures. Additionally, the large lattice mismatch with GaN is believed to be responsible for the formation of InN or GaN clusters in In(Ga)N ternary compounds when In or Ga concentration is high. In this regard, significant efforts have been devoted to technically modifying the growth process such as the In/Ga-metal shutter interrupted growth by MBE.(*117*)

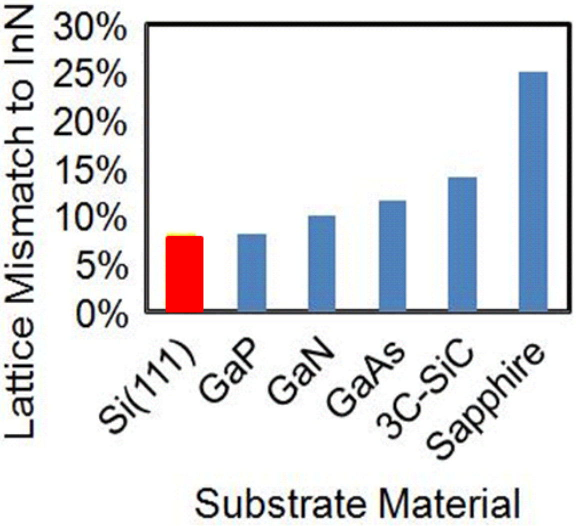

Figure 1-5 The lattice mismatch of InN to various commercialized substrates.

The large density of defects immediately create a big problem for materials with narrow bandgaps, such as InN and InAs, which have emerged as an important category for nanoelectronic and nanophotonic devices in the infrared spectrum range. In these materials, the CBM lies well below the charge neutrality level (CNL) due to the low In-5*s* orbital energy.(*118-120*) In the extreme case of

---

[3] However, as we will show later on, the growth of InN(GaN) nanowires might *not* be related to the epitaxial relationship with the Si substrate; they can be grown on amorphous template. In this sense, the nanowires can be integrated to *any* substrate. See Chapter 2 for details.

InN, which has the lowest CBM of any reported semiconductor, see Figure 1-6,(*120*) the CNL is positioned 1.2 to 1.8 eV above the CBM.(*81, 120, 121*) Therefore, any defect or impurity in these compounds generally becomes donor-like, leading to extremely high electron density even in *nominally* non-doped structures. Common to these materials is the near universal observation of a two-dimensional electron gas (2DEG) or surface electron accumulation on surface, and the near-surface Fermi-level is pinned deep into the conduction band.(*80, 85, 118, 122-124*)

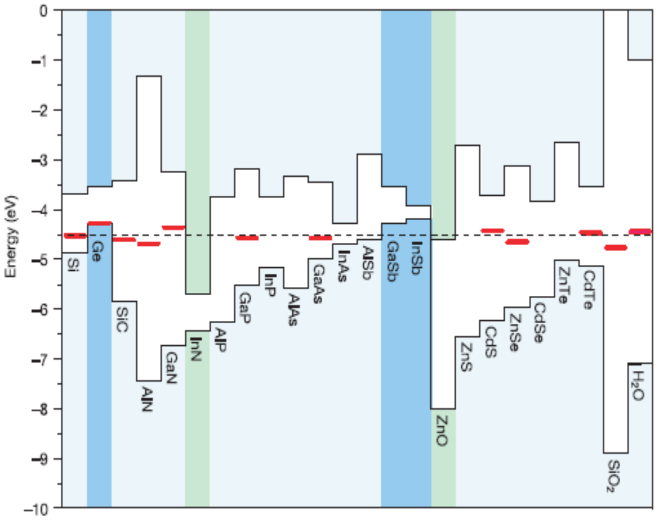

Figure 1-6 Band lineups for a range of semiconductors and insulators.(*120*)

1.2.4.2. The surface electron accumulation: The most debatable issue in InN

Initially, the surface electron accumulation (or the uncontrolled surface charge properties) is believed to be intrinsic due to the electrochemical nature (the aforementioned very low CBM and very high CNL) of InN. However, recent theoretical calculation indicates that the surface electron accumulation is critically dependent on surface polarity, i.e., polar planes or non-polar planes, as well as other factors such as surface states, impurities, and stoichiometry.(*98, 106*) The surface electron accumulation, therefore, is only expected to exist on polar planes, while for non-polar planes there should be no electron accumulation.(*106, 125*)

Figure 1-7 shows the density of states (DOS) of InN in terms of the bulk region, polar planes, and non-polar planes. It can be seen that for polar planes

(Figure 1-7(a)), the large-density surface states *only* exist above the CBM. In this case, the presence of surface electron accumulation on the polar planes can be explained by the presence of a large density of occupied In-In bond states above the CBM.(*125*) Additionally, donor-type surface states are allowed to exist in the conduction band due to the high CNL level (or the low CBM), which could be another reason for the presence of surface electron accumulation on the polar planes.(*81*) For non-polar planes (e.g., nanowire sidewalls in the presented thesis work), however, the large-density surface states exist *both* above and below the CBM. Therefore, the surface electron accumulation might *not* be expected in this case.(*125*)

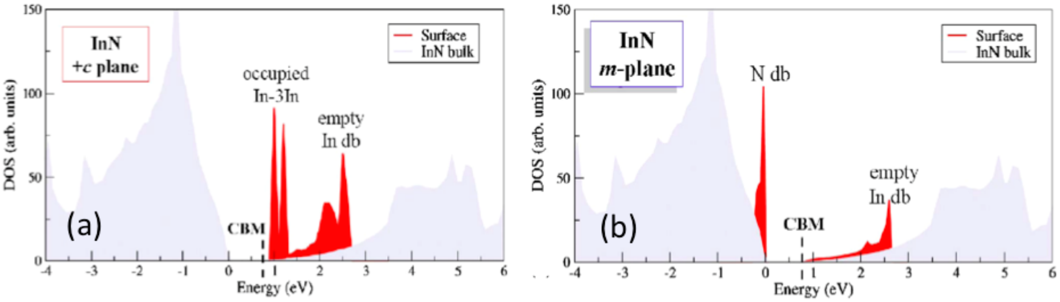

Figure 1-7 Density of states (DOS) of InN for both bulk and surface with (a) polar planes and (b) non-polar planes.(*125*)

The theory prediction, however, only agrees with the experimental results for InN polar planes.(*80, 81*) For the non-polar planes, the experimental results are quite debatable: many experiments indicate the presence of surface electron accumulation,(*79, 126-130*) but there are also a few experiments that indicate the absence of surface electron accumulation (please refer to Figure 1-4).(*100-102*) *In this sense, the surface electron accumulation issue is not clear for InN non-polar planes, and prior to this thesis work, the surface electron accumulation is prevalently observed on InN grown surfaces, which not only severely influences the electrical and optical properties, but also drastically limits practical device applications of InN-based materials.*

1.3. The need of InN nanowire structures

The large dislocation density in InN planar structures and InN(GaN) clusters in In(Ga)N ternary compounds, which are directly related to the large lattice mismatch, may be removed in nanowire structures due to the much efficient strain (and thermal) relaxation to nanowire lateral surfaces.(*131-135*) For planar structures, the critical thickness is determined by the lattice constant of the substrate and the lattice mismatch with the top epilayer. This limits the thickness (critical thickness) of growing a given material on a given substrate. In nanowire structures, the situation is significantly different. The recent theoretical study indicates that the critical thickness of nanowires is closely related to the nanowire radii; and if the nanowire radii are smaller than certain critical value, the critical thickness can be infinity.(*131*)

On the other hand, Moore's Law predicts the shrinkage of transistor size, which has been materialized by the constant reduction of the feature size of Si CMOS technology.(*136-138*) Ultimately, however, this essentially requires the electronic and optic components that are integrated to Si to be in nano-size, which immediately requires the study of low-dimensional nanostructures such as nanowires. In this sense, a fundamental understanding of InN nanowires in terms of their optical and electrical properties is of great importance to realize low-dimensional near-infrared electronic and photonic devices on Si.

1.4. InN nanowires: The current status and challenges

Driven by the aforementioned advantages of the nanowire structures, tremendous efforts have been devoted to growing InN nanowires, as well as improving the quality of InN nanowires.(*126-129, 132, 139-145*) The growth of InN nanowires as well as the underlying mechanisms will be discussed in details in Chapter 2.

1.4.1. The current status

To date, the *nominally* non-doped InN nanowires typically exhibit tapered morphology. Large residual electron concentration with the presence of surface electron accumulation, as well as the pinning of the near-surface Fermi-level in the conduction band is prevalently observed in such InN nanowires.(*126-128, 130, 146*) This, as a consequence, results in poor optical and electrical properties.

1.4.1.1. The poor optical and electrical properties of InN nanowires compared with InN planar structures

Optical properties – Significant efforts have been made to study the PL properties of InN nanowires,(*126, 129, 140, 144, 147*) which are significantly influenced by the large free carrier concentration. The typical PL spectra are shown in Figure 1-8. It can be seen that the PL spectra are extremely broad, with the linewidth on the order of 80 to 100 meV; and the PL peak energies are significantly higher than the bandgap energy of InN. More importantly, the PL peaks exhibit no temperature- and power-dependences. Until now, it is worth mentioning that, compared with the improved optical quality of InN epilayers, e.g., for InN epilayers it is now possible to control the PL properties with reduced free carrier concentration, the optical quality of *nominally* non-doped InN nanowires has remained poor.

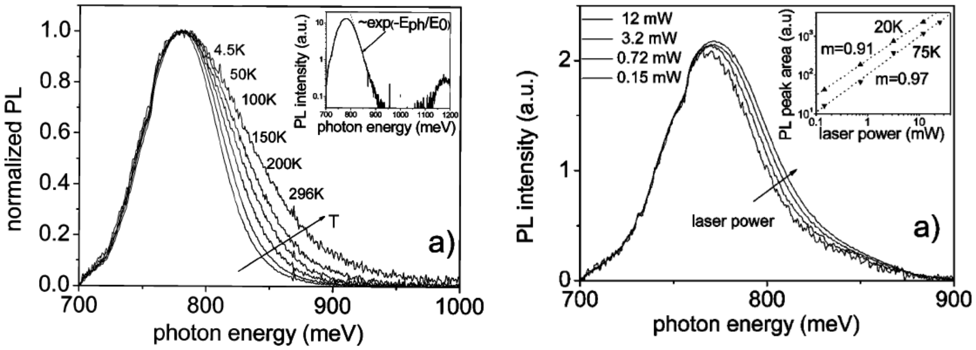

Figure 1-8 Photoluminescence properties of nominally non-doped InN nanowires (*n*-type degenerate).(*126*) Left: the temperature-dependent PL spectra, and Right: the power-dependent PL spectra.

To date, the PL properties of InN nanowires generally exhibit a very large inhomogeneous broadening, a peak energy considerably larger than the bandgap energy of InN, as well as the anomalous dependence on temperature and optical excitation power. *With these strong n-type characteristics of nominally non-doped InN nanowires, the PL properties of intrinsic InN nanowires, as well as the dependence on free carrier concentration and surface charge properties have* *remained elusive.*

In addition, Raman scattering experiments were performed on InN nanowires. Similar to InN planar structures, the surface electron accumulation associated Raman shift peaks are prevalently observed in InN nanowires.(*148-150*)

Electrical properties – Electrical properties (particularly free carrier concentration and electron mobility) of InN nanowires have been investigated through nanowire field effect transistors due to the difficulty in performing the Hall experiments in nanowire structures.

The free carrier concentration of InN nanowires is typically determined to be on the order of $10^{18\text{-}19}$ cm^{-3}, or higher,(*99, 127-129*) which is about 10 times larger than the lowest value reported for InN planar structures.(*63, 65*) The electron mobility, on the other hand, is estimated to be in the range of 100 $cm^2/V{\cdot}s$ to 470 $cm^2/V{\cdot}s$,(*127, 151*) which is about 10 times smaller compared with the numbers derived from InN planar structures(*65*) and more than 20 times lower compared with the theoretical calculation.(*64, 152-154*)

1.4.2. The challenges

To date, InN nanowires face similar challenges compared with InN planar structures, namely, *lack of intrinsic InN*, *uncontrolled surface charge properties*, as well as *difficulty in achieving p-type doping*;[4] but different from InN planar structures where the bottleneck is the lattice and/or thermal mismatch, the bottleneck for InN nanowires at present can be ascribed to *uncontrolled* growth process.

From the afore-discussed optical and electrical properties of InN nanowires, it can be seen that there is an enormous amount of potential for one to improve the quality of InN nanowires by improving growth technique. In this thesis work, we will demonstrate that, by the drastically improved molecular beam epitaxial

---

[4] It is worth mentioning here that, in contrast to Mg-doped InN planar structures, the study of Mg-doped InN nanowires is near zero. The only available study is from Raman scattering.(*149*)

growth technique, intrinsic InN nanowires can be achieved, the surface charge properties can be *accurately* controlled, and *p*-type doping into InN nanowires is also possible.

1.5. Summary of the contribution and the organization of this thesis

In this thesis work, it is demonstrated that, by utilizing the nanowire structure and with the dramatically improved molecular beam epitaxial growth technique, all the aforementioned three challenges can largely be resolved. The progress achieved in this thesis work makes InN nanowires an extremely attractive candidate for nanoelectronic and nanophotonic devices and systems in the near-infrared spectrum range.

It is shown in this thesis that, (1) *intrinsic* InN nanowires can be achieved. This is strongly supported by XPS and micro-Raman scattering experiments. Additionally, the electrical and optical characterization indicate an extremely low free carrier concentration, which is ~10^{13} cm^{-3}. Meanwhile, the electron mobility can be as high as ~12,000 $cm^2/V{\cdot}s$ at room temperature. (2) The surface electron accumulation is *tunable* through the controlled *n*-type doping, which is evidenced by the clear shift of the near-surface Fermi-level into the conduction band and the presence of two PL emission regions with the incorporation of *n*-type donors. The achievement of intrinsic InN nanowires, and the controlled surface charge properties can also be captured by the theoretical calculation. (3) The *p*-type doping can be realized in InN nanowires. The presence of Mg-acceptors is clearly indicated by the PL experiments, and *p*-type surface is measured by the XPS experiments. More importantly, *p*-type conduction is observed from the single nanowire field effect transistors. In the end, InN nanowire *p-i-n* photodiodes are fabricated, which exhibit a light response up to the telecommunication wavelength range.

The thesis is organized as follows. The growth of InN nanowires, and other III-nitride nanowires such as GaN nanowires, as well as the underlying growth mechanism will be discussed in Chapter 2. In Chapter 3, the techniques employed for InN nanowire characterization, including optical spectroscopies and electrical transport properties measurements will be discussed. In Chapter 4, the direct evidence of achieving *intrinsic* InN nanowires will be provided, and the optical properties of intrinsic InN nanowires will be discussed as well. The electrical transport properties of such intrinsic InN nanowires will be discussed in Chapter 5. The tuning of the surface charge properties with the controlled *n*-type doping, through both experimental study and theoretical calculation, will be discussed in Chapter 6. The achievement of *p*-type InN nanowires will be discussed in Chapter 7. InN nanowire *p-i-n* photodiodes will be demonstrated and discussed in Chapter 8. Finally, conclusions and future work will be presented in Chapter 9.

2. Growth of InN, and other III-nitride nanowires

As described in the previous chapter, due to the urgent need of InN, as well as other III-nitride nanowires in the future electronic and photonic devices and systems, significant efforts have been devoted to developing various techniques in growing III-nitride nanowires. In this chapter, these conventional techniques will be briefly introduced in Section 2.1. The underlying growth mechanisms of various growth techniques will be discussed in details in Section 2.2. The novel *in situ* In seeding layer assisted growth technique, which can lead to superior quality InN nanowires, will be discussed in Section 2.3. Due to the emerging flexible electronic and photonic devices, growing high quality III-nitride nanowires on amorphous template will be discussed in Section 2.4. In the end, the importance of III-nitrides grown by molecular beam epitaxy to industrial applications will be discussed in Section 2.5.

2.1. Growth techniques of III-nitride nanowires

To date, III-nitride nanowires can be obtained by top-down techniques such as dry etching,(*155-157*) direct reaction between group-III metals and NH_3,(*158, 159*) as well as the dominant bottom-up direct nanowire formation techniques such as chemical vapor deposition (CVD),(*139, 142, 143, 160-169*) molecular beam epitaxy (MBE),(*126, 132, 144, 170, 171*) chemical beam epitaxy (CBE),(*172*) and vapor phase epitaxy (VPE).(*173*) Additionally, in order to have a better control of the nanowire position, aspect ratio and uniformity, as well as the associated electrical and optical properties, selective area growth (SAG) technique has been developed using various growth systems such as metal organic CVD,(*174-178*) metal organic VPE,(*173*) and plasma-assisted MBE.(*179-181*)

2.2. Mechanisms of nanowire formation in general

Even though the growth techniques vary from one to another, they may share the same growth mechanism. For example, the diffusion driven mechanism can be applied to the gas source MBE(*182*) and CBE(*183*) in the formation of GaAs nanowires, or the radio-frequency (RF) plasma-assisted MBE in the formation of InN/GaN nanowires.(*132*) In this regard, we will discuss in this section the details of two important growth mechanisms related to the growth of group III-V nanowires: the vapor-liquid-solid (VLS) mechanism and the diffusion driven mechanism.

2.2.1. The vapor-liquid-solid (VLS) mechanism

The VLS growth mechanism in general involves the use of foreign metals such as Au, Ni, or Fe (the commonly referred catalysts) that act as nucleation centers and assist the nanowire growth. Growth procedure by the VLS mechanism was first introduced by Wagner and Ellis in 1964 who used Au particle as catalyst to grow Si nanowire whiskers from vapor sources such as $SiCl_4$ or SiH_4.(*184*) Based on this particular Si nanowire whiskers growth, the VLS mechanism was established, which, as one of the classical growth mechanisms, has been applied to many other semiconductor nanowires today. Since the VLS mechanism was historically established based on Si nanowire whiskers, we will discuss this mechanism in details based on Si nanowire whiskers growth.

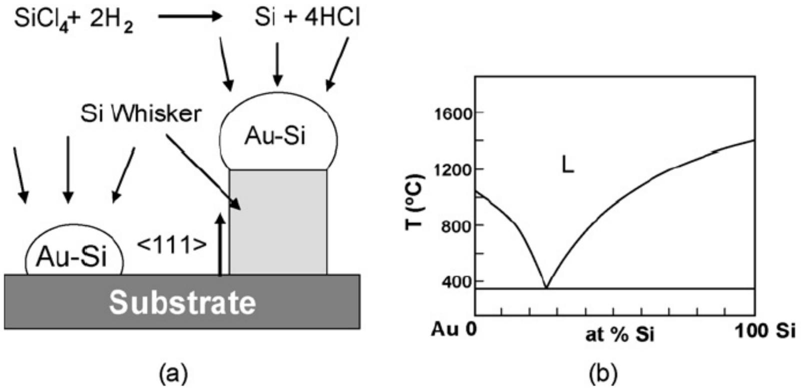

Figure 2-1 (a) Schematic plot of growing Si nanowire whiskers by the VLS mechanism. (b) The Si-Au phase diagram. (c) The Si absorption, diffusion, and precipitation path.(*142*)

In this process, a thin Au layer was first deposited. With a subsequent annealing, Au particles can be formed by the cracking of the thin Au layer. The subsequent growth process can be summarized in Figure 2-1(a). Firstly, the Au particles react with Si (the product of the chemical reaction between $SiCl_4$ vapor and H_2 vapor), to form Au-Si alloy liquid droplets at a certain temperature above the eutectic point and below the Si melting point (as shown in Figure 2-1(b)). Ideally, at high temperatures, the Si atoms from the vapor mixture will only be captured by the Au-Si liquid surface, due to their much larger sticking coefficient to the Au-Si liquid surface compared with that to the Si solid surface. At some point the Si will precipitate due to supersaturation, forming the crystalline structure starting from the liquid-solid interface. The Si absorption, diffusion, and precipitation path is shown in Figure 2-1(c), which typically involves vapor, liquid, and solid phases.

Such VLS mechanism also has a few variants,[5] such as vapor-solid-solid (VSS), solid-liquid-solid (SLS), solution-solid-liquid (SSL), to explain the formation of various compound semiconductor nanowires.(*142, 169, 185, 186*) Additionally, the VLS mechanism is believed to be the underlying mechanism for the guided growth of GaN nanowires on patterned substrate.(*178*)

2.2.1.1. Recent progress of growing InN nanowires by the VLS mechanism

The techniques of growing III-nitride nanowires by the VLS mechanism have been developed sophisticatedly, especially for GaN nanowires due to their important role in industry. A contemporary review of growing GaN nanowires by the VLS mechanism can be found in a review by Fathololoumi *et al.*.(*72*)

In the other hand, due to the need for the emerging near-infrared electronic and optical devices, significant efforts have been devoted to growing InN nanowires by various techniques based on the VLS mechanism.(*139, 143, 160-168*) For example, InN nanowires can be synthesized by a CVD technique in a quartz-tube reactor on Si substrate coated with SiO_x,(*161, 187*) or by a modified two-zone CVD technique on Si substrate coated with SiO_x,(*139*) or by a guided-stream thermal CVD technique on Si substrate but coated with SiN_x,(*160*) or on Al_2O_3 substrate by a CVD technique.(*143*)

The advantage of the growth techniques with the VLS mechanism is that

---

[5] In the rest content, we will use the VLS mechanism as a general term to describe growth process involving vapor, liquid, and solid phases, or combinations of any two phases.

long (a few micrometers) nanowires can be synthesized in a very short growth duration. However, foreign metal catalysts will usually diffuse into the semiconductor nanowires and serve as deep trap centers. As a result, the electrical and optical properties of the obtained nanowires will be significantly affected.

In this regard, growing InN nanowires by the novel *catalyst-free* techniques based on the VLS mechanism was also developed, to improve the material purity, as well as the electrical and optical properties. For example, InN nanowires can be grown by a metal organic CVD technique, where hydrogen is introduced intentionally to make the existence of metallic In; and due to the low melting point of In, In liquid droplet will be formed. Such liquid phase In will serve as catalyst to promote the growth.(*168*) InN nanowires can also be grown by a catalyst-free CVD technique on 4H-SiC substrate, in which high purity InN powders are used as source materials and the mixed vapor of N_2 and NH_3 is the reaction atmosphere.(*167*) Moreover, InN nanowires can be formed by a vapor transport of In in the presence of ammonia, wherein the InN nanocrystals, due to the supersaturation of In vapor, will serve as the nucleation center as well as the driving force for the nanowire growth.(*165, 166*) In addition, InN nanowires can be grown by an In predeposition technique in a CVD system,(*164*) or through a CBE technique on sapphire substrate.(*172*)

To date, however, the InN nanowires grown by the VLS mechanism in general exhibit uncontrolled nanowire morphology, as well as poor electrical and optical properties as described in the previous chapter.

2.2.2. The diffusion driven mechanism

In addition to the VLS mechanism, where the nanowire formation is through a supersaturation process, semiconductor nanowires can be formed by the diffusion driven mechanism, such as the Au-catalyst assisted formation of GaAs nanowires by the gas source MBE technique,(*182*) or the Au catalyzed formation of GaAs nanowires by the CBE technique,(*183*) or the spontaneous formation of III-nitride nanowires under N_2 rich condition by the RF plasma-assisted MBE technique.(*132, 144, 170, 171, 188*)

Initially, group III-V nanowires grown by these techniques were suggested to follow the VLS mechanism, wherein either Au or group-III metal serves as catalyst to promote the nanowire formation. This, however, is in disagreement with the experimental observations, e.g., the nanowire length scales inversely with the Au-catalyst size,(*182*) or the group-III metal droplets have never been observed on the tops or sidewalls of III-nitride nanowires during the formation process.(*133, 189*)

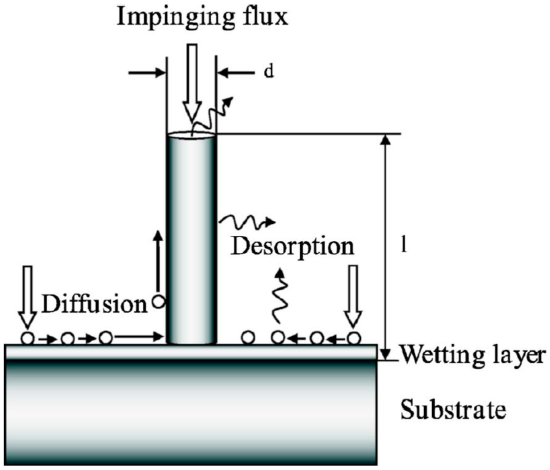

Figure 2-2 A schematic plot of the diffusion driven mechanism in the spontaneous formation of III-nitride nanowires under N_2 rich condition by MBE.(*190*)

The diffusion driven mechanism is schematically shown in Figure 2-2 based on the spontaneous formation of III-nitride nanowires under N_2 rich condition. The Au-catalyzed formation of GaAs nanowires follows a similar diffusion mechanism but with the Au-catalyst on top of nanowires.(*182*) Firstly, group-III metal adatoms are absorbed onto the surface at certain temperature, forming the nucleation center; then the group-III metal adatoms diffuse towards the top due to the lower chemical potential on the top surfaces. Considering the shadow effect from adjacent nanowires, as well as the higher sticking coefficient (or the lower desorption rate) on the nanowire tops compared with that on the nanowire sidewalls, the axial growth will be enhanced.[6]

This diffusion model is consistent with the fact that the nanowire axial growth rate increases rapidly with the increase of the substrate temperature, as well as the thinner nanowires have longer lengths. These effects can be ascribed to the significantly enhanced group-III metal adatoms surface diffusion/migration.

2.2.2.1. The spontaneous formation of III-nitride nanowires by molecular beam epitaxy

To date, the spontaneous formation of III-nitride nanowires is commonly realized under N_2 rich condition by MBE technique, which therefore combines the advantage of (1) *no* foreign metal catalyst hence the material purity is significantly increased; and (2) the merit of MBE technique such as the ultrahigh vacuum so that the material can possess extremely high purity, as well as the low growth rate so that atomically flat interface can be achieved.[7] Albeit the drastically improved electrical and optical qualities of III-nitride nanowires grown by this technique, the underlying mechanism is poorly understood.

To date, such spontaneous formation of III-nitride nanowires is generally understood as a diffusion driven process, wherein the formation of the nanowires is closely related to the anisotropies of surface energies, desorption rates/sticking coefficients, and diffusion coefficients on different crystalline surfaces.

GaN — Recent detailed studies further indicate that a thin amorphous layer exists between the GaN nanowire bottom and Si substrate (shown in Figure 2-3(a) and (b)),(*191, 192*) which essentially suggests the presumable *removal* of the epitaxial relationship between the nanowire and Si substrate.[8] *This might indicate that the growth of GaN nanowires by such spontaneous process under N_2 rich condition is fundamentally different from the growth of III-nitride epilayers.*

---

[6] Here, it is assumed that the diffusion length of group-III metal adatoms is larger than the nanowire length

[7] The advantages of MBE technique will be discussed in details in Section 2.5.

[8] This will be further confirmed by the growth on amorphous template as discussed in Section 2.4.

Additionally, the 2D spherical shape GaN nuclei were clearly observed in the initial growth stage (shown in Figure 2-3(a)). Such 2D nuclei were also observed on AlN buffer layer.(*135*) The shape, however, is pyramid-like (*not* spherical), which is due to the requirement of the elastic relaxation of the epitaxial strains. *This difference indicates that the initial nuclei are more closely related to the interface/buffer layer*. With such a clear demonstration of the 2D nuclei, the diffusion driven process can be theoretically modeled by quantizing the driving forces coming from the surface free energies, surface stresses, and the interfaces.(*192*)

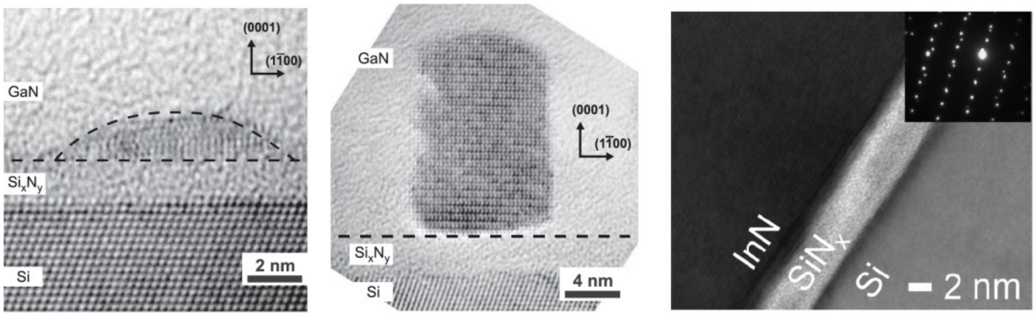

Figure 2-3 High-resolution TEM images of III-nitride nanowires. From left to right: (a) the initial nucleation of GaN nanowires and (b) the formation of GaN nanowires,(*192*) and (c) the interface layer between InN nanowires and Si substrate.(*58*)

InN — A thin amorphous layer was also observed between the InN nanowire bottom and Si substrate (shown in Figure 2-3(c)),(*58*) suggesting the presumably *removed* epitaxial relationship between InN nanowires and the substrate. *However, the growth mechanism of InN nanowires by spontaneous formation is not clear yet.*

Firstly, the initial nuclei formation has *never* been observed by high-resolution TEM. Secondly, compared with a clear diffusion driven mechanism where long GaN nanowires are typically thinner, InN nanowires do *not* exhibit such nanowire length-radius dependence. Instead, InN nanowires grown by this technique typically have much smaller length variation compared with radius variation. These different characteristics could come from the larger surface migration rate of In compared with that of Ga, or the growth mechanism of InN nanowires by this technique being different from that of GaN nanowires.(*193*)

2.2.2.2. The spontaneous formation of InN nanowires by molecular beam epitaxy: The material quality challenge

Endeavored efforts were devoted to achieving high quality InN nanowires/nanorods by the spontaneous formation under N_2 rich condition by MBE technique,(*126-129, 132, 144, 145*) and the achievement of dislocation-free InN nanowires has been confirmed by high-resolution TEM.(*145, 194*) However, as introduced in Chapter 1, such *nominally* non-doped InN nanowires typically exhibit tapered morphology (see Figure 2-4) and are *n*-type degenerate, with large free carrier concentration and Fermi-level being pinned deep into the conduction band, as well as the presence of surface electron accumulation.

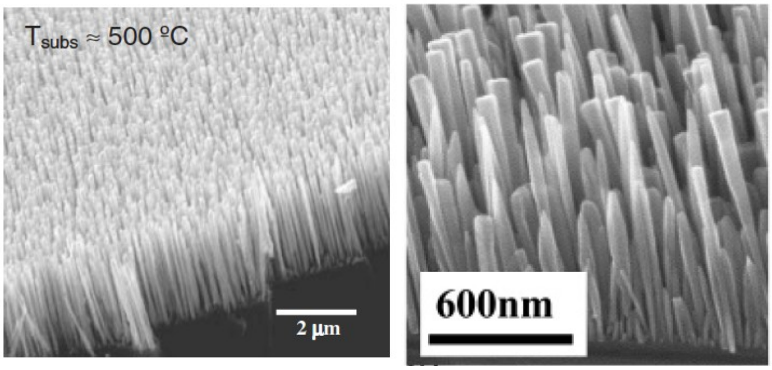

Figure 2-4 Spontaneous formation of InN nanowires under N_2 rich condition by molecular beam epitaxy. Left: from Calleja *et al.*(*132*), and Right: from Stoica *et al.*(*126*).

This could indicate the importance of non-polar surfaces (nanowire sidewalls) in nanowire structures, i.e., besides achieving a perfect lattice in an atomic scale, obtaining a good termination at the surface (i.e., non-tapered morphology) and near-perfect hexagonal lattice structure in a much larger scale is also important to minimize the n-type characteristics. We will demonstrate in Chapter 4 that non-tapered hexagonal InN nanowires can be *intrinsic*, with extremely low free carrier concentration and Fermi-level being located below the CBM.

2.3. A novel approach by the *in situ* In seeding layer deposition technique

From the above discussions, it can be seen that the conventional techniques generally lead to tapered InN nanowires with large free carrier concentration; hence intrinsic InN nanowires *cannot* be achieved. To solve this issue, we recently developed a novel *in situ* In seeding layer assisted growth process by MBE technique.(*58*) This method utilizes an *in-situ* deposited In seeding layer prior to the growth initiation, through which non-tapered InN nanowires can be achieved. The reason can be attributed to the controlled nuclei size with the introduction of the thin (~0.6 nm) In seeding layer which forms In droplets subsequently at high temperatures, compared with the spontaneous formation in which the nuclei size is random.(*58*)

Actually, a similar growth process, i.e., a Ga seeding layer assisted growth of GaN nanowires, was also investigated.(*195*) It is found that the axial growth rate can be enhanced significantly compared with that of the spontaneous formation of GaN nanowires. However the nanowire morphology does not improve much. This could be due to different growth mechanisms between InN nanowires and GaN nanowires, or the relatively small surface migration rate of Ga.

2.3.1. Demonstration of non-tapered InN nanowires

The *radio-frequency plasma-assisted* Veeco Gen-II MBE system is shown in Figure 2-5(a). Figure 2-5(b) shows the SEM image[9] of InN nanowires grown without the In seeding layer; only tapered InN nanowires can be obtained. As a comparison, InN nanowires grown with the In seeding layer were shown in Figure 2-5(c), which demonstrate a near-perfect hexagonal structure with equal diameters on the nanowire tops and bottoms (i.e., non-tapered surface morphology).

---

[9] The SEM images were taken using a Hitachi S-4700 system with a 45-degree angle. An accelerating voltage of 5 kV and a current of 10 µA were used for imaging.

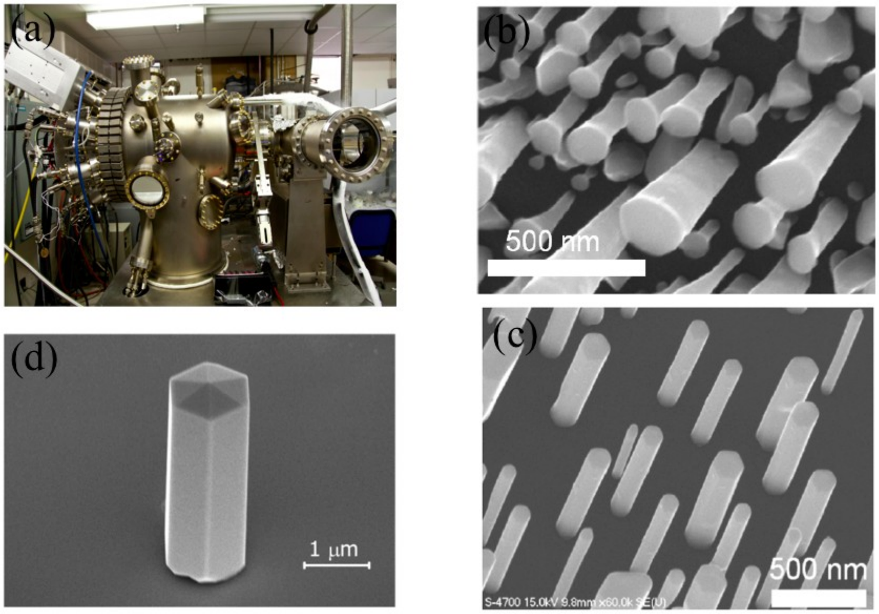

Figure 2-5 (Clockwise) (a) Veeco Gen-II molecular beam epitaxial growth system. SEM images of InN nanowires grown witout (b) and with (c) In seeding layer.(*58*) The cabability of obtaining long InN nanowires using this novel technique is shown in (d).

Furthermore, by optimizing the growth parameters (primarily the growth temperature), very long InN nanowires can be achieved (with diameters of ~1 μm, and lengths of ~4 μm). As shown in Figure 2-5(d), a large nanowire with a near-perfect hexagonal structure can be obtained, which clearly demonstrates the capability of this *novel* MBE technique in growing ultrahigh-quality InN nanowires. From Chapters 4 to 6, we will demonstrate that such InN nanowires can be intrinsic; and moreover, the surface charge properties can be precisely tuned by the controlled *n*-type dopant incorporation.

Additionally, it is noted that the nanowire morphology does *not* change significantly with the incorporation of Si-donors, Mg-acceptors, or even in the formation of InN nanowire *p-i-n* homojunctions as will be discussed in Chapter 8. *All these doped nanowires and nanowire structures exhibit non-tapered Wurtzite structure as that of non-doped InN nanowires.* Admitting the comparable surface morphology, the point defects *might* be significantly increased in doped InN nanowires. Therefore, as we will discuss later on, the PL intensity will be reduced significantly due to the enhanced nonradiative recombination rate as the doping concentration increases.

2.4. Growth of III-nitride nanowires on amorphous template

In terms of device applications, a very important factor that needs to be considered is the substrate cost. To drastically reduce the device fabrication cost,(*51, 53, 196*) as well as to achieve seamless integration with other device components for the emerging flexible photonic and electronic devices,(*50, 52*) it is of crucial importance and practical interest to develop high-quality semiconductor nanowires on *amorphous* and/or *flexible substrates*.

In general, the growth/synthesis of semiconductor nanowires on amorphous substrate involves the use of foreign metal catalysts, which leads to a significant level of impurity incorporation, as well as uncontrolled structural, electrical and optical properties.(*197-203*) Developing catalyst-free process to further improve the quality of semiconductor nanowires on amorphous substrate is of great importance. In this section, we will discuss growing high-quality GaN/InN nanowires on thick amorphous template via the afore-introduced novel MBE technique.

2.4.1. Demonstration of high-quality GaN nanowires on SiO*x* with controlled orientation

Due to the industrial importance of GaN,(*7, 8*) as well as the problems faced by GaN planar structures, the growth of GaN nanowires has been investigated intensively.(*170, 171*) For GaN nanowires spontaneously formed on amorphous layer,(*191, 192*) the nanowires generally exhibit random orientations, which is believed to be related to the local surface roughness of the underneath amorphous template.(*191*) Moreover, the optical quality of the spontaneously formed GaN nanowires on thick amorphous template has remained largely unknown. *To date, the realization of catalyst-free, electronically pure GaN nanowires on amorphous substrate with controlled orientation, and superior crystalline and optical quality in a large scale has remained challenging.*

In this regard, we have performed a detailed investigation of GaN nanowires grown on SiO*x* template. The SEM images of GaN nanowires grown at different substrate temperatures are shown in Figure 2-6: from (a) to (c) corresponds to ~830 °C, ~808 °C, and ~780 °C, respectively. In these growths, the N_2 flow rate was kept at ~1.0 sccm, and the underneath SiO*x* template has a thickness ~100 nm. It can be seen that as the substrate temperature decreases, the nanowire density increases dramatically. Meanwhile, the orientation of the nanowires changes from being random/tilted to almost-100% vertically aligned.

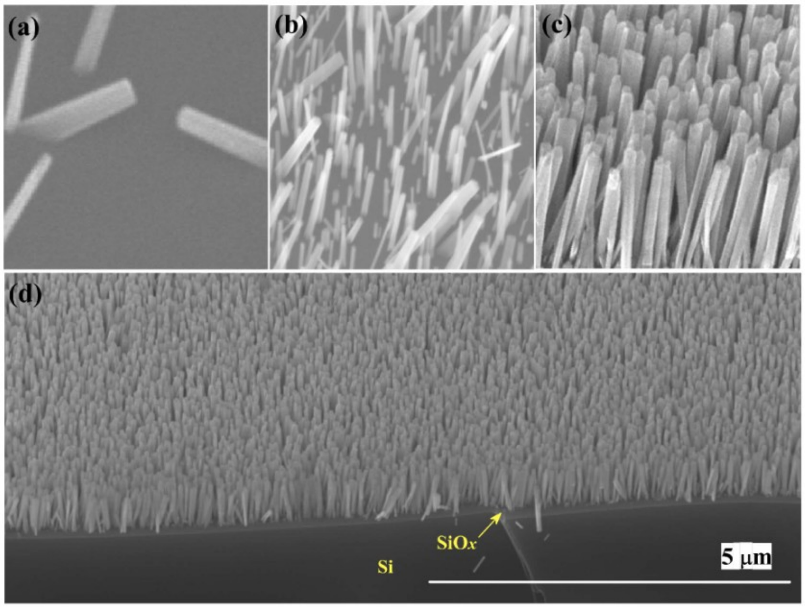

Figure 2-6 SEM images of GaN nanowires grown on SiO*x* template (thickness ~100 nm) under different substrate temperatures taken with a 45-degree angle, with (a) ~830 °C, (b) ~808 °C, and (c) ~780 °C, respectively; the SEM images are in size 1 µm by 1 µm. (d) Same growth parameters as in (c) but shown in a large scale with the SiO*x* layer as marked; this figure clearly demonstrates that highly uniform and vertically aligned GaN nanowires can be realized in a large scale on SiO*x* template.

Growth experiments were also performed by changing the N_2 flow rate from ~0.6 sccm to ~1.4 sccm, while keeping the substrate temperature fixed at ~790 °C. In this case, however, no significant change in the nanowire density, orientation, and uniformity was observed.

The temperature dependence of nanowire density/morphology can be understood by the following. At relatively high substrate temperatures, the Ga adatom desorption rate is high. Therefore the nucleation process is severely suppressed; as a result, the nanowire density is low (Figure 2-6(a)). In this case, the growth direction/orientation of GaN nanowires depends strongly on the surface roughness of the underneath SiO*x* template, thereby leading to random orientation for such low-density GaN nanowires. Similar is the case for the GaN nanowires with moderate density when the substrate temperature is decreased (Figure 2-6(b)): admitting the presence of vertically aligned GaN nanowires, the orientation is still highly dependent on the surface roughness of the underneath SiO*x* template.

This situation is changed with further decreasing the substrate temperature. The much-reduced Ga adatom desorption rate (which in turn enhances the nucleation process) results in GaN nanowires with a very high density ($\sim10^{11\text{-}12}$ cm^{-2}); and in this case, GaN nanowires are almost-100% vertically aligned (Figure 2-6(c)). This can be ascribed to, with high nanowire density the number of Ga adatoms that can impinge onto non-vertically orientated nanowires is significantly reduced, due to the shadow effect of surrounding nanowires. As a consequence, the growth of non-vertical nanowires is suppressed, thereby promoting the formation of vertically aligned and nearly uniform GaN nanowire arrays.

These results indicate that, besides the role of surface flatness, maintaining a high nanowire density is critical to achieve vertically aligned GaN nanowires on SiOx, and the substrate temperature plays a significant role under N_2 rich conditions.

The near-perfect size uniformity and controlled orientation can also be maintained for relatively long GaN nanowires. Figure 2-7(a) shows an SEM image (taken with a 45-degree angle) of GaN nanowires grown on SiO*x* template at ~ 780 °C with a N_2 flow rate ~0.6 sccm for a longer growth duration. It can be seen that the resulting nanowires maintain high uniformity and vertically aligned orientation. Figure 2-7(b) shows a low-magnification TEM image of a single GaN nanowire with a length ~1.8 μm and a diameter ~50 nm. As can be seen, it exhibits a very high uniformity, i.e., equal sizes on the nanowire top and bottom. Figure 2-7(c) shows a typical high-resolution TEM image of the root of a single GaN nanowire, which exhibits clear atomic planes, and is free of stacking faults. Detailed studies further confirm that the entire nanowire is also free of dislocations. The PL spectrum measured at room temperature is shown in Figure 2-7(d), and no defect-related yellow luminesce is observed. The peak at ~363 nm (with a linewidth ~6 nm) could be ascribed to the band-to-band carrier recombination, which is consistent with the bandgap energy of GaN.

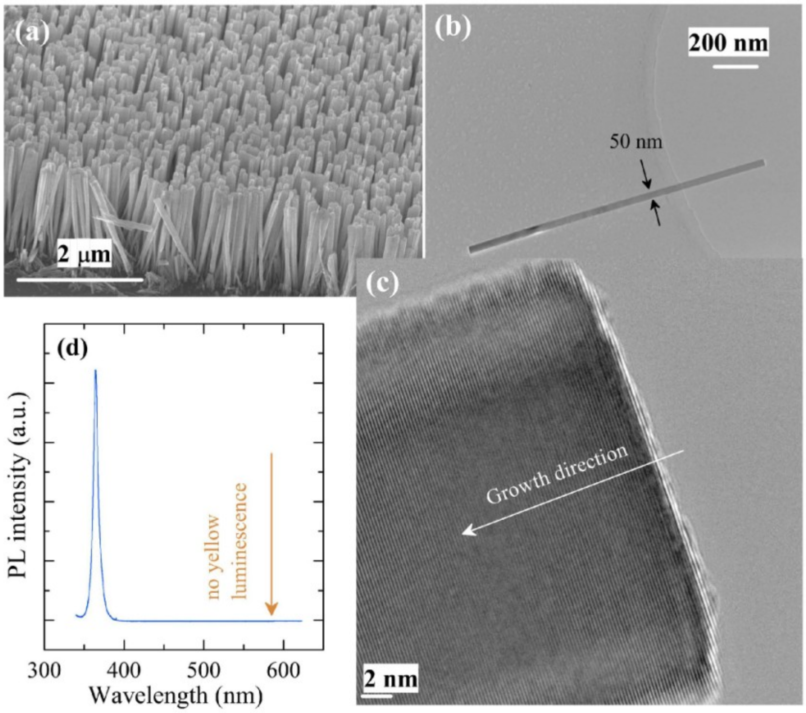

Figure 2-7 (a) An SEM image of GaN nanowires grown on SiO*x* (thickness ~100 nm) for a longer growth duration, taken with a 45-degree angle. (b) A low-magnification TEM image of a single GaN nanowire. (c) A high-resolution TEM image of the bottom of a single GaN nanowire. (d) PL spectrum measured at room temperature with a λ = 325 nm laser.

These results solidly indicate high-quality (both structurally and optically) vertically aligned GaN nanowires can be grown on amorphous template in a large scale; and the quality is comparable to that of GaN nanowires grown directly on

Si substrate,(*189-192, 204*) due to the possibly similar growth mechanism.(*170, 171, 191, 192*)

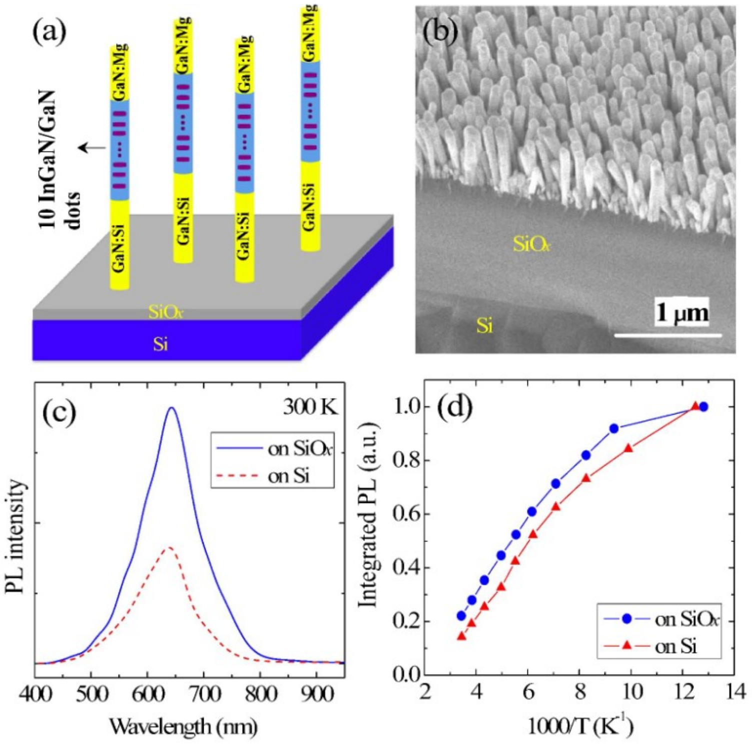

Figure 2-8 (a) Schematic plot of the InGaN/GaN dot-in-a-wire LED structures on SiO*x* (thickness ~1.5 µm). (b) The corresponding SEM image taken with a 45-degree angle. (c) PL spectra for such LED structures grown on SiO*x* (solid blue curve) and directly on Si substrate (dashed red curve), measured with a λ = 405 nm laser at room temperature. (d) Normalized integrated PL intensities as a function of the inverse temperature for these two samples, measured from 74 K to 300 K.

Next, we have further investigated the growth and characterization of the InGaN/GaN dot-in-a-wire LED structures(*205*) on thick (~1.5 µm) SiO*x* template (defined as "sample A"). The schematic plot of the structure is illustrated in Figure 2-8(a). The corresponding SEM image is shown in Figure 2-8(b). It can be seen that the InGaN/GaN nanowires are almost-100% vertically aligned with high uniformity, and the very short nanowires are due to the shadow effect as aforementioned. The room temperature PL spectrum of sample A is measured (shown as the solid blue curve in Figure 2-8(c)); the PL emission wavelength is ~650 nm. As a comparison, the PL spectrum from the same structure but grown directly on Si(111) substrate (defined as "sample B") is also shown (the dashed red curve in Figure 2-8(c)). It can be seen that sample A has comparable or even stronger PL emission intensity compared with that from sample B. The stronger PL emission from sample A could be ascribed to the reduced optical absorption by the SiO*x* template.

To reveal more details of these two samples, the inverse-temperature (from 74 K to 300 K) dependent integrated PL intensity is shown in Figure 2-8(d). The integrated PL intensities at 300 K are about 20% and 15% of those measured at 74 K for sample A and sample B, respectively. These measurements suggest that the optical performance of InGaN/GaN nanowire LED structures on SiO*x* is comparable to, if not better than that from the same structure but grown directly on Si substrate.

The achievement of highly vertically aligned and uniform GaN nanowires and their heterostructures with excellent structural and optical properties on SiO*x* template could provide an entirely new avenue for GaN nanowire based nanoelectronic and nanophotonic devices.

2.4.2. Growth of InN nanowires on SiO*x*

Following the same philosophy of the need of growing GaN nanowires on amorphous template, there is also such a need for growing InN nanowires on amorphous template. However, compared to the growth of GaN nanowires, the growth of high-quality InN nanowires is more difficult, largely due to the fact that the growth of InN nanowires is highly sensitive to substrate temperature and substrate cleaning process. Therefore, growing high-quality InN nanowires on amorphous template remains elusive.

In Section 2.3, we have demonstrated that non-tapered InN nanowires can be grown by a novel MBE technique on Si substrate, which possess excellent optical and electrical properties (as will be discussed in Chapters 4 and 5). Therefore, it would be of great interest to investigate the growth of InN nanowires on SiO*x* template with such MBE technique.

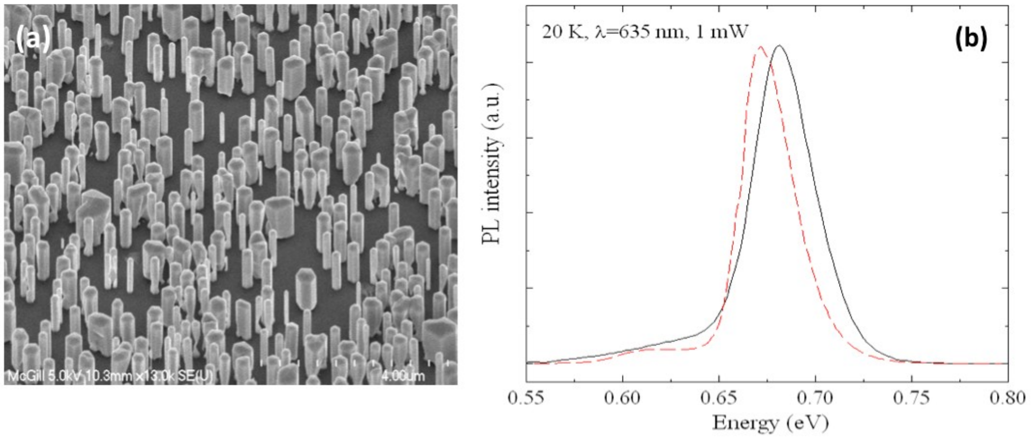

Figure 2-9 (a) An SEM image of InN nanowires grown on SiO*x* template. The thickness of the underneath SiO*x* is ~100 nm. (b) The corresponding PL spectrum measured at low temperature. Red dotted curve: the same measurement condition but on InN nanowires grown directly on Si.

Figure 2-9(a) shows an SEM image of InN nanowires grown on SiO*x* template. It can be seen that the nanowires are aligned vertically with similar morphology compared to that of InN nanowires grown directly on Si substrate. The corresponding PL spectrum measured at low temperature is shown Figure 2-9(b), with a low-temperature PL spectrum of InN nanowires grown directly on Si substrate for a comparison (dotted curve). It can be seen that the two PL spectra have comparable peak intensity. However, the PL peak energy of InN nanowires grown on SiO*x* template is higher; meanwhile, the associated PL spectral linewidth is broader compared with that of InN nanowires grown directly on Si. Such a blueshift of the PL peak energy and the broadening of the PL spectral linewidth measured from InN nanowires grown on SiO*x* could suggest a higher free carrier concentration due to the increased defects on nanowire surface.(*61, 62*)

2.4.3. Discussions

Considering the fundamentals of epitaxial growth, it generally requires a crystalline substrate to promote the growth, and the top epilayer shares the same surface crystalline orientation or orientates in one or more preferred directions with respect to the crystalline substrate. Therefore, the epilayer and the underneath substrate have an epitaxial relationship. This is the case for growing GaN/InN films by MBE technique, and the lattice mismatch between the epilayer and the underneath substrate is an important factor to be considered to improve device performance.

The growth of GaN/InN nanowires by MBE technique, however, as afore-discussed, could indicate *no* epitaxial relationship between the nanowires and the substrate.(*58, 191, 192*) Furthermore, from the demonstration of growing GaN/InN nanowires on amorphous template above, *it clearly indicates that the growth of GaN/InN nanowires does not rely on the epitaxial relationship between the nanowire and the underneath substrate; and the growth can be essentially performed on any substrate as long as the 2D nuclei, which often rely on (but may not be limited to) the presence of an amorphous interface (e.g., SiNx, SiOx),*[10] *can be formed.(191, 192) The subsequent shape transformation is driven by the anisotropies of surface free energies, surface stresses, as well as the interface barriers.(191, 192)*

In the end, comparing the SEM images of InN nanowires (Figure 2-9(a)) and GaN nanowires (Figure 2-6) grown on SiO*x*, it can be clearly seen that the orientation of GaN nanowires is highly dependent on the nanowire density, which, however, is *not* the case for InN nanowires, i.e., InN nanowires can remain highly vertically aligned even though the nanowire density is significantly lower compared with that of GaN nanowires. This could be either ascribed to the large surface migration rate of In, or a different growth mechanism that needs to be further investigated.

---

[10] It is also suggested that there should be *no* fundamental difference between the mechanism of growing GaN/InN nanowires directly on Si substrate and that on amorphous template. The surface roughness of amorphous template could play a role in a manner that assists the initial nucleation process and may only change the shape of the initial 2D nuclei.

2.5. The importance of III-nitrides grown by MBE to industrial applications

Nowadays, the commercialized In(Ga)N planar structures are generally grown by metal organic CVD technique, which has been a great success. However, the metal organic CVD growth technique has drawbacks: it requires the use of large amount of ammonia and high growth temperature. The consequence of high growth temperature is the presence of large dislocation density and polarization field, as well as poorly controlled heterointerface, caused by the thermal mismatch between In(Ga)N planar structures and the underneath substrates during the cooling process. This severely limits the device performance. In addition, the high growth temperature makes it difficult to incorporate high In concentration, which makes In-rich material *not* possible to grow. Reducing the growth temperature as well as seeking ammonia-free process is urgent.

In this regard, within the territory of metal organic CVD, researchers at Meaglow Ltd. have developed a special technique, i.e., using the ammonia-free migration enhanced deposition with the aid of a plasma source, to grow high-quality In(Ga)N planar structures in a CVD environment at low temperatures.(*206-208*) The biggest advantage of this technique is that, it can scale the high-In-content-compatible growth up to a large area at a *low* cost. However, these growths are normally done in a nitrogen extremely-rich environment, which inevitably creates a significant amount of nitrogen related defects;(*206-208*) this reduces the optical performance drastically. Another completely different avenue might be needed to further push the device performance to a longer wavelength.

The MBE grown III-nitrides, in contrast, have a number of advantages. Firstly, high In concentration becomes much easier to achieve, due to the low growth temperatures. Secondly, the ultrahigh vacuum environment can increase the material quality significantly. For example, the MBE grown Mg-doped III-nitrides do not need annealing to activate *p*-type conductivity, due to the much reduced hydrogen incorporation. Thirdly, the interface properties can be controlled precisely, which is critical for many electronic and photonic device applications.

In addition, with the rapid development of MBE technology, MBE growth can be scaled up: the use of MBE system to grow large-area wafer (up to 12 inch) has been very mature, and more importantly, the throughput now is comparable to that by metal organic CVD system.

Lastly, MBE now is widely used in industry for the production of III-V electronic and photonic devices, as well as the emerging low-dimensional semiconductors such as quantum dots and nanowires. For example, as will be shown in this thesis work, MBE has a huge advantage in growing high-quality Wurtzite III-nitride nanowires. All these attributes together will provide an entirely new avenue for realizing high-efficiency III-nitride electronic and photonic devices and systems by MBE.

3. Characterization methods of InN, and other semiconductor nanowires and heterostructures

Characterizing material properties experimentally is a rich and important scientific area; and performing the structural, electrical and optical characterization of compound semiconductors and their heterostructures is of critical importance to optimize the growth process and to realize high performance devices.

For instance, to determine whether a new material or a new structure is useful or not, the material designer or the sample grower has to characterize the intrinsic material properties such as the optical bandgap, the free carrier concentration, and the electron drift mobility, etc.. Moreover, for samples grown by highly complex systems such as MBE, the material quality might vary from each growth as well as from position to position in the same sample. In this case, the grower also needs these important parameters as instant feedback to track sample quality and to optimize the growth process.

Compared with the characterization of bulk semiconductors, characterizing the structural, electrical, and optical properties of semiconductor nanowires faces a number of challenges. For example, the Hall measurements can be performed on bulk materials to estimate free carrier concentration, but for nanowires such a method is *very difficult* due to the challenge in making electrical contacts to nanowires in a manner that satisfy the requirements for the Hall measurements.

3.1. An overview

In this thesis work, different characterization methods are employed, which involves:

a) **Structural characterization** – such as the *scanning electron microscopy* (SEM) that produces the images of microstructures by scanning them with a focused electron beam, and the *transmission electron microscopy* (TEM) in which ultrahigh energy electrons are transmitted through an ultra-thin sample so that the atomic structure can be pictured.

b) **Optical characterization** – such as the *X-ray photoelectron spectroscopy* (XPS) that utilizes high-energy electrons to bombard a sample so that the chemical bonds and electronic states can be revealed from the photo-excited electrons, the *photoluminescence* (PL) spectroscopy where the incident photons are absorbed by a semiconductor that subsequently produces light emission due to the radiative recombination of photo-generated electron-hole pairs, and the *Raman scattering* in which the incident light is scattered by lattice vibration.

c) **Electrical characterization** – wherein a nanoprobe is utilized in an SEM environment to probe the electrical transport properties of semiconductor nanowires.

In the rest of this chapter, we will focus on the heavily involved characterization methods in this thesis work. They are: the optical characterization methods that include XPS, PL, and Raman spectroscopies; as well as the electrical characterization method – the electrical nanoprobing in an SEM environment.

3.2. Optical characterization

In general the interaction between light (electromagnetic radiation) and solids have three major consequences: elastic/inelastic scattering, absorption with electrons excited, and absorption with photons emitted. Therefore, studying the interaction between light and solids can provide a lot of useful information of solids.

For example, by using very short wavelength X-rays (on the order of the crystalline lattice constant, namely, a few angstroms) and examining diffraction pattern created by scattering, crystalline structure can be determined. By increasing the wavelength of X-rays and examining the photo-excited electrons, the information such as the chemical bonds and electronic states can be determined. By further increasing the wavelength and using light with wavelengths from the ultraviolet to the visible or infrared, almost all aspects of a semiconductor can be examined, e.g., crystal lattice information can be determined from the light scattering by phonons, or electronic band structure including bandgap, impurity energy levels and defect states can be estimated from the light absorption/scattering by electrons, holes, and ions.

3.2.1. Advantage of optical characterization

Optical characterization, as an important counter-partner to electrical characterization, has a number of advantages, especially for sample growers. First of all, optical characterization does *not* need electrical contacts, which is a very time-consuming and expensive process, and difficult sometimes. For example, making electrical contacts to semiconductor nanowires normally needs numerous procedures from nanowire dispersing, coating photoresist, e-beam lithography, photoresist development, to chemical treatment of nanowire surface, electron beam evaporator metal deposition and metal liftoff. In addition, such nanowire contact process may damage nanowire surface. Actually, making electrical contacts, sometimes limits the study of material properties. For example, it is very challenging to perform Hall measurements on nanowires because of the difficulty in making contacts, due to the nanowire geometry.

Secondly, optical beam is easily manipulated, so that a specific region of the investigated sample, either a micro-size spot, or a nanometer-size depth under the surface, can be probed effectively. This is in contrast with electrical characterization, wherein only an average effect of the sample can be studied.

For the above reasons, optical characterization is generally able to provide a much faster and efficient feedback on material quality and uniformity, as well as the correlation with growth parameters for sample growers.

3.2.2. X-ray photoelectron spectroscopy

X-ray photoelectron spectroscopy (XPS), also known as ESCA (Electron Spectroscopy for Chemical Analysis), is a powerful surface/near-surface analysis technique that measures chemical composition, chemical bonds, as well as electronic states for a given material. XPS spectra are normally obtained by exciting a material with an X-ray beam while simultaneously measuring the kinetic energy and the count of electrons that are excited from the material within 1 nm to 10 nm in the near-surface region. The electron excitation process is schematically shown in Figure 3-1, where E_{vac} is the vacuum energy level, E_F is the Fermi-level, ϕ is the work function (the energy difference between E_{vac} and E_F), and E_B is the binding energy (the energy needed for an electron jump to the Fermi-level). In this case, the kinetic energy (*K.E.*) of the electron excited from the sample (*not* the instrument-measured *K.E.*) is: $K.E._{(sample)} = hv - E_B - \phi_{(sample)}$.

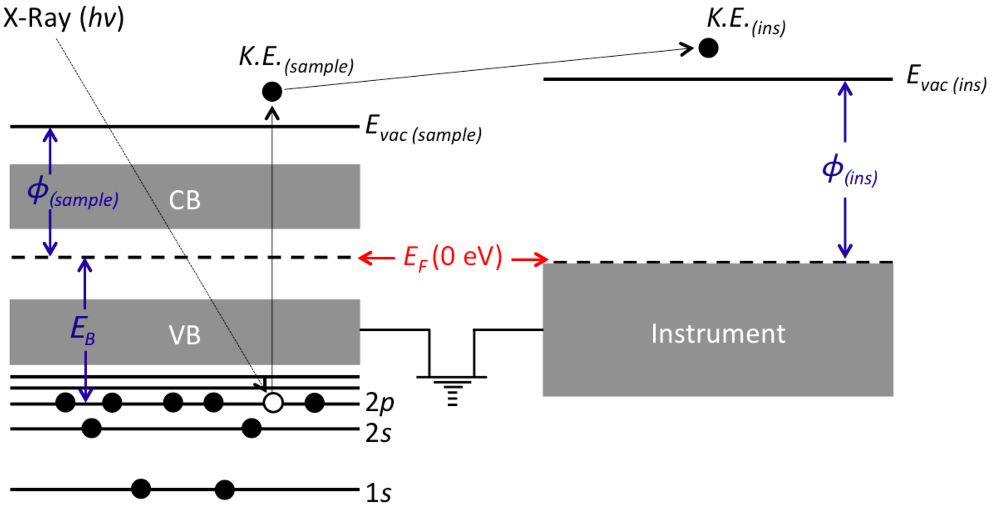

Figure 3-1 A schematic plot of the principle of X-ray photoelectron spectroscopy in studying a semiconductor material.

Since nearly all information from XPS is derived through the electron kinetic energy, a reference energy level is needed. This is the most critical point for all XPS experiments. In general, for a material in a gas phase, the only reference point is the vacuum energy level (E_{vac}); while for a solid phase there is a second reference point: the Fermi energy level or Fermi edge (E_F). *However, if using E_F as the energy reference, it is critical that the sample is grounded, and* *the ground has to be the same as that of the instrument.*[11] *In this case, the Fermi-level is set at 0 eV.*

The band alignment of the sample and instrument is shown in Figure 3-1 when they have the *same* ground. In this case, the instrument measured electron kinetic energy is: $K.E._{(ins)} = h\nu - E_B - \phi_{(sample)} - (\phi_{(ins)} - \phi_{(sample)}) = h\nu - E_B - \phi_{(ins)}$. Therefore, the binding energy E_B relative to the Fermi-level can be determined by: $E_B = h\nu - K.E._{(ins)} - \phi_{(ins)}$, where the parameters in the equation right side can be experimentally measured, and for modern XPS systems $\phi_{(ins)}$ is typically very small. By analyzing binding energies of different electron species one can derive a lot of useful information of the sample such as:

- **a)** Chemical element identification and related chemical states/bonds by characterizing energy peak positions
- **b)** Chemical composition/chemical formula by characterizing relative peak intensities
- **c)** Valence band structure

The sample-grounding requirement does not cause problems for conductive samples, in which the calibration by the core energy levels (such as Cu-$2p_{3/2}$, Ag-$3d_{5/2}$, and Au-$4f_{7/2}$ peaks) of the metals on the sample holder is sufficient to correct the Fermi-level shift. However, if the samples are *not* highly conductive, such as nondoped or Mg-doped InN nanowires in this work, the charging effect[12] is inevitable, so that the Fermi-level determined through the calibration by Cu-$2p_{3/2}$, Ag-$3d_{5/2}$, and Au-$4f_{7/2}$ peaks needs to be carefully analyzed and corrected. In this case, another peak is normally used as internal calibrator (inherent to the

---

[11] This is also the reason that for a gas material E_F cannot be the reference point since one cannot ground a material in a gas phase.

[12] The electrons are excited from the sample so that the positive charges are left. If the grounding is not good, then these positive charges will be left, to shift the Fermi-level of the sample to a higher energy level. Low-energy electron flood gun can be used to remove these positive charges. However, an internal calibrator such as C-1*s* (285.0 eV) is normally used to calibrate the Fermi-level shift as a more accurate approach.

sample). It is the C-1*s* peak (285.0 eV), arising from the adventitious carbon.[13] Such adventitious carbon originates from the adsorption of aliphatic hydrocarbons from the atmosphere.

Characterization of valence band spectra of InN nanowires – The XPS experiments in this thesis work were performed in a Thermo Scientific Al *K-α* (1486.295 eV) system, with a monochromatic beam size in the range of 30 to 400 μm. The valence band spectrum, or the valence region of the whole XPS spectrum,[14] is of special interest to this thesis work. The sample is grounded so that the Fermi-level is at 0 eV. A low-energy flood gun is turned on during the measurements so that the charging effect can be removed. Additionally, both Au-$4f_{7/2}$ and C-1*s* peaks were calibrated to correct the Fermi-level shift due to the charging effect, if there is any, to make sure the derived energy is with the best accuracy.

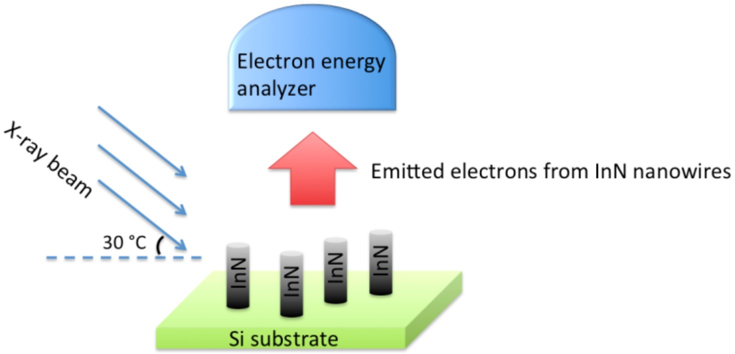

Figure 3-2 A schematic plot of using X-ray photoelectron spectroscopy to study InN nanowire surface.

Moreover, in order to minimize the influence from Si substrate, the X-ray beam impinges upon the nanowires at a 60-degree angle with respect to the nanowire *c*-axis. The resulting photoelectrons are collected by an electron energy

---

[13] A thin layer of carbonaceous material is usually found on the surface of most air-exposed samples, this layer is generally known as adventitious carbon.

[14] The valence band spectrum function was enabled in this case, to increase the accuracy by only collecting the low-energy electrons, since in a strict meaning XPS is only sensitive to the high-energy core-level electrons (1s, 2s, etc.), not the low-energy valence band electrons.

analyzer above the nanowires (near-zero take-off angle). A simplified schematic plot is shown in Figure 3-2. It can be seen that the X-ray impinges upon the InN nanowire sidewalls with the photoelectrons collected at a near-zero take-off angle. This measurement configuration ensures that the majority of the signal is derived from the InN nanowire sidewalls.

3.2.3. Photoluminescence spectroscopy

Luminescence, in general, is a light emission from a substance due to an external excitation, such as Joule heating, electrical current injection, or light irradiation. In semiconductors, studying luminescence is an efficient probe to the excited electronic states, which, in conjunction with electrical transport phenomena, can reveal the fundamental electrical and optical properties of semiconductors such as the electronic states, and the population of electrons/holes associated with each state in semiconductors.

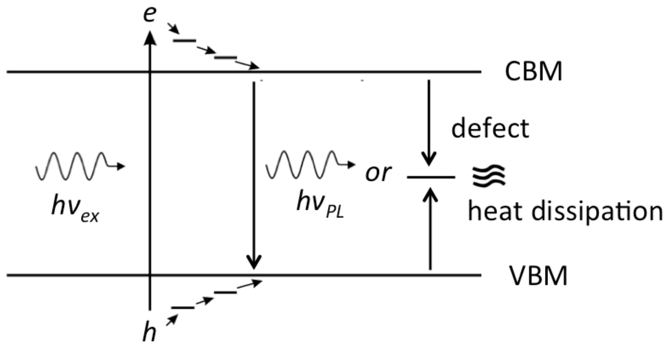

Figure 3-3 A schematic plot of carrier recombination process in a semiconductor due to absorbing a photon.

In this work, photoluminescence, where the light emission is due to the absorption of photons, is employed as a probe to study the electronic states, energy levels, as well as carrier distribution in InN nanowires. In this process, as shown in Figure 3-3, due to incident photons (with energy $hv_1 □ E_g$, where E_g is the bandgap energy), electrons will be excited into the conduction band, with holes being left in the valence band. The carrier radiative recombination lifetime is in general much longer compared with the carrier relaxation time, so that the photo-generated electrons and holes will have enough time to relax towards the conduction band and valence band edges, to recombine either radiatively to give light emission, or nonradiatively to give heat dissipation if they are trapped by defects in the bandgap.

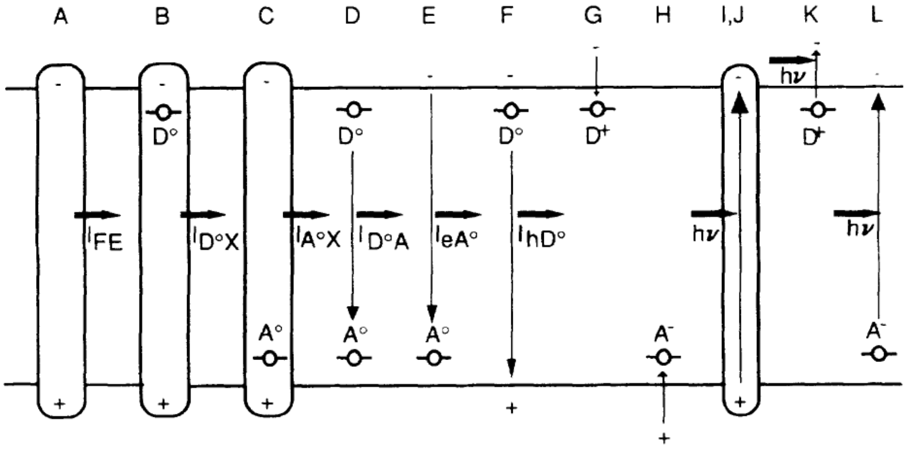

Figure 3-4 Near-band-edge radiative and nonradiative recombinations of the photo-generated electron-hole pairs,[15] with (A) Free-exciton emission, (B) donor bound exciton emission, (C) acceptor-bound exciton emission, (D) donor-acceptor pair recombination, (E) radiative recombination of free electrons and neutral acceptors, (F) radiative recombination of free holes and neutral donors, (G) nonradiative recombination between free electrons and ionized donors, (H) nonradiative recombination between free holes and ionized acceptors, (I) the excitation of electron-hole pairs by above-bandgap laser light (i.e., $h\nu > E_g$), (J) the resonant formation of free excitons with $h\nu \sim E_g$, (K) the excitation of electrons from neutral donors, and (L) the excitation of electrons from ionized acceptors.(*209*)

However, the actual electron-hole recombination processes in semiconductors are in general complicated due to the presence of shallow defect donor/acceptor energy levels, or excitonic states formed by electron-hole

---

[15] It should be noted that Mahan exciton emission as discussed in Chapter 1 does not fall in any category here since in Mahan exciton emission process, the electrons in conduction band are far away from the conduction band edge.

interaction. These effects will modify near-band-edge transitions. In addition, the recombination processes will be affected by the presence of phonons (to produce phonon replica or phonon sideband emission) and the Fermi-level being pinned deep in the conduction band (to produce Mahan exciton emission). All these aspects will affect the electron-hole recombination process and the PL properties significantly. As an example, Figure 3-4 schematically shows the electron-hole recombination process for *near-band-edge* transitions, including both radiative and nonradiative recombinations.

In practice, the light emission requires radiative recombination outwins nonradiative recombination, wherein Joule heat is dissipated. This can be, in one way, technically achieved by increasing the incident light intensity so that more electron-hole pairs are generated. Besides using high power lasers, another approach to increase the incident light intensity is to reduce the incident beam size, i.e., performing micro-PL experiments. Additionally, by using micro-PL, the inhomogeneous broadening caused by the nanowire size distribution will also be significantly reduced, rendering a much narrower PL spectral linewidth that is more closely related to the intrinsic electrical and optical properties of the material.

Fundamentally, the PL properties are closely related to the photo-excited carriers in a solid, such as the correlation between PL spectral linewidth and total carrier density.[16] Therefore, by using extreme low excitation conditions, free carrier concentration (the so-called background doping concentration) can be crudely estimated by PL spectral linewidth. In InN, the PL spectral linewidth as a function of the free carrier concentration is calculated by Moret *et al.*.(*210*) As shown in Figure 3-5, if assuming zero inhomogeneous broadening, for a linewidth ~100 meV, the free carrier concentration is estimated to be ~10^{18} cm^{-3}.

---

[16] This total carrier density includes the residual electron density (the so-called background doping concentration, or the free carrier concentration as mentioned in this thesis) and the photo-generated electron density. By using extremely low excitation conditions, one can minimize the photo-generated electron density.

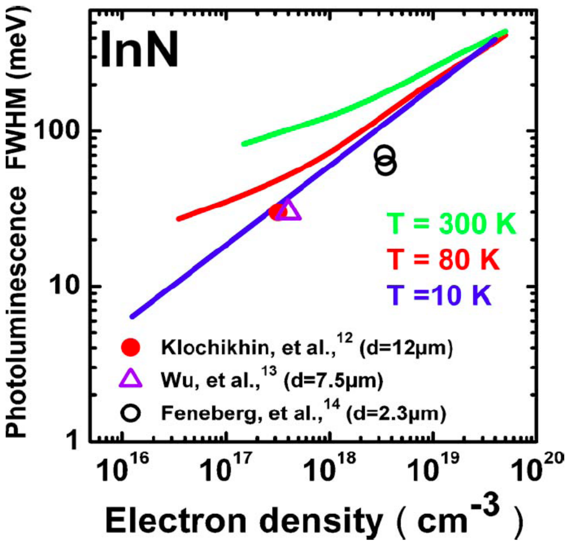

Figure 3-5 Relationship between free carrier concentration and PL spectral linewdith with zero inhomogeneous broadening, from Ref. (*210*). The solid lines are theoretical calculations.

It is worth mentioning, however, that the free carrier concentration determined by the PL spectral linewidth is highly dependent on the measurement conditions, such as excitation power, beam size, and sample geometry. Therefore, this approach is not a straightforward method compared with electrical measurements. In this regard, electrical characterization (Section 3.3) would be more accurate to estimate free carrier concentration, electron mobility, etc..

PL setup for measuring InN nanowires – Illustrated in Figure 3-6 is a homemade temperature variable micro-PL system. InN nanowires were optically excited using a semiconductor diode laser (λ = 635 nm) with a 100× objective. The beam size is ~5 μm. The emitted light from InN nanowires (through the same 100× objective) was spectrally resolved by a high-resolution spectrometer, and detected by a liquid-nitrogen-cooled InGaAs detector (with a cut-off wavelength of ~2.2 μm). The signal was collected with a single channel lock-in amplifier. All the PL measurements were performed on non-tapered nanowires.[17]

---

[17] The PL spectra of tapered non-doped InN nanowires show a little trace of the near-surface region emission (see Chapter 6 for the near-surface region emission). The PL

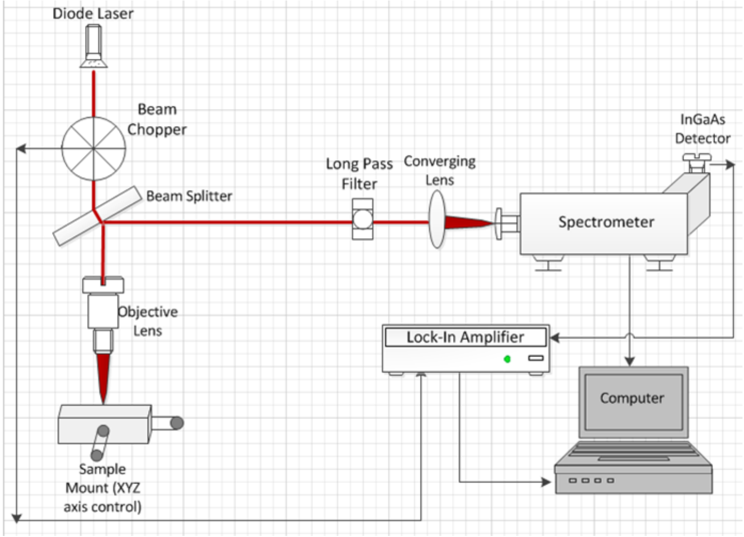

Figure 3-6 A schematic plot of the homemade temperature variable micro-photoluminescence setup (courtesy of Shouvik Mukherjee).

3.2.4. Raman scattering spectroscopy

Different from the previous two optical characterization methods where light absorption is involved, Raman scattering deals with the *inelastic* scattering of light, in which the energy of scattered photons is different from that of incident photons (e.g., the momentum change) with $\Delta E = h \cdot \Delta \nu$. The phenomenon of inelastic scattering of light was first proposed by Smekal in 1923,(*211*) and was first observed by Raman and Krishnan experimentally in 1928.(*212*) In Raman experiments, $\Delta \nu$ has a practical unit as cm^{-1}.[18] It is worth mentioning that Raman scattering is a very weak process so that only one in every 10^6-10^8 photons will be scattered through Raman process, while the majority of photons pass the sample with elastic scattering, or Rayleigh scattering.

---

spectra of tapered Si-doped InN nanowires interestingly do not exhibit a significantly higher energy peaks compared with non-tapered Si-doped InN nanowires (see Chapter 6), but exhibit much weaker PL intensity due to the enhanced nonradiative recombination rate.

[18] The frequency change of the incident light can be expressed as $\Delta \nu = c / \Delta \lambda$. In describing Raman scattering experiments, the speed of light is generally normalized for a historical reason. In this case, the frequency change is expressed in the inverse wavenumber (unit of cm^{-1}); and 1 eV = 8,000 cm^{-1}. In addition, in a strict meaning the frequency change should be expressed as Δcm^{-1}.

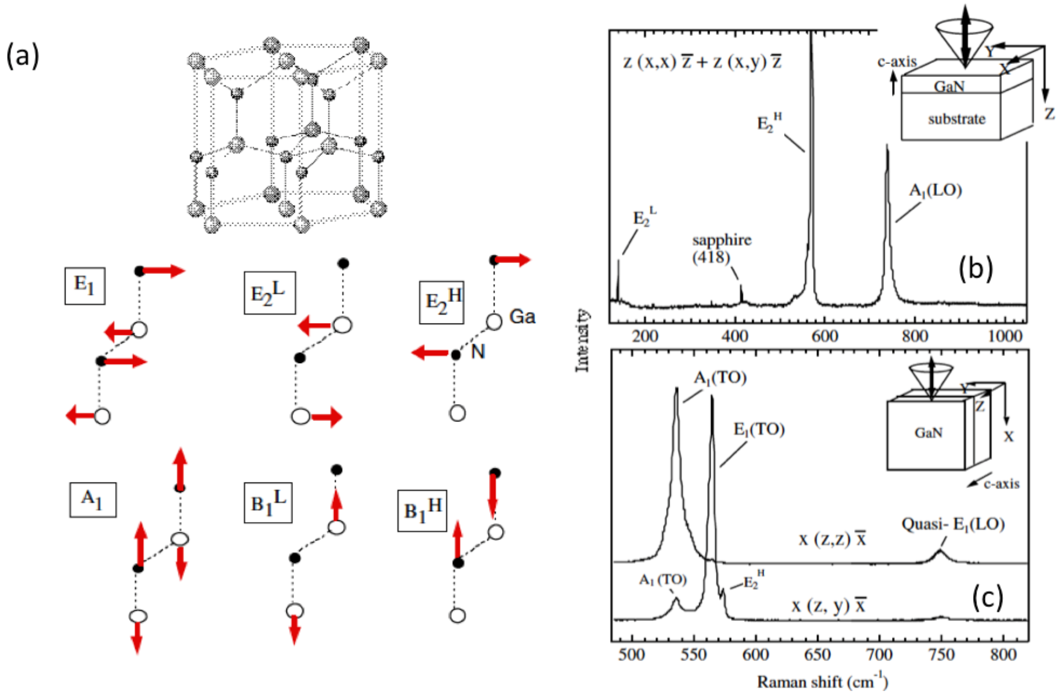

Figure 3-7 (a) Optical phonon modes in a Wurtzite structure; shown is GaN for an example. In has the same site as Ga. (b) and (c) The Raman shift peaks related to each optical phonon mode with different incident light directions.(*213*)

Raman scattering is a very effective tool to study low-energy states in solids, and the most common and important light scattering source is phonon (the quantum of lattice vibration). In general, for a Wurtzite crystal structure, at the Γ point (Brillouin zone center), phonon modes can be irreducibly presented by: $\Gamma_{ac}+\Gamma_{op}=(A_1+E_1)+(A_1+2B_1+E_1+2E_2)$, where the terms in the first brackets are acoustic phonon modes and the terms in the second brackets are optical phonon modes. Figure 3-7(a) shows the optical phonon modes in a Wurtzite structure, where the two B_1 modes are silent modes, the two E_2 modes are only Raman active, and the A_1 and E_1 modes are both Raman and IR active. Therefore, by investigating the Raman shift peaks one can determine the crystal structure, such as the peaks shown in Figure 3-7(b) and (c) indicating a Wurtzite structure.

Additionally, the detailed phonon properties can be revealed by Raman scattering experiments such as phonon lifetime and phonon decay.(*214*) Understanding phonon properties, as well as their influence on electrical and optical properties, is of practical importance to reduce the “hot phonon effect”, which in a lot of circumstances reduces the lifetime of electronic and photonic devices.

Optical phonon modes in InN – The optical phonon modes in InN have been investigated extensively by Raman scattering spectroscopy.(*92, 94, 95, 214-219*) The wavenumbers for all the six Raman-active optical phonon modes are: E_2^L = 87 cm^{-1}, E_2^H = 488 cm^{-1}, A_1(TO) = 447 cm^{-1}, A_1(LO) = 586 cm^{-1}, E_1(TO) = 476 cm^{-1}, E_1(LO) = 593 cm^{-1}.(*92*)

Furthermore, if the surface electron accumulation is present on InN surface, there will also exist the longitudinal optical phonon-plasmon coupling modes (L^+, L^-), with L^- in the range of 400-450 cm^{-1} and L^+ very close to the wave numbers of uncoupled LO modes.(*92, 95, 215*) Therefore, by investigating the Raman scattering spectroscopy, the surface electron accumulation, as well as free carrier concentration can be studied.(*149*)

Raman scattering setup for InN nanowires – The Raman scattering experiments were performed at room temperature. In these experiments, InN nanowires were excited with an external 488 nm Argon ion laser, and the estimated power on the sample is about 40-50 mW with a spot size about 0.5–1 μm. The signal was detected by a Synapse CCD air-cooled detector. In this configuration, the incident light is in parallel with the hexagonal *c*-axis of the nanowires.

3.3. Electrical characterization

Optical characterization, however, also has a number of limitations such as it cannot determine free carrier concentration and electron mobility accurately. This can be perfectly compensated by electrical characterization. *Electrical characterization deals with transport phenomena in solids.*[19]

---

[19] Generally speaking, the motion of carriers (i.e., electrons, holes, ions, etc.) under the influence of external forces (i.e., electric field, magnetic field, thermal gradient) or density gradient (i.e. in case of diffusion) gives rise to the so-called transport phenomenon. For example, carriers can transport electric charge to give electrical current (electrical transport), or transport phonons to give heat dissipation (thermal transport).

Electrical characterization, as an important counter-partner to optical characterization, provides a more accurate estimation of the electrical transport properties associated parameters such as resistivity, free carrier concentration, and electron mobility. *The measurement of charge carrier transport properties of semiconductor nanowires, including carrier type, carrier concentration, and carrier mobility is critical for the design and performance of a wide range of nanowire devices.*

3.3.1. Electrical transport of bulk semiconductors:[20] The experimental approach and properties

When an electric field (or a current) is applied to a bulk semiconductor, the resistivity/conductivity can be measured from the configuration as shown in Figure 3-8(a). Furthermore, by applying a *z*-axis magnetic field and using side contacts (shown in Figure 3-8(b)) the Hall effect can be measured, from which carrier concentration (as well as carrier type), hence carrier mobility can be determined. Besides the Hall measurements, capacitance voltage measurements can be used to study electrical transport properties.(*65, 75, 107, 111, 220, 221*)

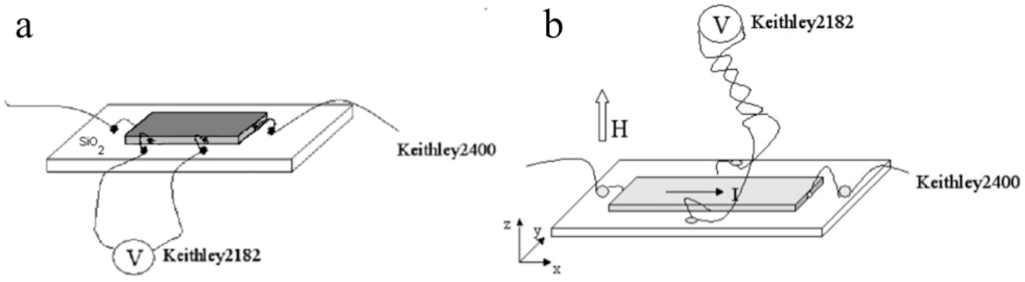

Figure 3-8 Schematic plots of characterizing electrical transport properties of a bulk semiconductor, with (a) the in-plane resistivity, and (b) the Hall effect measurements.

In addition, when a large electrical field is applied to a bulk semiconductor with low free carrier concentration, the electrical conduction will be driven from

---

[20] Here we discuss semiconductors with *low* free carrier concentration.

the ohmic conduction to the space-charge-limited (SCL) conduction.(*222-224*) The SCL current, characterized by a square law dependence on the applied voltage ($I \propto V^2$), has been measured when the injected charge carrier concentration exceeds the free carrier concentration in a solid that is relatively free of charge traps and biased through an ohmic contact.(*222*) With the presence of charge traps, however, the SCL current can be significantly reduced, or even distorted, showing a higher power dependence on the applied voltage ($I \propto V^{\beta}$, with $\beta > 2$) for charge traps distributed over a broad energy range.(*222-224*)

Therefore, a thorough investigation of the SCL conduction, together with the correlation to the ohmic conduction under low biasing conditions, can provide critical information on free carrier concentration, electron mobility, and charge trap characteristics.(*222-224*)

3.3.2. Electrical transport of semiconductor nanowires: The challenge, experimental approach, and properties

Similar to a bulk semiconductor, the resistivity/conductivity of a semiconductor nanowire can be derived by the 4-point contact method, or 2-point contact if the contact resistance is much less than the nanowire resistance. Free carrier concentration, however, *cannot* be straightforwardly derived from the Hall effect measurements due to the much-reduced dimension, so that 4-point (as shown in Figure 3-8(b)) contacts are very difficult to make.

In this regard, the electrical transport properties (such as electron concentration and electron mobility) of semiconductor nanowires have been commonly analyzed by studying the characteristics of nanowire field effect transistors.(*127, 128, 225-227*). Figure 3-9(a) shows an InN nanowire field effect transistor as an example, wherein two metal contacts serve as source and drain. In this configuration, the electron mobility μ can be determined by $\mu = g_m \cdot L^2 / (C \cdot V_{SD})$, where g_m is the transconductance, L is the channel length, V_{SD} is the source-drain voltage, and C is the capacitance at the pinch-off point, which is closely related to the thickness of the underneath oxide t_{ox}. The electron concentration therefore can be determined by $n = 1/(\rho e \mu)$, where ρ is the resistivity of the nanowire.

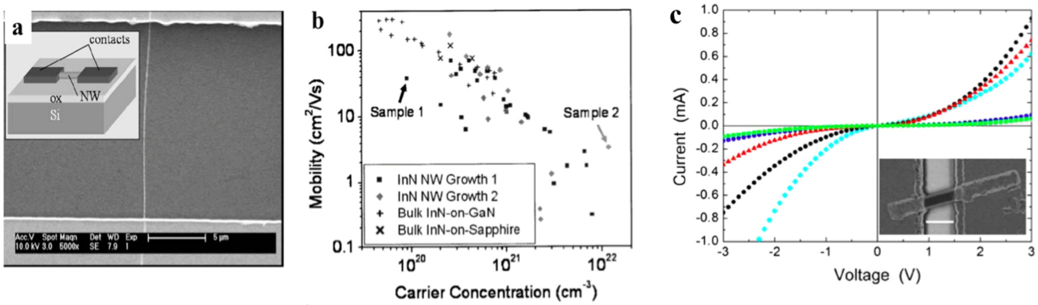

Figure 3-9 (a) A InN nanowire field effect transistor, and (b) the derived electron mobility and electron concentration dependence.(*151*) (c) The space-charge-limited conduction in GaN nanowires.(*228*)

Figure 3-9(b) shows the derived electron mobility and electron concentration dependence from InN nanowires grown by the VLS mechanism using a CVD technique. It can be seen that the electron concentration is extremely high, and the electron mobility is very low, which can be ascribed to the strong *n*-type characteristics as discussed in Chapter 1.

When the source-drain voltage is increased, similar to bulk semiconductors, the conduction of semiconductor nanowires is also driven from the ohmic conduction to the SCL conduction,[21] as shown in Figure 3-9(c) for GaN nanowires as an example. Such SCL conduction has been prevalently observed in semiconductor nanowires and heterostructures such as GaN,(*229*) GaAs,(*230*) GaSb,(*231*) InAs,(*232*) and AlGaN/GaN core-shell structures.(*233*) However, compared with the SCL conduction in bulk semiconductors, the SCL conduction in semiconductor nanowires is further enhanced, due to the large aspect ratio and

---

[21] In nanowire field effect transistors, applying a large source-drain voltage, however, sometimes burns out the semiconductor nanowires. In contrast, as we will discuss later on, with the nanoprobing technique, high voltage can be easily applied without burning out the nanowires.

the reduced Coulomb screening. In this case, a nanowire geometry related scaling factor $\zeta(R/L)$ should be included in the SCL conduction theory.(*228*)

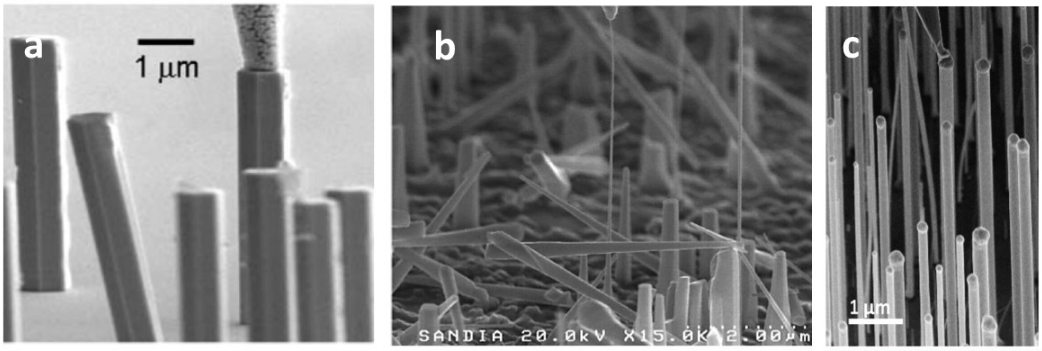

Figure 3-10 Nanoprobing various semiconductor nanowires in an SEM environment, with (a) GaN nanowires,(*229*) (b) InAs nanowires,(*232*) and (c) GaAs nanowires.(*230*)

3.3.3. Nanoprobing: A new technique to study the electrical transport properties of semiconductor nanowires

During the fabrication of nanowire field effect transistors, a significant amount of chemical treatments, as well as high-energy electron beam exposure are involved, which inevitably changes the surface states of semiconductor nanowires drastically. A better approach is needed.

Recently, a new method has been explored to investigate the electrical transport properties of semiconductor nanowires. It utilizes a nanoprobe in an SEM environment to measure the electrical conduction of individual semiconductor nanowires.(*228-230, 232*) Figure 3-10 shows such nanoprobing to various semiconductor nanowires. This technique provides the distinct advantage that the surface and interface properties of semiconductor nanowires are not perturbed by any chemical treatment or electron-beam lithography process, thereby offering a more efficient approach to characterize the electrical transport properties of semiconductor nanowires.

In this thesis work, such nanoprobing technique was employed to study the electrical transport properties of InN nanowires. The experiments were performed at the 4D LABS, Simon Fraser University, B.C., Canada.

4. Demonstration of intrinsic InN nanowires (I): Direct evidence from optical characterization and their optical properties

In this chapter, it is demonstrated through XPS and micro-Raman scattering experiments that, *intrinsic* InN nanowires can be achieved. In such intrinsic InN nanowires, the near-surface Fermi-level was measured to locate below the CBM, suggesting the absence of electron accumulation on the lateral surfaces. Additionally, the PL characteristics of intrinsic InN nanowires were studied in details. An extremely narrow PL spectral linewidth (~9 meV) was measured at 10 K, and the trace of free-exciton emission was also observed. Moreover, phonon sideband emission peak was detected, confirming the superior sample quality. These PL characteristics can be well correlated with the absence of surface electron accumulation.

4.1. The absence of surface electron accumulation on the *grown* non-polar surfaces

The surface charge properties of non-doped InN nanowires were investigated directly by the angle-resolved XPS. Illustrated in Figure 4-1 is the measurement of the near-surface Fermi-level (E_F) relative to the position of the VBM. It can be seen that the near-surface E_F lies at ~0.4 to 0.5 eV above the VBM, suggesting the *absence* of electron accumulation and minimal downward band bending on the sidewalls of InN nanowires. This near-surface Fermi-level is also very close to the intrinsic Fermi-level (E_{Fi} ~ 0.38 eV) in InN if taking $m_e^* = 0.05m_0$ and $m_h^* = 0.65m_0$.(*111, 234, 235*) Furthermore, highly symmetric In-3$d_{5/2}$ and N-1*s* XPS spectra peaks (shown in the inset of Figure 4-1(a)) suggest a negligible level of impurity bonds (such as In-O, N-H or N-C) associated with the surface electron accumulation.(*236*) To the current knowledge, this is the *first* demonstration that the surface 2DEG formation and E_F pinning is absent on the non-polar *grown* surfaces of any InN structure.

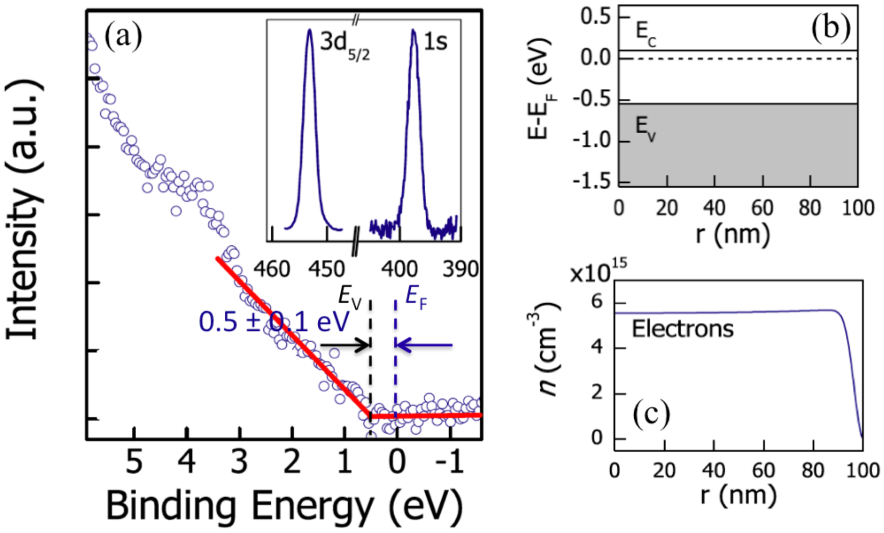

Figure 4-1 (Clockwise) Angle-resolved XPS spectra and *ab*-initio calculation of intrinsic InN nanowires. (a) Angle-resolved XPS spectra were measured from the lateral surfaces (*m*-planes) of [0001]-oriented non-doped InN nanowires, showing an energy separation of ~0.5 eV between the VBM and the near-surface E_F. The inset of (a) shows the photoelectron spectra of In-3$d_{5/2}$ and N-1*s* orbitals measured from the lateral surfaces. The surface band structure and electron distribution are modelled by performing self-consistent effective mass calculation of a 200 nm diameter InN nanowire. Intrinsic InN nanowires are characterized by the absence of surface band bending (shown in (b)) and surface 2DEG (shown in (c)).

This behaviour can be further captured through a self-consistent effective mass model,(*237*) where the time-independent Schrödinger equation was solved self-consistently assuming an effective mass of $0.055m_0$, a relative dielectric constant of 13, and a cylindrical symmetry. As shown in Figure 4-1(b) and Figure 4-1(c), under uniform near-intrinsic doping level − less than 5×10^{15} cm^{-3},[22] the surface band bending does not occur at the *m*-plane (shown in Figure 4-1(b), juxtaposed against the XPS data in Figure 4-1(a)). This is illustrated by the spatial distribution of the long wavelength electrons that occupy the CBM under the

---

[22] It will be seen later on that this doping level is within the range of estimated average electron concentration from the optical measurements and electrical measurements on intrinsic InN nanowires with a diameter around 200 nm.

near-intrinsic doping level. As shown in Figure 4-1(c), electrons at the CBM pull away from the surface due to quantum confinement and do not form a surface 2DEG but rather partially deplete the near surface region.[23] This observation is in direct contrast to the commonly reported 2DEG that forms at the surfaces of *n*-type degenerate InN nanowires and thin films.

Such absence of surface electron accumulation in intrinsic InN nanowires can be further confirmed by micro-Raman scattering experiments. As shown in Figure 4-2, compared with the spectrum of Si-doped InN nanowires, where a surface electron accumulation associated Raman shift peak L^- appears around 445 cm^{-1},(*94, 149, 150*) the non-doped (intrinsic) InN nanowires do *not* exhibit such peak, which therefore is consistent with the absence of surface electron accumulation.

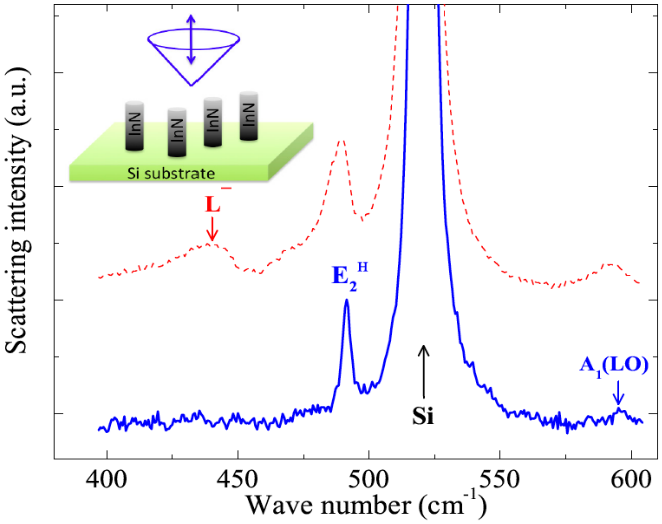

Figure 4-2 Micro-Raman scattering spectrum of intrinsic InN nanowires. The spectrum measured from Si-doped InN nanowires is also shown as a comparison. The inset shows the experimental setup, where the incident light is in parallel with the nanowire *c*-axis.

---

[23] This is based on exactly flat band condition; however, experimentally, the surface could be weakly *n*-type (i.e., a very small downward band bending) even though there is no surface electron accumulation.

Moreover, the peak at ~591 cm^{-1} in intrinsic InN nanowires is significantly weak compared with the normally reported A_1(LO) mode in *nominally* non-doped InN. This peak, however, is significantly enhanced in the presented Si-doped InN nanowires, which could indicate that the strong A_1(LO) mode observed in previous reports from *nominally* non-doped InN could be more dominated by L^+ mode.

In addition, the main Raman shift peak E_2^H, which appears at ~491 cm^{-1}, is significantly narrower in intrinsic InN nanowires compared with that in Si-doped InN nanowires, indicating a lower free carrier concentration. This low free carrier concentration will be further estimated by the PL spectral linewidth as discussed in section 4.2.1 and the nanoprobing technique in Chapter 5.

4.2. Photoluminescence properties of intrinsic InN nanowires

The previous PL studies on tapered InN nanowires measured broad PL spectra with the linewidth in the range of 50 to 100 meV,(*126, 146*) and the recombination mechanism was believed to originate from Mahan exciton emission.(*86, 90*) With large free carrier concentration associated effects, the PL properties in intrinsic InN nanowires are *not* clear prior to this thesis work.

We demonstrate in this section that in intrinsic InN nanowires, the PL spectrum linewidth can be as narrow as ~9 meV, which is about 5 to 10 times narrower compared with tapered InN nanowires grown by conventional methods.(*126, 132*) Additionally, with much-reduced free carrier concentration in such pristine InN nanowires, the PL mechanism can be ascribed to band-edge emission with free-exciton emission at low excitation conditions. More importantly, phonon sideband emission is also observed for the first time in InN nanowires, further confirming the superior quality of the presented InN nanowires.

4.2.1. The narrow photoluminescence spectral linewidth and extremely low free carrier concentration

The intrinsic (non-tapered non-doped) InN nanowires, in this thesis work, can exhibit an extremely narrow PL spectral linewidth of ~9 meV under an excitation power of ~0.5 μW at 10 K,[24] shown in Figure 4-3. This linewidth is nearly 5 to 10 times narrower, compared to the commonly reported values in *n*-type degenerate InN nanowires and films.(*89, 126, 129, 146*) It is also noted, as further reducing the optical excitation power, the linewidth does not get narrower. There are a few factors, which we believe, can contribute to the ~9 meV linewidth: (1) thermal broadening that scales with *kT*, where *k* is Boltzmann constant, (2) size distribution and the associated inhomogeneity of nanowires, and (3) the presence of defects on the surfaces of each nanowire. In addition, the peak energy position at ~0.675 eV agrees reasonably well with the bandgap of InN in this temperature range.(*4, 63*)

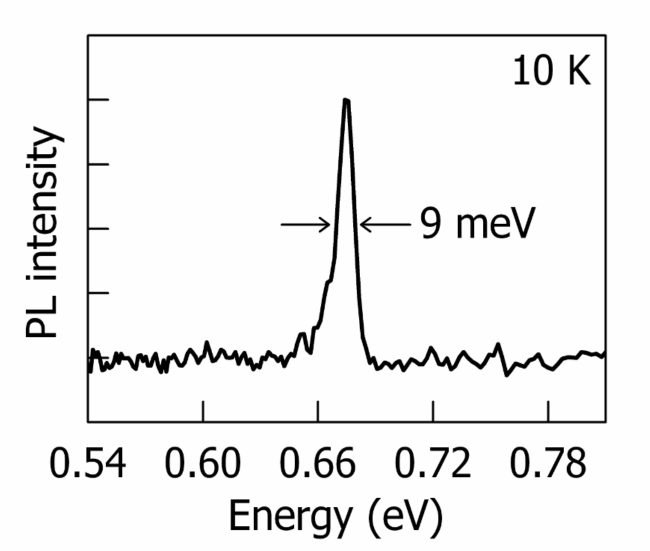

Figure 4-3 The micro-photoluminescence spectrum of intrinsic InN nanowires measured at 10 K under an excitation power of ~ 0.5 μW.

---

[24] The narrowest PL linewidth was achieved on non-doped InN nanowires with lengths of ~ 4 μm.

As discussed in Section 3.2.3, the residual electron concentration of InN can be approximately derived by analyzing the PL spectral linewidth.(*210*) The same approach was employed here. To the first order, for InN nanowires with a PL spectral linewidth (Γ) of ~9 meV, the total electron concentration, n, at 10 K was estimated to be $\sim 2.5\times10^{16}$ cm^{-3} (when the inhomogeneous broadening is neglected). However, by considering the inhomogeneous broadening, Γ_{ih}, a lower value of n can be derived by $n(1-\Gamma_{ih}/\Gamma)^{1/\alpha}$, where $\alpha \approx 0.5$. Assuming an inhomogeneous broadening of ~5 meV (which represents a lower limit on the values normally measured for III-V compound semiconductor nanowires),(*126, 238*) we obtain $n \sim 4\times10^{15}$ cm^{-3}.[25] Since the estimated value may include the residual electron concentration, n_0, and the photo-generated electron concentration, n-n_0, we therefore conclude that such intrinsic InN nanowires exhibit an extremely low residual electron concentration (less than 4×10^{15} cm^{-3}). This value is nearly 2 to 3 orders of magnitude smaller than the commonly reported values in InN nanowires and films. It is also approximately 10 times smaller than the previous reports by Chang *et al.*(*59*) and Jeganathan *et al.*(*93*), and is the smallest value ever reported in any InN structure.

4.2.2. Near-band-edge recombination in intrinsic InN nanowires

Detailed PL emission properties are shown in Figure 4-4. Figure 4-4(a) shows the temperature dependent PL spectra measured under an excitation power of 9 mW. It can be seen that as the temperature increases, the PL peak (E_{PL}^1) shifts to lower energies and the spectra become broader. The derived temperature dependence of E_{PL}^1 is shown in Figure 4-4(b). Such temperature dependent peak energy can be phenomenally fitted by Varshni's equation,(*4*)

$$E_g(T)=E_g(0)-\frac{\alpha T^2}{\beta+T}. \qquad \text{Eq. (4-1)}$$

---

[25] Nevertheless, the derived carrier concentration needs to be further confirmed with direct electrical transport properties measurements, such as via nanowire field effect transistors, or using the nanoprobing technique, which will be discussed in Chapter 5.

where $E_g(0)$ is the fundamental bandgap; α and β are Varshni's coefficients which correspond to the lattice thermal expansion and Debye temperature, respectively. As shown in Figure 4-4(b), the best fit gives $E_g(0) = 0.689 \pm 0.001$ eV, $\alpha = 0.41 \pm 0.02$ meV/K, and $\beta = 449 \pm 32$ K. These values are consistent with those obtained from absorption and PL measurements in InN films, suggesting the nature of this PL peak is related to band-to-band carrier recombination.(*4, 63*) This result is in direct contrast to the nearly temperature invariant PL emission characteristics of *n*-type degenerate InN nanowires.(*126, 129*)

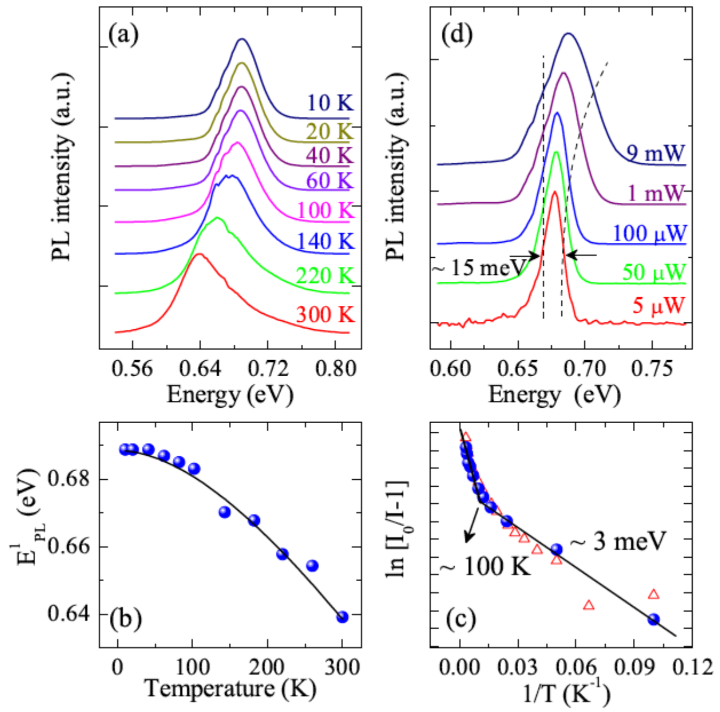

Figure 4-4 (counter-clockwise) (a) The temperature dependent PL spectra of intrinsic InN nanowires measured under an optical excitation power of 9 mW. (b) The temperature dependence of E_{PL}^{1}, solid line is the fitting curve by Varshni's equation. (c) The scaling plot of the integrated PL intensity *I*, as described in the text. (d) The power dependent PL spectra measured at 20 K. The arrows denote the FWHM position, and the dotted lines exhibit the evolution of the FWHM.

It should be noted, however, that the PL peak energy in general is not equivalent to the bandgap energy; it is only approximately valid under very low excitation conditions and in the absence of localized states and band-tailing effect.

Table 4-1 shows the extracted $E_g(0)$, α, and β values measured under different optical excitation conditions, and with different nanowire lengths. It can be seen that in the very low photo-generated carrier concentration regime (with 0.8 μm nanowire length, 1 mW excitation power, and 50 μm beam size), $E_g(0)$ is determined to be ~0.672 eV. This value is consistent with the smallest reported $E_g(0)$ in InN epilayers.(*63*)

Table 4-1 The Varshni's parameters extracted from InN nanowires with different lengths and different optical excitation conditions.

Length, power	$E_g(0)$ (eV)	α (meV/K)	β (K)
0.8 μm, 9 mW	0.689	0.41	449
4 μm, 9 mW	0.674	0.44	445
4 μm, 1 mW	0.674	0.44	502
0.8 μm, 1 mW^a	0.672	0.30	467

^{a} With larger beam size 50 μm.

We have further investigated the variation of the integrated PL intensity as a function of temperature, which provides more insight of the carrier recombination process. As illustrated in Figure 4-4(c), $\ln[I_0/I - 1]$ is plotted as a function $1/T$ under an excitation power of 9 mW, where I_0 is the maximum PL intensity at low temperature, and I represents the integrated PL intensity measured at various temperatures. It can be seen that there exist two distinct slopes, which change at ~100 K (about ~ 8 meV). This slope change temperature sets an upper limit of the exciton binding energy,(*239-241*) which is consistent with the previously reported value ~9 meV from Wu *et al.*.(*4*)

Additionally, the exciton binding energy is suggested to be related to the activation energy derived in the low temperature range (10 to 100 K),(*242, 243*) which is ~3 meV in this study. This small activation energy is consistent with the derived exciton binding energy ~2-3 meV if assuming a relative dielectric constant ε = 13-14, an electron effective mass $m_e^* = 0.05m_0$, and a hole effective mass $m_h^* = 0.3 - 0.65m_0$.(*77, 79*) These studies suggest the recombination process changes from exciton dominated emission at low temperatures to electron-hole plasma emission at high temperatures in intrinsic InN nanowires. Such measurements were also performed on intrinsic InN nanowires with lengths up to ~ 4 μm, which shows similar scaling behavior (see open triangles in Figure 4-4(c)).

Figure 4-4(d) shows the power dependent PL spectra of intrinsic InN nanowires measured at 20 K. At low excitation conditions (< 1 mW), the variation of the integrated PL intensity I with the optical excitation power P can be described by $I = P^{0.99\pm0.18}$. This nearly linear *I-P* dependence further confirms that the PL emission is directly related to free-exciton emission at low excitation conditions.(*209*) At high excitation conditions (> 1 mW), a significant blueshift of E_{PL}^{1}, accompanied by a rapid increase in the PL spectral linewidth was measured, which is consistent with the band-filling effect.(*59*)

It should also be noted that with increasing the optical excitation power, the high-energy sides of the PL spectra become significantly broader (see the dotted curve in Figure 4-4(d)), which is a direct reflection of the E_F shifting into the conduction band. On the other hand, the low-energy sides of the PL spectra do not exhibit any variation with increasing the optical excitation power (see the vertical dotted line Figure 4-4(d)), suggesting the absence or the presence of a negligible level of band-tailing effect and localized states.

4.2.3. Phonon sideband emission

The log-log plot of the low temperature PL spectra reveals another low-energy PL peak.[26] It can be seen from Figure 4-5(a) that two well-resolved emission peaks appear at 6 K under 50 μW excitation, with an energy separation ~70 meV. The high-energy peak is due to the afore-discussed band-to-band recombination. The low-energy peak exhibits an extremely narrow PL spectral linewidth (~9 meV), and the PL peak intensity is about two decades weaker than that of the main PL peak. Moreover, with increasing the excitation power, both peaks get stronger in

---

[26] To resolve the phonon sideband emission peak, the measurements were performed on intrinsic InN nanowires with length ~ 4 μm.

intensity; see the inset of Figure 4-5(a) for the spectrum measured under 500 μW at the same temperature. This can also be seen from Figure 4-5(b), where the low-energy peak is about two decades weaker than the main PL peak over a wide range of the excitation power (50 μW to 3 mW).

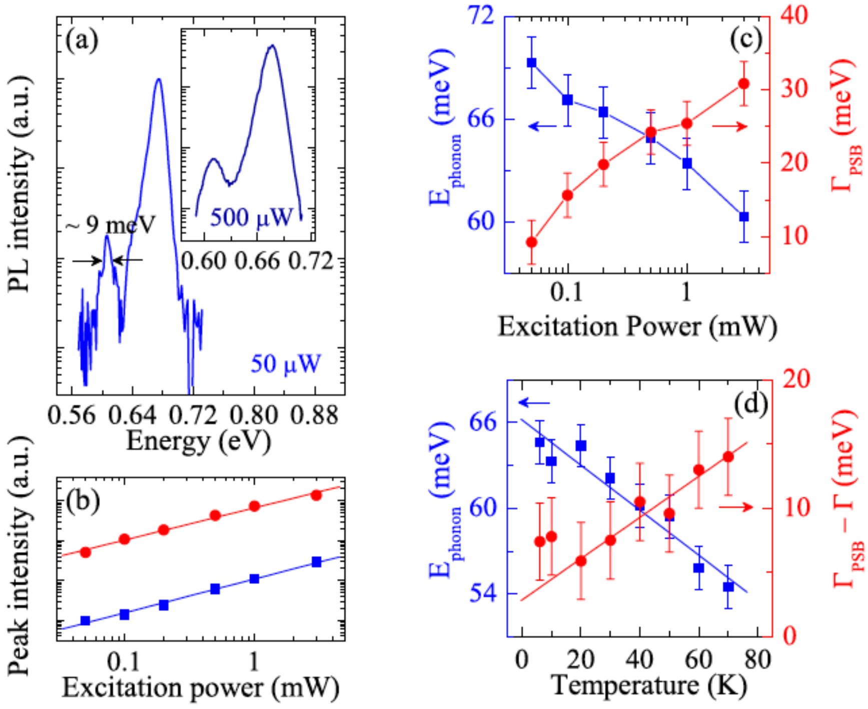

Figure 4-5 PL characteristics of non-doped InN nanowires with lengths ~4μm (beam size ~5μm). (a) The PL spectrum measured at 6 K at an exposure to 50 μW (inset at an exposure to 500 μW). (b) The derived power dependent PL peak intensity for the phonon sideband emission peak (filled blue squares) and the main PL peak (filled red circles). Solid lines are linear fittings. (c) The extracted power-dependent phonon energy (E_{phonon}) and the phonon sideband emission spectral linewidth (Γ_{PSB}), measured at 6 K. (d) The extracted temperature-dependent E_{phonon} and Γ_{PSB}-Γ (where Γ is the spectral linewidth of the main PL peak), measured at an exposure to 500 μW. The blue and red lines in (d) are linear fittings.

Up to here, the possibility of residual acceptor energy level transition(*76, 77*) could be ruled out. This is because: (1) in such a transition, the associated PL peak intensity is quite comparable to that of the main PL peak. Here, however, the low-energy peak is about two decades weaker than the main PL peak, which indicates a second-order effect (e.g., phonon related process). (2) If the presented low-energy peak is due to the residual acceptor energy level transition, then at low excitation conditions such transition should dominate the PL spectra. It is, however, not the case again. Here, the low-energy peak is *always* about two decades weaker than the main PL peak.

Moreover, it should also be noted that the contributions from valence band tails and excitons can be excluded because the energies involved in these processes are comparably small (~30 meV for localized valence band tail states(*77*) and ~3-9 meV for excitons(*4, 79*)).

We, therefore, ascribe the low-energy peak to the phonon replica of the main PL peak, or the phonon sideband emission (PSB), which is a natural result of the observation of optical phonon modes in micro-Raman spectrum (Figure 4-2) and the extremely low free carrier concentration in such pristine InN nanowires.

The PSB emission linewidth (Γ_{PSB}) and the phonon energy (E_{phonon}) were also derived to give more insight. With increasing the optical excitation power, as shown in Figure 4-5(c), Γ_{PSB} gets much broader and E_{phonon} becomes smaller. A similar trend was also observed in the extracted temperature dependence of Γ_{PSB} (here the plot of $\Gamma_{PSB} - \Gamma$, where Γ is the linewidth of the main PL peak, is shown) and E_{phonon} (Figure 4-5 (d)).

Temperature-dependent PSB properties from LO phonons have been studied before in GaN(*244*) and InN epilayers(*63*), where the energy shift with temperature can be described as,

$$\omega_{PSBm}(T) = m\omega_0 - (\frac{5}{2} - m)k_B T - m\Delta(T). \qquad \text{Eq. (4-2)}$$

where m is the PSB index (here, $m = 1$[27]), ω_0 represents the PSB energy at $T = 0$, and the third term is from the anharmonic shift due to phonon decay, which is negligible here.(*63*) The linear fit of the temperature dependent E_{phonon}, see the

---

[27] Due to the cut-off wavelength of the detector, we can only observe the first PSB band; hence m=1.

blue line in Figure 4-5(d), gives a slope of (−0.158 ± 0.024) meV K^{-1}, which is consistent with the calculated temperature coefficient if taking $m = 1$ in Eq. (4-2).

Similarly, the temperature evolution of Γ_{PSB} can be described as,

$$\Gamma_{PSBm}(T) = 2\sqrt{(\frac{5}{2} - m)k_B T} + \Gamma(T) + \Gamma_{phonon}(T). \qquad \text{Eq. (4-3)}$$

where $\Gamma(T)$ is the temperature-dependent broadening of the interband emission peak due to the electron-phonon interaction, and $\Gamma_{phonon}(T)$ is the negligible temperature-dependent phonon broadening.(*63*) The plot of ($\Gamma_{PSB}(T) - \Gamma(T)$) versus T is shown in Figure 4-5(d), and the red line is a linear fit, which gives a slope of (0.160±0.022) meV K^{-1}. This number is also consistent with the calculated temperature coefficient if taking $m = 1$ in Eq. (4-3).

Phonon mode analysis and indication – The derived E_{phonon} at 5 K under 50 μW is ~70 meV, or ~564 cm^{-1} in wavenumber, which is very close to three optical phonon modes, i.e., A_1(LO) mode, E_1(LO) mode, and the L^+ mode. The L^+ mode, being the most debatable mode due to its proximity to the uncoupled LO mode, was proposed either coming from interface depletion layers(*245*) or wave vector nonconservation during scattering(*95, 216*). The idea of depletion layers was excluded by the recent IR ellipsometry measurements.(*215*) Meanwhile, the wave vector nonconservation requires significant crystalline disorder, which therefore cannot explain the situation where the samples are mostly defect-free such as intrinsic InN nanowires in this study. Therefore, to the current knowledge, L^+ mode is not likely happening here.

This phonon mode analysis suggests the phonon sideband emission in the presented study could only involve pure phonon mode(s), which further indicates that such non-doped InN nanowires exhibit a negligible level of electron accumulation on the lateral surfaces, and are consistent with the nature of intrinsic InN nanowires.

In summary, intrinsic InN nanowires are achieved for the first time, with the near-surface Fermi-level being located below the CBM. This study provided unambiguous evidence showing that the commonly measured large free carrier concentration, surface electron accumulation, and E_F pinning are *not* fundamental properties of InN. It reconciles, to a large extent, the intense debate on the origin of the 2DEG on the InN non-polar surfaces. In addition, such intrinsic InN nanowires possess distinct PL properties compared with those measured in tapered InN nanowires grown by conventional methods.

5. Demonstration of intrinsic InN nanowires (II): The electrical transport properties

In the previous chapter, intrinsic InN nanowires with the absence of surface electron accumulation and extremely low free carrier concentration (on the order of 10^{15} cm^{-3}, or less) have been demonstrated. There is, therefore, an urgent need to develop a fundamental understanding of the charge carrier transport properties and their dependence on the nanowire dimension in such intrinsic InN nanowires. Additionally, a detailed quantization of the characteristics of charge traps, if there are any, in such intrinsic InN nanowires is of crucial importance to the design of future InN-based high-speed devices and systems in the nanoscale.

In this chapter, the electrical transport properties of intrinsic InN nanowires are characterized by the nanoprobing technique. It was measured that the electrical transport is dominated by ohmic conduction at low bias and SCL conduction at high bias, with a crossover voltage V_c at ~0.2 V. It was further derived that, for InN nanowires with relatively large radii, the free carrier concentration can be on the order of 10^{13} cm^{-3}, which agrees very well with the intrinsic carrier concentration (n_i, on the order of 10^{13} cm^{-3}) level in InN if taking $m_e^* = 0.05m_0$ and $m_h^* = 0.65m_0$.(*111, 234, 235*) Meanwhile, for such large-radius InN nanowires, the electron mobility can be in the range of 8,000 to 12,000 cm^2/V·s, approaching the theoretically predicted maximum value at room temperature (~12,000 cm^2/V·s). Moreover, the dependence of free carrier concentration and electron mobility on the nanowire dimension can be well correlated with growth parameters and surface charge properties of InN nanowires. In addition, the charge traps are found to distribute exponentially in energy near the CBM, with a characteristic energy of ~65 meV.

5.1. *I-V* characteristics

The electrical transport measurements were performed on such *as-grown* single InN nanowires in an SEM environment, wherein a retrofitted tungsten tip and melted In droplets on the backside of Si substrate serve as the top and bottom electrodes, respectively. Such nanoprobing to an individual InN nanowire is shown in the top-left inset of Figure 5-1(a).

In this study, in order to cover a wide range of nanowire geometry, two batches of non-doped InN nanowires were grown with different growth duration. The resulting nanowire lengths are ~2 μm (with radii in the range of 200 nm to 1000 nm) and ~1 μm (with radii in the range of 80 nm to 800 nm) in batches I and II, respectively. In these growths, only the inner heating zone of a 2-zone heater was used, which can create a temperature distribution across the 2-inch wafer. The nanowire radius was found to decrease with decreasing the substrate temperature.

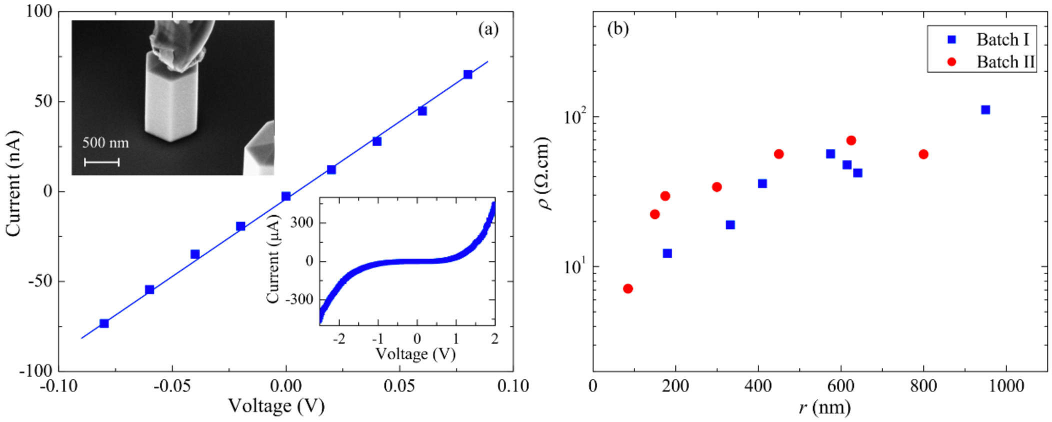

Figure 5-1 (a) Representative low-bias *I-V* characteristics obtained by nanoprobing an individual InN nanowire with length L ~2 μm and radius r ~600 nm. The top-left inset shows an SEM image of such nanoprobing with a tungsten tip. The bottom-right inset shows *I-V* characteristics of the same nanowire at high bias. (b) The nanowire resistivity derived from the linear fit as shown in (a).

The representative *I-V* characteristics of a single InN nanowire under low-bias condition are shown in Figure 5-1(a). The linear characteristics suggest the formation of an ohmic contact.(*228, 230, 246*) With increasing the bias voltage, however, the *I-V* characteristics become highly nonlinear (see the bottom-right inset of Figure 5-1(a)). Such nonlinear *I-V* characteristics at relatively large bias are consistent with SCL conduction.(*231-233, 246, 247*) For the low-bias *I-V* characteristics, if neglecting contact resistance,[28] the nanowire resistance is estimated to be in the range of MΩ. The resistivity ρ of each nanowire can be further derived (as illustrated in Figure 5-1 (b)), which varies in the range of 6 to 100 Ω·cm and exhibits an increasing trend with increasing the nanowire radius.

More features of the high-bias conduction can be revealed in a logarithmic plot. Figure 5-2(a) shows the *I-V* characteristics in a logarithmic scale of two InN nanowires with lengths of ~2 and ~2.4 μm and radii of ~600 and ~900 nm, respectively. It is clearly seen that the *I-V* characteristics change from ohmic conduction at low bias to SCL conduction at high bias, and the crossover voltage (V_c) can be determined by the intersection point of the two fitting lines for the ohmic and SCL conduction regimes. The nanowire radius dependent V_c is shown in Figure 5-2(b), and exhibits a statistical average of 0.20±0.03 V.

The slope β at relatively large bias (defined by $I \propto V^{\beta}$) is plotted in Figure 5-2(c), and exhibits a statistical average of 3.53±0.39. The β values in this range have been commonly measured in various nanowire structures(*231-233, 246, 247*) and can be understood by the SCL conduction with the presence of charge traps that are exponentially distributed in energy, i.e., $e^{-(E-E_C)/kT_c}$, where T_c is the characteristic temperature and kT_c represents the characteristic energy.(*222*) With further increasing the bias, the slope β is reduced to 2 for a bias voltage V_s >1.4 V

---

[28] The presence of surface electron accumulation on top surface (polar/semi-polar plane) of InN nanowires renders low-resistivity ohmic contact with the tungsten tip. At the InN nanowire and Si interface, a very thin SiN_x layer was observed;*(58)* however, due to the heavily *n*-doped Si substrate and low conduction band of InN, electrons can readily tunnel through this thin interface barrier, which can immediately lead to ohmic conduction. In this regard, the contact resistance is much less than the resistance of the InN nanowires. Furthermore, it should be noted that the *I-V* curve at large bias is not perfectly symmetric, which could be due to the asymmetric top and bottom contacts. This has been commonly observed in high-bias *I-V* characteristics with this technique.*(231-233, 246, 247)* Moreover, it is also noticed that occasionally the first few scans may not be symmetric, which could be ascribed to the existence of a very thin oxide layer between the tungsten tip and the investigated InN nanowire. However, such thin oxide layer can be burned away after a few repeated scans, producing nearly symmetric *I-V* curves.

(A line with a slope of 2 is also plotted in Figure 5-2(a)), which indicates the saturation of charge traps.

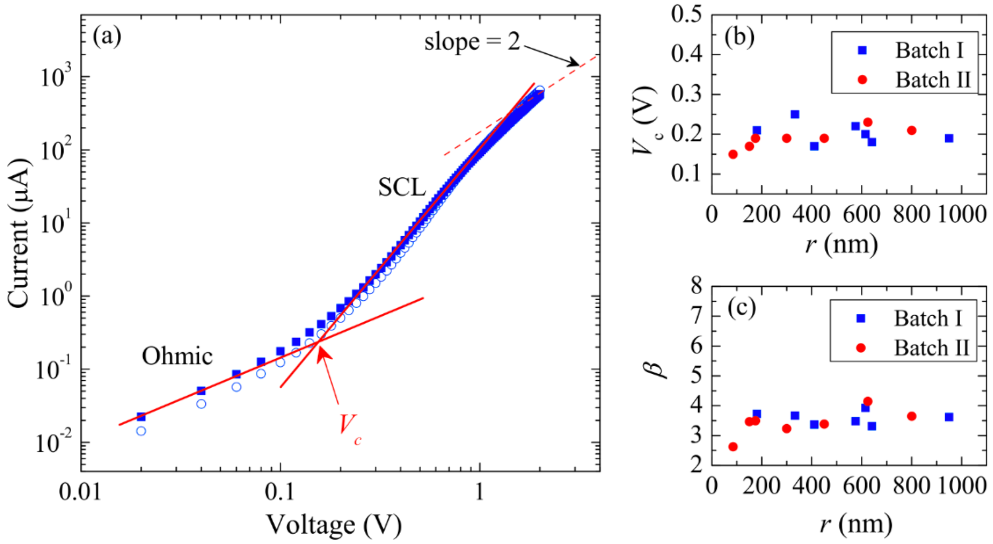

Figure 5-2 (a) I-V characteristics of InN nanowires in a logarithmic plot. Filled squares: length L ~2.0 μm and radius r ~600 nm; open circles: length L ~2.4 μm and radius r ~900 nm. (b) and (c) The derived crossover voltage V_c and the voltage exponential β in the SCL conduction regime as a function of the nanowire radius, respectively.

The observation of SCL conduction at high bias, as well as the filling of charge traps due to the progressive shift of the Fermi-level towards the conduction band edge with increasing the voltage, further suggests low free carrier concentration and the Fermi-level is below the conduction band minimum.

5.2. The electrical transport properties derived using bulk geometry

The theory for SCL conduction in bulk semiconductors has been well established.(*222-224*) In the SCL conduction regime and with the presence of charge traps that are exponentially distributed in energy, the current density can be expressed as:(*222, 228*)

$$J_{SCL}^{bulk} = \varepsilon \square (\theta\mu) \square (\frac{V^2}{L^3}), \qquad \text{Eq. (5-1)}$$

where ε is the dielectric constant, μ is the electron mobility, V is the applied voltage, and L represents the sample thickness (here it is the length of the nanowires). θ denotes the fraction of free charges due to the presence of charge traps, and it depends on the applied bias voltage in the SCL conduction regime according to:(*222*)

$$\theta=\theta_0\left(V/V_c\right)^{\gamma}, \qquad \text{Eq. (5-2)}$$

if the trap density follows an exponential distribution in energy, where θ_0 is a constant and represents the fraction of free charges at the onset of SCL condition, and γ is equal to $T_c/T-1$.(*222*)

Charge trap characteristic energy – Combing Eq. (5-1) and Eq. (5-2) leads to a higher power law dependence on the voltage for the current density, i.e., $J \sim V^{2+\gamma}$, as observed in this experiment ($\beta=2+\gamma$), with $\gamma = 1.53 \pm 0.39$. Therefore, the characteristic energy kT_c for charge traps can be estimated by $kT\square(\gamma+1)$. At 300 K, it is ~65 meV. *This characteristic energy is geometry independent, i.e., it should exhibit similar values for the same quality materials no matter they are in the form of thin film or nanowire.*

Charge trap density – The charge trap density can be crudely estimated by using bulk geometry due to the lack of accurate solution for nanowire structures. This is also the current approach that is normally used to derive charge trap density in nanowires.(*224, 246*) In this case, the charge trap density can be estimated by $V_s = en_tL^2/2\varepsilon$, where V_s is the charge trap saturation voltage, e is the electrical charge, n_t is the charge trap density, L is the nanowire length, ε is the relative dielectric constant. For a saturation voltage of 1.4 V, the charge trap density is estimated to be on the order of 10^{14} cm^{-3}. Contributions to charge traps in InN nanowires may include surface states due to ionic bonding(*248*) and nitrogen vacancies(*249*).

Free carrier concentration and electron mobility – Using the bulk geometry obviously renders that free carrier concentration is independent of the nanowire radius, which is in direct contrast to the experimental observation that nanowires with smaller radii generally exhibit higher free carrier concentration.(*62, 229, 232*) This indicates that bulk geometry *cannot* be used to derive free carrier concentration and electron mobility for semiconductor nanowires. However, for InN nanowires with large radii, bulk geometry approach gives a free carrier concentration of ~6×10^{12} cm^{-3} and an electron mobility of ~15,000 $cm^2/V\cdot s$. These values agree reasonably well with the estimation using nanowire geometry as will be discussed later on.

5.3. The electrical transport properties derived considering the large aspect ratio of nanowires

5.3.1. The formulae

In nanowire structures with large aspect ratio (L/r), the SCL conduction current is significantly enhanced due to the drastically reduced Coulomb screening.(*228*) As just discussed, some characteristics cannot be derived using bulk geometry such as free carrier concentration and electron mobility. On the other hand, there has been no theoretical study on the SCL current density in nanowire structures where charge traps are present. In nanowires where charge traps are *absent*, Talin *et al.* suggest that an appropriate geometrical scaling factor, $(r/L)^{-2}$, where r and L denote the nanowire radius and length, respectively, needs to be included in the calculation of the SCL current density in nanowire structures.(*228, 229*)

Combining the fraction of free charges θ and the scaling factor suggested by Talin *et al.*, a proposed formula for the SCL current density in nanowires with exponentially distributed charge traps in energy can be expressed as,

$$J_{SCL}^{NW} = [(\frac{r}{L})^{-2} \cdot (\frac{\varepsilon}{L^3}) \cdot \theta\mu] \cdot V^2 . \qquad \text{Eq. (5-3)}$$

Eq. (5-3) can also be phenomenally understood by combining the aspect ratio factor (a function of r/L) of nanowire structures into the SCL current density of bulk materials where charge traps are present. The scaling factor can be generally written as $(r/L)^{\delta}$. In a previous study in InN nanowires,(*62*) it was indicated that free carrier concentration is a strong function of the nanowire radius, while the dependence on the nanowire length is negligible. This can only be satisfied mathematically when $\delta = 2$.

The ohmic conduction current, on the other hand, can be written as,

$$J_{Ohmic} = n_0 e \mu \cdot (\frac{V}{L}). \qquad \text{Eq. (5-4)}$$

At the crossover voltage, $J_{SCL}^{NW} = J_{Ohmic}$. Therefore, the free carrier concentration n_0 can be obtained,[29]

$$n_0 = \theta_0 (1/V_c)^{\gamma} \cdot (\frac{\varepsilon}{er^2}) \cdot V_c^{\gamma+1}. \qquad \text{Eq. (5-5)}$$

Subsequently, the electron mobility μ can be derived through the resistivity obtained in the ohmic conduction regime,

$$\mu = \frac{1}{\rho n_0 e}. \qquad \text{Eq. (5-6)}$$

5.3.2. Free carrier concentration and electron mobility: Revised by considering the large aspect ratio of nanowires

Illustrated in Figure 5-3, it is seen that free carrier concentration varies from 10^{13} to 10^{15} cm^{-3}, depending on the nanowire radius, which is in excellent agreement with the PL analysis as discussed in the previous chapter. It also correlates well with the XPS studies, showing that the Fermi-level is located well below the conduction band edge for such non-doped InN nanowires.

In this derivation, the carrier distribution is assumed to be uniform across the nanowire radial direction, due to the absence of surface electron accumulation,[30] which is in contrast to *n*-type degenerate InN nanowires where high density of electrons are accumulated on nanowire surface.(*127*)

---

[29] It is expected that, at or near the saturation voltage V_s, θ should approach unity. Therefore, in Eq. (5-5), the prefactor $\theta_0 (1/V_c)^{\gamma}$ is proportional to $(1/V_s)^{\gamma}$. For V_s = 1.4 V, $(1/V_s)^{\gamma}$= 3/5 V^{-1}. In this work only a few nanowires show saturation voltages that are around 1.4 V, the rest nanowires do not exhibit any saturation up to 2 V. The rest of the calculation in this chapter is based on $(1/V_s)^{\gamma}$= 3/5 V^{-1}. Therefore, the upper boundary of free carrier concentration and the lower boundary of electron mobility are estimated.

[30] As we will see later on, the presented nanowire surface tends to be weakly *n*-type, i.e., there are more electrons in the near-surface region compared with the bulk due to the fact that defects are preferentially incorporated into the near-surface region. *This weakly n-type surface, however, does not necessarily mean the presence of surface electron*

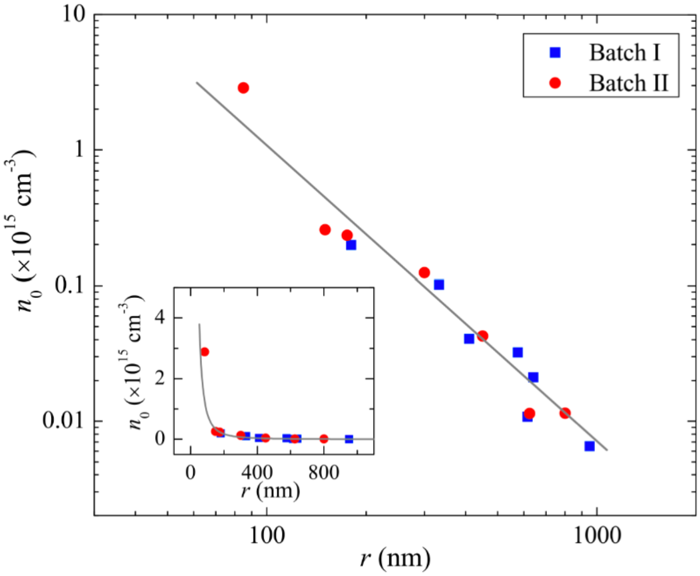

Figure 5-3 The derived free electron concentration n_0 as a function of the nanowire radius r in a logarithmic plot. The line is a linear fit, giving a slope $k = -2.3 \pm 0.2$. The inset shows the same plot but in a linear scale.

Shown in Figure 5-3, the derived free carrier concentration increases significantly with decreasing the nanowire radius according to $n_0 \propto r^{-2.3\pm0.2}$, which can be largely explained by the presence of surface states and defects that contribute to free carriers in such non-doped InN nanowires.

Additionally, to a large extent, small radii nanowires in this work are obtained with the use of a relatively low substrate temperature, which can further increase surface defects and/or impurity incorporation, thereby leading to the enhanced free carrier concentration. This observation is consistent with the studies on the surface charge properties of InN nanowires, which indicates that the presence of surface states and/or defects is the primary source for large free carrier concentration and the surface electron accumulation of n-type degenerate InN nanowires grown by conventional methods.(*62*)

---

accumulation. In the case where the nanowire surface is weakly n-type, one can still approximately assume a uniform carrier distribution over the nanowire radial direction.

Similar $n_0 \propto r^{-2}$ dependence is also observed in InAs nanowires, where the surface electron accumulation is present.(*232*) In contrast, for GaN nanowires, where the surface electron depletion is present, $n_0 \propto r^{-1}$ is observed.(*229*)

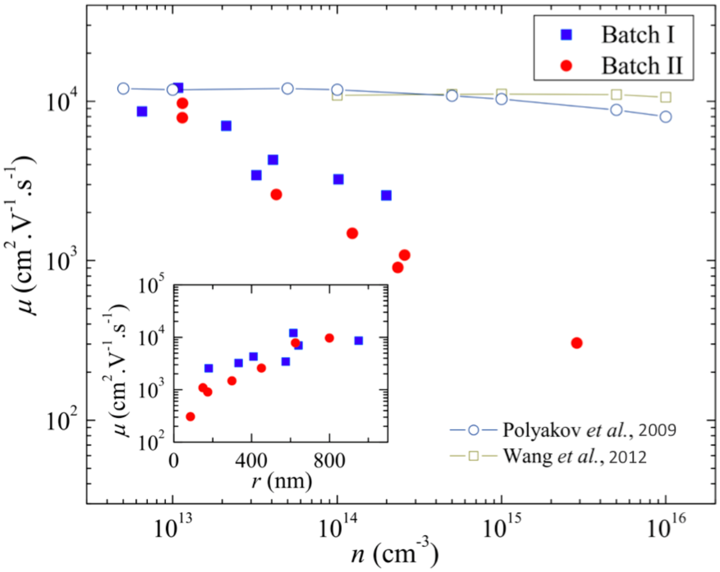

Figure 5-4 The derived electron mobility μ as a function of the free carrier concentration n_0 in a logarithmic plot; the open symbols are from theoretical calculation based on InN *planar structures*.(*64, 66*) The inset shows the derived electron mobility μ as a function of the nanowire radius r.

The derived electron mobility as a function of the free carrier concentration is shown in Figure 5-4. Also shown in this figure is the theoretically calculated electron mobility of InN films with free carrier concentration in the range of 10^{13} to 10^{16} cm^{-3}, which exhibits a nearly constant value of ~12,000 cm^2/V·s (shown as the open symbols).(*64, 66*) It is seen that the experimentally derived electron mobility is in reasonably good agreement with the theoretical calculation for free carrier concentration ~1×10^{13} cm^{-3}.

However, the electron mobility of InN nanowires reduces significantly with increasing the free carrier concentration. For free carrier concentration ~3×10^{14} cm^{-3}, the electron mobility drops to ~1,000 cm^2/V·s, or smaller. This value is more than 10 times smaller, compared to the theoretical calculation in this free carrier concentration range. Clearly, such reduced electron mobility cannot be simply explained by the enhanced impurity and/or defect incorporation. Considering that the relatively large free carrier concentration is derived from the nanowires with smaller radii (shown in Figure 5-3), it is therefore suggested that the electron mobility is largely limited by the enhanced charge and impurity scattering on nanowire surface. In addition, another important point that is usually overlooked is the electrostatic effect so that electrons tend to be repelled by each other to the near surface region; this will naturally enhance the electron surface scattering process.

Such electron mobility reduction by the enhanced surface scattering can also be confirmed by the variation of the electron mobility as a function of the nanowire radius. As illustrated in the inset of Figure 5-4, it can be seen that for the InN nanowires with relatively large radii, the electron mobility does not exhibit significant variation and is in the range of 8,000 to 12,000 $cm^2/V\cdot s$. However, for the InN nanowires with relatively small radii, the electron mobility decreases significantly. This is a clearly effect about the increased influence from surface scattering due to the increased surface-to-bulk volume ratio for small radii nanowires. The strong dependence of electron mobility on the nanowire radius has also been observed in other nanowires, such as InAs nanowires(*232, 250*) and GaN nanowires(*226, 229*).

In summary, the electrical transport properties of intrinsic InN nanowires were studied using the electrical nanoprobing technique. It was measured that free carrier concentration can be on the order of 10^{13} cm^{-3}, which is nearly 4 to 5 orders of magnitude lower, compared to the commonly measured values in InN thin films and tapered InN nanowires grown by conventional methods. The electron mobility in such intrinsic InN nanowires can approach the theoretically predicted maximum value at room temperature. The dependence of charge carrier transport properties on the nanowire dimension and the charge trap characteristics were analyzed, which underscores the predominant role of surface scattering on the electrical transport properties of such intrinsic InN nanowires.

6. Tuning the surface charge properties of InN nanowires

The achievement of intrinsic InN nanowires makes it possible for one to precisely tune the surface charge properties and the optical emission characteristics, over a wide range of doping concentration from intrinsic to *n*-type degenerate. In this chapter, it is clearly demonstrated that the surface electron accumulation, as well as the PL emission characteristics can be well controlled. Moreover, through *ab*-initio calculation, the definitive role of surface doping in tuning the surface charge properties has been unambiguously identified. This unprecedented tunability, which had *yet* been achieved in any nanowire and film structure, is crucial for many emerging nanoscale electronic and photonic devices.

6.1. The presence of surface electron accumulation due to Si doping

This tuning of surface charge properties is first demonstrated by XPS experiments on Si-doped InN nanowires. We investigated the surface charge properties of non-tapered Si-doped InN nanowires grown at a Si cell temperature of ~1250 °C (an estimated average doping concentration of ~5×10^{17} cm^{-3}, based on the secondary ion mass spectroscopy measurements on GaN films grown with similar growth rate and with this Si cell temperature).

For such Si-doped InN nanowires it was observed that the near-surface E_F lies ~0.95 eV above the VBM, shown in Figure 6-1(a). Therefore, given a bandgap energy of ~0.65 eV at room temperature, the near-surface E_F of Si-doped InN nanowires is located ~0.3 eV above the CBM. This indicates the presence of a high-density 2DEG (> 6×10^{12} cm^{-2}), which is significantly larger than the bulk doping concentration. This observation is similar to the commonly reported 2DEG that forms at the surfaces of unintentionally *n*-type doped InN nanowires and thin films. Here, however, it is obtained by the controlled Si doping.

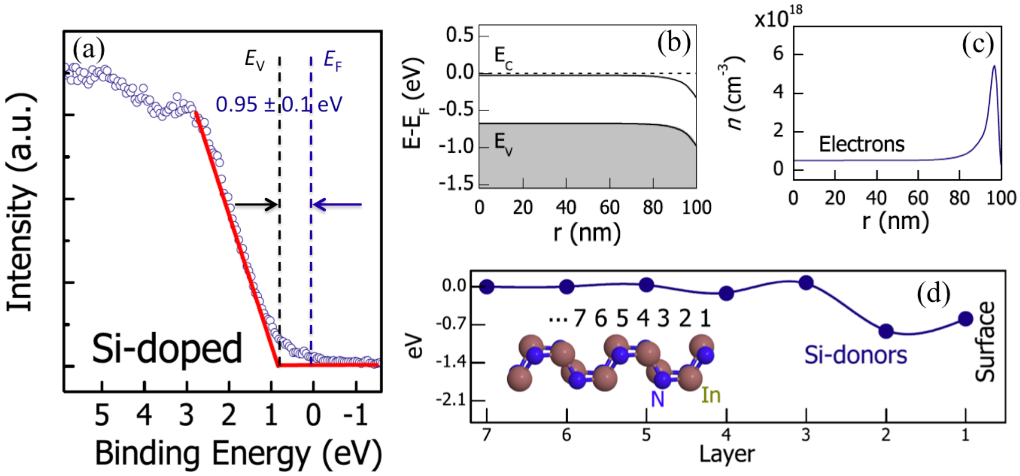

Figure 6-1 Angle-resolved XPS spectra and *ab*-initio calculation of Si-doped InN nanowires. (a) Angle-resolved XPS spectra were measured from the lateral surfaces (*m*-planes) of [0001]-oriented Si-doped InN nanowires, showing an energy separation of ~0.95 eV between the VBM and the near-surface E_F. The surface band structure and electron distribution are modelled by performing self-consistent effective mass calculation on a 200 nm diameter InN nanowire. The Si-doped InN nanowires show ~0.3 eV surface band bending (shown in (b)) and 2DEG formation (shown in (c)), due to a surface donor density of 6.7×10^{12} cm^{-2} in the first two atomic layers. (d) An *ab*-initio calculation showing that the formation energy of In-substitutional Si doping near the InN *m*-plane surface is significantly lower than that in the bulk.

The high surface electron concentration most likely arises from the segregation of Si-dopants at the *m*-plane. This phenomenon is demonstrated through the effective mass calculation presented in Figure 6-1(b) and Figure 6-1(c). Upon raising the bulk doping to $\sim5\times10^{17}$ cm^{-3} (which lies in the range of the average doping concentration obtained at a Si cell temperature of ~1250 °C), a surface 2DEG, having a concentration of $\sim6.7\times10^{12}$ cm^{-2}, occurs to screen the segregated surface donors, resulting in a surface band bending of ~0.3 eV; this correlates rather well with the XPS result in Figure 6-1(a).

This dopant segregation model is strongly supported by atomistic *ab*-initio calculation, where the density functional theory (DFT) calculation on a 3×3 InN slab (12 atomic layers, and 16.2 Å thick) was performed within VASP.(*251*) At this thickness the slab work function converged to the bulk value. A plane-wave basis at a cut-off energy of 450 eV was employed. Pseudopotential and nonlinear core correction were applied within the local spin density approximation (LSDA). Computation was performed on a 3×2×1 *k*-point grid within a $15.2\times17.0\times31.2$ Å^3 super-cell. The force on all atoms was converged to 0.01 eV/Ang.

As shown in Figure 6-1(d), it can be seen that the formation energy of In-substitutional Si doping is much lower at the InN *m*-plane surface − specifically within the first 0.5 nm. Consequently, Si-dopants are preferentially incorporated in the near-surface region. Similar surface dopant segregation has been widely observed in other nanowires.(*169, 252-256*). We attribute this to the reduced lattice strain imposed by the surface donors with respect to the bulk donors.

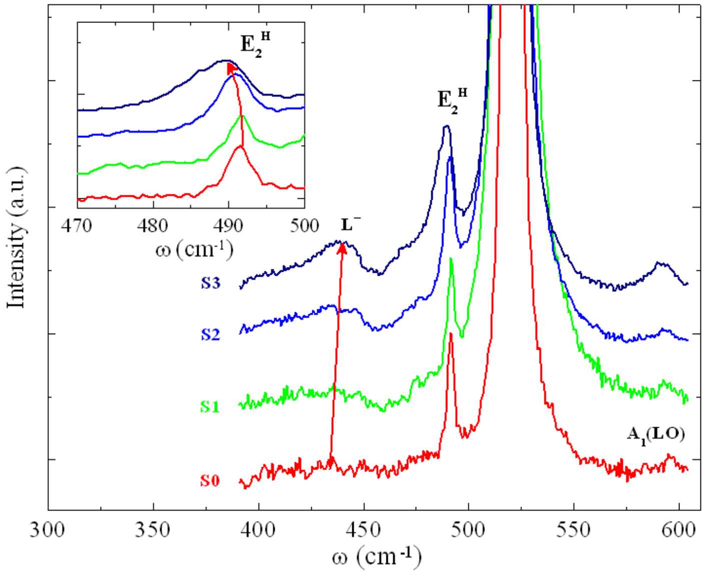

Figure 6-2 Micro-Raman spectra of InN nanowires with different electron concentration. S_0 is non-doped sample; from S_1 to S_3 are *n*-type samples with increased doping concentration.

Such tuning of the surface charge properties, as well as the resultant change in free carrier concentration can be further evidenced by micro-Raman scattering experiments. As can be seen from Figure 6-2, as *n*-type donors are incorporated, the low-energy branch of longitudinal phonon-plasma coupling mode (L^-) associated Raman shift peak, which is an indication of the presence of surface electron accumulation, appears and shifts to higher wavenumbers. This feature is consistent with the presence of surface electron accumulation as *n*-type donors are incorporated.(*149, 150*) Meanwhile, the main Raman shift peak, E_2^H, shifts to smaller wavenumbers and gets significantly broader (the inset of Figure 6-2 shows the evolution of E_2^H with increasing *n*-type donor concentration), which is also consistent with the increased *n*-type characteristics due to the increased free carrier concentration.(*150*)

6.2. Photoluminescence properties influenced by the presence of surface electron accumulation

With the unveiled PL characteristics of intrinsic InN nanowires (Chapter 4), it is possible to have a better understanding of the PL characteristics of Si-doped InN nanowires. In what follows, we will describe the temperature- and power-dependent PL characteristics of Si-doped InN (InN:Si) nanowires with Si cell temperatures of 1250 °C (defined as "moderately Si-doped") and 1350 °C (defined as "heavily Si-doped"), which correspond to average doping concentration of approximately $\sim 5\times10^{17}$ cm^{-3} and $\sim 5\times10^{18}$ cm^{-3}, respectively.[31]

PL characteristics of moderately Si-doped InN nanowires were first described. As illustrated in Figure 6-3(a), it can be seen that at low temperatures (< 160 K), the PL spectra can be characterized by a single emission peak with a peak energy (E_{PL}^H) ~0.73 eV. This energy is considerably larger than that of intrinsic InN nanowires (E_{PL}^1, shown in Figure 4-4). Such large PL peak energy has been commonly measured for *n*-type degenerate InN nanowires.

When the temperature increases, however, in contrast to *n*-type degenerate InN nanowires, it is observed that a low-energy peak (E_{PL}^L) ~0.65 eV (at 300 K) appears in the PL spectra. The arrow in Figure 6-3(a) shows the trend of E_{PL}^L. At 300 K, the intensity of E_{PL}^L is observably higher than that of E_{PL}^H; this suggests E_{PL}^L is *not* likely a phonon replica (second-order effect) of E_{PL}^H.

---

[31] For moderately Si-doped InN nanowires, secondary ion mass spectroscopy (SIMS) indicates the average Si-doping concentration is $\sim 5\times10^{17}$ cm^{-3}. For a Si cell temperature difference of 100 °C, in general the Si-doping concentration will vary by another factor of ~10.

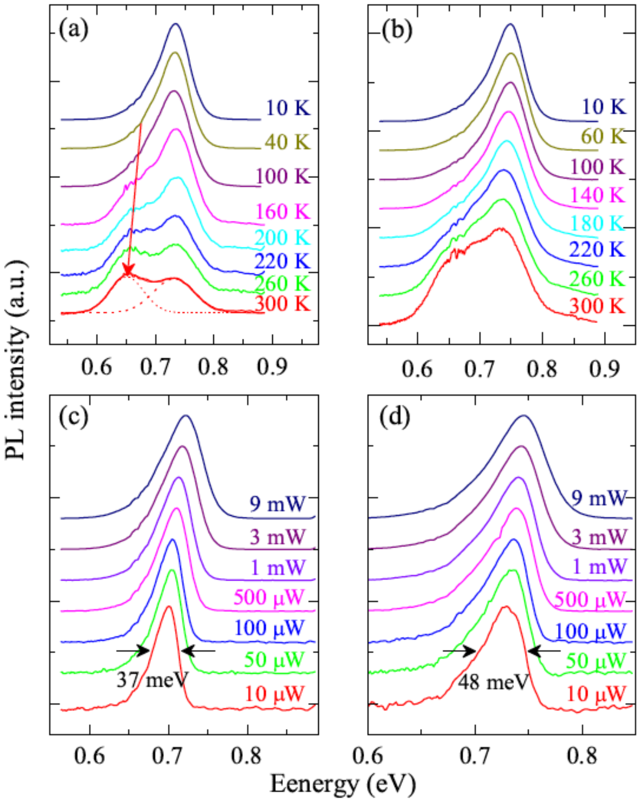

Figure 6-3 PL spectra of InN:Si nanowires with (a) moderately and (b) heavily Si doping at different temperatures under an excitation power of 9 mW, and (c) moderately and (d) heavily Si doping under different optical excitation powers measured at 6 K. The narrowest measured linewidth for each Si-doped sample is labeled by the FWHM value.

The important feature revealed from the temperature dependent PL spectra is that E_{PL}^{L} shows a clear redshift as the temperature increases. In contrast, E_{PL}^{H} is almost temperature invariant, which resembles the profile measured from *n*-type degenerate InN nanowires. Here, we suggest E_{PL}^{L} and E_{PL}^{H} can be ascribed to band-to-band carrier recombination from the low-doped *bulk* region and Mahan exciton emission in the high-doped *near-surface* region. Details will be discussed in Section 6.3.

With further increasing the Si-doping to ~5×10^{18} cm^{-3} (Figure 6-3(b)), the PL spectra exhibit similar feature. However, the high-energy peak described above (E_{PL}^{H}) shifts to an even larger energy (E_{PL}^{3}) ~ 0.75 eV. Such blueshift with increasing doping is consistent with the Burstein-Moss shift. Moreover, the PL spectrum at each temperature is dominated by E_{PL}^{3}, which could suggest the dominant emission region is E_{PL}^{3} associated. We will show in Section 6.3 that this region[32] is the high-doped near-surface region.

From Figure 6-3(a) and Figure 6-3(b), it can be seen that the temperature dependent PL spectra of InN:Si nanowires are significantly different from those of intrinsic InN nanowires (Figure 4-4(a)). Such difference can also be seen from the power dependent PL spectra. Comparing Figure 4-4(d), Figure 6-3(c), and Figure 6-3(d), it can be seen that as Si-dopants are incorporated and with increased average doping concentration, the PL spectral linewidth (Γ, as indicated by arrows) gets much broader under the lowest optical excitation powers when the PL emission can still be picked up (5 μW for non-doped InN nanowires and 10 μW for InN:Si nanowires). Moreover, Γ has much reduced excitation power dependence, e.g., Γ is nearly power-independent in heavily Si-doped InN nanowires (Figure 6-3(d)).

These nearly power-independent PL characteristics of the presented heavily Si-doped InN nanowires have been commonly reported for *n*-type degenerate InN nanowires. Here, we ascribe this to the change of the dominant emission region from the low-doped bulk region to the high-doped near-surface region.

The presence of two emission regions, as well as the evolution of the dominant emission region from the bulk to the near-surface in InN:Si nanowires can be ascribed to the Si-dopants being preferentially incorporated to the near-surface region. Such Si-dopants surface segregation will be discussed in details in Section 6.3.

Up to here, it is important to mention that, the PL peaks of the presented InN:Si nanowires are centered at higher energies compared with those measured from InN films with similar average doping concentration.(*63, 79*) In addition, the PL characteristics in such InN films also exhibit considerable dependence on optical excitation power. This could indicate that the surface of InN nanowires plays an important role in the PL characteristics, due to the large surface-to-bulk

---

[32] As will be discussed in Section 6.3, E_{PL}^{3} and E_{PL}^{H} have the same emission mechanism.

volume ratio. *In this sense, the afore-mentioned two emission regions could only be readily observed in nanowire structures, due to the enhanced surface effect.*

6.3. Discussions

6.3.1. The presence of two emission regions due to the presence of surface electron accumulation

From the afore-described results, it is evident that the PL characteristics of InN nanowires change significantly with Si doping. For intrinsic InN nanowires, as discussed in Section 4.2, the PL emission is mediated by free exciton at low powers, and the PL characteristics can be further characterized by the strong dependence on temperature and optical excitation power.

In contrast, the PL spectra of InN:Si nanowires measured at low temperatures resemble those of *n*-type degenerate InN nanowires, i.e., a peak energy (here, it is ~0.73-0.75 eV) considerably larger than the bandgap of InN, as well as the absence of band-filling effect with increasing the optical excitation power. However, with increasing the temperature, a new feature, the low-energy (E_{PL}^{L} ~ 0.65 eV) peak, emerges in the PL spectra of InN:Si nanowires. In this section, we discuss the origin of this peak, as well as the influence of free carrier concentration and distribution on the PL characteristics of InN nanowires.

As the first step, it is critically important to understand the charge carrier distribution or the Si-dopant distribution in InN nanowires. Although the Si-doping mechanism in InN nanowires remains not clear, the surface segregation of dopant species has been commonly observed in the epitaxial grown III-nitride semiconductors as well as other various semiconductor nanowires.(*169, 252-256*) The Si-dopant surface segregation in InN nanowires was also observed through XPS experiments as well as the effective mass and *ab*-initio calculations (as discussed in Section 6.1).

Based on this, free carrier distribution, and the associated recombination process are schematically shown in Figure 6-4(a) and Figure 6-4(b) for intrinsic and Si-doped InN nanowires, respectively. For intrinsic InN nanowires, photo-generated electron-hole pairs may distribute nearly uniformly across the lateral dimension of the nanowire, and the measured PL emission is mainly due to band-to-band carrier recombination (therefore the shrinkage of bandgap and band-filling effect can be clearly observed).

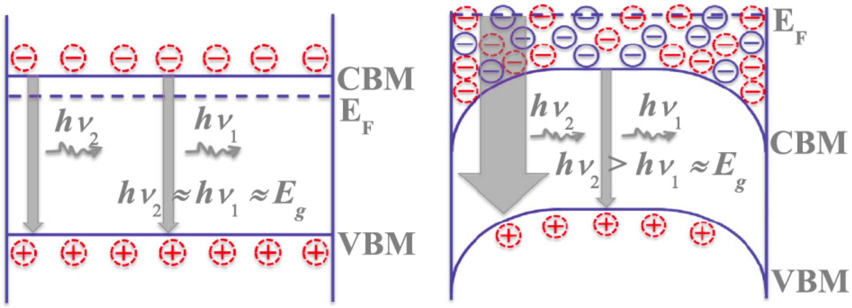

Figure 6-4 (a) and (b) are schematic plots showing free carrier distribution and recombination process in intrinsic and Si-doped InN nanowires, respectively. The blue circles represent intrinsic free carriers, and the dotted red circles represent photo-generated carriers.

For InN:Si nanowires, however, the near-surface region is characterized by the presence of large density of electrons hence severe surface band bending.[33] In addition, due to the lateral electric field induced by inhomogeneous free carrier distribution, photo-generated electrons will migrate to the near-surface region. In this case, two emission regions, i.e., bulk region (low-doped), and near-surface region (high-doped), could probably exist in InN:Si nanowires, with corresponding photon energies marked by $h\nu_1$ and $h\nu_2$, respectively.

Moreover, as Si doping increases, the near-surface region emission could become more important, i.e., the dominant emission region evolves from the low-doped bulk region to the high-doped near-surface region. In what follows, we will examine these scenarios and correlate them with the PL characteristics.

Figure 6-5(a) shows the extracted (by two Gaussian distributions, see the dotted lines in Figure 6-3(a) for a sample fitting) temperature dependent E_{PL}^L and E_{PL}^H of the moderately Si-doped InN nanowires. E_{PL}^I of intrinsic InN nanowires

---

[33] The flat band situation cannot explain the presence of high electron concentration in the near-surface region and low electron concentration in the bulk region.

(Figure 4-4(a)) and E_{PL}^{3} of heavily Si-doped InN nanowires (from Figure 6-3(b)) are also shown in the same plot for comparison.

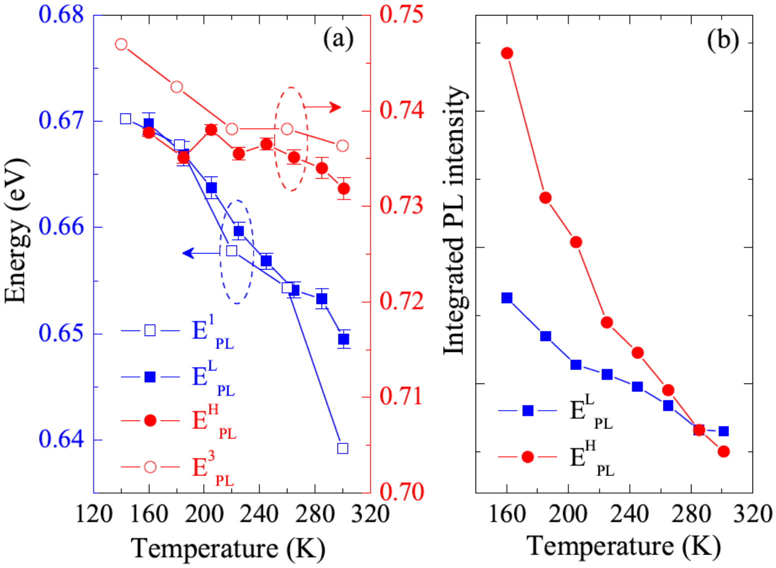

Figure 6-5 (a) The temperature dependence of peak energies: E_{PL}^{L} from the low-doped bulk region (filled blue squares) and E_{PL}^{H} from the high-doped near-surface region (filled red circles) of moderately Si-doped InN nanowires; E_{PL}^{1} of intrinsic InN nanowires (from **Figure 4-4**(a), open blue squares); E_{PL}^{3} of heavily Si-doped InN nanowires (open red circles). (b) The temperature dependent integrated PL intensity for the two emission regions of moderately Si-doped InN nanowires.

It can be seen that the temperature dependent E_{PL}^{L} is remarkably similar to E_{PL}^{1}; therefore E_{PL}^{L} can be ascribed to the carrier recombination process in the relatively low-doped region. The temperature dependent E_{PL}^{H}, on the other hand, exhibits characteristics that are nearly identical to E_{PL}^{3} of heavily Si-doped InN nanowires, as well as those commonly observed in *n*-type degenerate InN nanowires; therefore can be ascribed to the carrier recombination process in the relatively high-doped region.

These results are consistent with InN:Si nanowires being characterized by the presence of a low-doped region and a high-doped region, which corresponds to the bulk and the near-surface region, respectively. This is a natural consequence of inhomogeneous electron distribution caused by the afore-mentioned Si-dopant surface segregation.

More details about the PL characteristics in the low-doped (the bulk) and high-doped (the near-surface) regions can be revealed by the extracted temperature-dependent integrated PL intensity corresponding to each region (area under dotted lines in Figure 6-3(a)). As can be seen from Figure 6-5(b), with increasing the temperature the PL branch from the high-doped region quenches significantly faster than the PL branch from the low-doped region. This fast decay of the PL intensity from the high-doped region can also be observed in Figure 6-3(a), in which as the temperature increases, the PL emission from the low-doped region gradually dominates the spectra.

The fast decay with increasing the temperature in the high-doped region can be largely attributed to the significantly enhanced nonradiative recombination, due to the presence of surface states and defects. This further confirms that the high-doped region locates in the vicinity of nanowire surface.

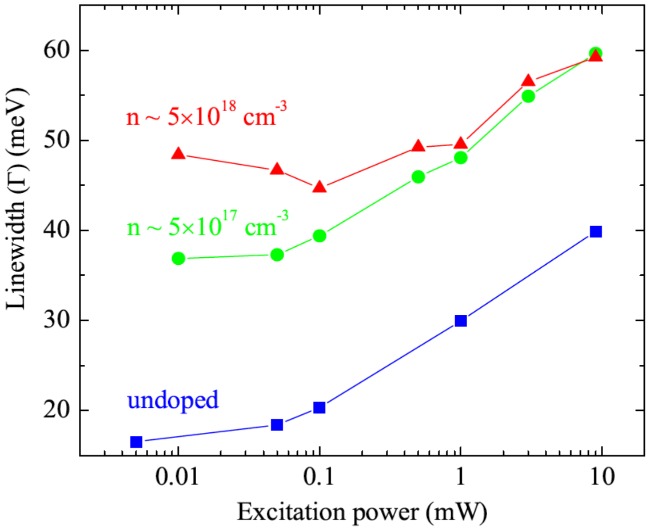

Figure 6-6 The extracted optical excitation power dependence of the PL spectral linewidth (*Γ*) for intrinsic (from **Figure 4-4**(d)) and Si-doped InN nanowires (from **Figure 6-3**(c) and **Figure 6-3**(d)) measured at low temperature.

The afore-described scenarios can also be justified by the distinct PL characteristics of intrinsic and Si-doped InN nanowires measured at low temperatures. Illustrated in Figure 6-6, the power dependent PL spectral linewidth (Γ) was derived from Figure 4-4(d), Figure 6-3(c), and Figure 6-3(d) for intrinsic, moderately Si-doped, and heavily Si-doped InN nanowires, respectively. It can be seen that Γ broadens significantly with increasing Si doping (i.e., at fixed optical excitation power), which is directly related to high free carrier concentration in the near-surface region.

This can be understood within the framework of Mahan exciton emission. Due to the enhanced surface doping, the energy spacing between the E_F and the valence band tail varies along the nanowire radial direction. As a result, electrons with a broad energy distribution are involved in the recombination process, resulting in a very broad PL spectrum; such effect can only be significant in the near-surface region due to the more severe band bending.

This broadening with increasing Si doping essentially indicates that the near-surface region emission gradually dominates the PL spectra. Such effect can also be observed if one compares the PL spectrum of moderately Si-doped InN nanowires measured at 300 K with that of heavily Si-doped InN nanowires (Figure 6-3(a) and Figure 6-3(b)).

Moreover, it can be seen from the heavily Si-doped InN nanowires that the linewidth ($\mathit{\Gamma}$) shows a small, or negligible dependence on the optical excitation power, compared to $\mathit{\Gamma}$ measured from the intrinsic InN nanowires. This can also be explained by that, at this average Si-doping concentration the photo-generated electron concentration might be significantly smaller than the accumulated electron concentration in the near-surface region due to the enhanced surface doping. As a consequence, the PL spectra, in terms of the peak energy position and the spectral linewidth, are largely determined by the residual electron concentration in the near-surface region, instead of the optical excitation power; this is in direct contrast to the case for intrinsic InN nanowires.

In this regard, it is suggested that the broad near-surface region emission predominantly determines the PL characteristics of *n*-type degenerate InN nanowires; thereby leading to very large and temperature independent PL peak energies (considerably larger than the bandgap of InN), as well as very broad and optical excitation power independent PL spectral linewidths. However, the band-to-band carrier recombination in the relatively low-doped nanowire bulk region may also be *clearly* observed, depending on the residual electron concentration. This is the case for the moderately Si-doped InN nanowires in this study.

Compared to the PL characteristics of intrinsic InN nanowires, which can be well explained by the absence, or the presence of a negligible level of surface electron accumulation on the lateral surfaces, the PL characteristics of InN:Si nanowires are fundamentally different, which are the natural results of the presence of electron accumulation on the lateral surfaces.

6.3.2. The influence of surface electron accumulation on the phonon sideband emission

The presence of electron accumulation and band bending on InN surfaces affects the phonon sideband emission significantly. As can be seen from Figure 6-7, the phonon sideband emission peak (estimated peak positions indicated by arrows) disappears gradually with increasing free carrier concentration.

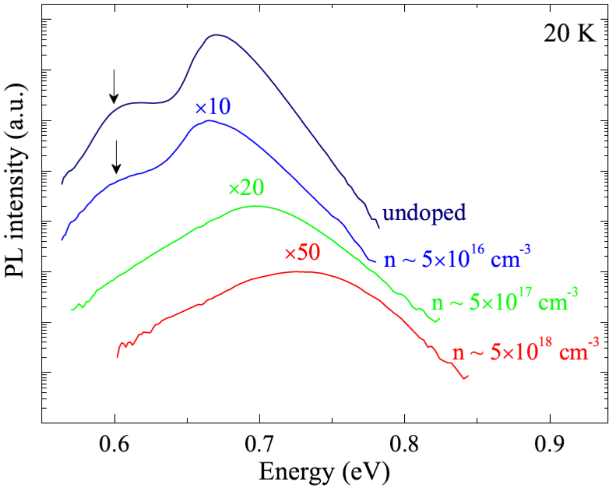

Figure 6-7 The PL spectra of intrinsic and Si-doped InN nanowires measured at 20 K under an excitation power of 1 mW (beam size ~ 50 μm). The PL spectra of InN:Si nanowires were normalized by the PL peak intensity of the main PL peak of intrinsic InN nanowires, and were shifted vertically for display purpose.

A possible reason for this disappearance of the phonon sideband emission peak with Si doping could be the "shadow effect", i.e., the broad main PL peak in

InN:Si nanowires overshadows the phonon sideband emission peak. The other reason could arise from the significantly reduced radiative efficiency (The main PL peak intensity is reduced by a factor of ~ 50 from intrinsic InN nanowires to heavily Si-doped InN nanowires), which is a direct consequence of the presence of surface electron accumulation and band bending. This is because, the photo-generated electron-hole pairs will be more spatially separated due to the lateral electric field caused by the surface electron accumulation; hence the radiative recombination efficiency decreases. In addition, the Si doping induced disorders or defects can be another reason for the reduced radiative recombination efficiency.

6.3.3. Understanding the influence of the nanowire morphology on the surface charge properties

We have further demonstrated, both experimentally and theoretically, that the tuning of the surface charge properties can be achieved by varying the nanowire morphology through controlling the growth parameters. This bridges the presented non-tapered InN nanowires in this thesis work and the tapered InN nanowires as commonly reported.(*126, 146*)

As illustrated in the inset of Figure 6-8(a), the non-doped InN nanowires exhibit tapered morphology when grown at a relatively low substrate temperature (~460 °C). This is compared to the non-tapered near-perfect hexagonal structure achieved at an optimum substrate temperature of ~480 °C (Figure 2-5 (c) and (d)). The near-surface E_F on the lateral, non-polar surfaces of tapered non-doped InN nanowires, measured from the angle-resolved XPS experiments, is shown in Figure 6-8(a). It can be seen that the near-surface E_F is located ~1.0 eV above the VBM. This contrasts directly with the result obtained from the non-tapered and non-non-doped InN nanowires, illustrated in Figure 4-1(a).

The underlying mechanism was investigated. From the atomistic *ab*-initio calculation shown in Figure 6-8(g), we have determined that the formation energy for nitrogen vacancy (as an example of the potential *n*-type defect donors in such tapered nanowires) is lower at the nanowire surface, thereby leading to the enhanced surface doping and surface electron accumulation. Accordingly, the resulting 2DEG formation on the lateral surfaces of InN nanowires can be precisely captured through a self-consistent effective mass calculation (as illustrated in Figure 6-8(b) and Figure 6-8(c)), by incorporating a surface defect donor density of ~6.25×10^{12} cm^{-2}.

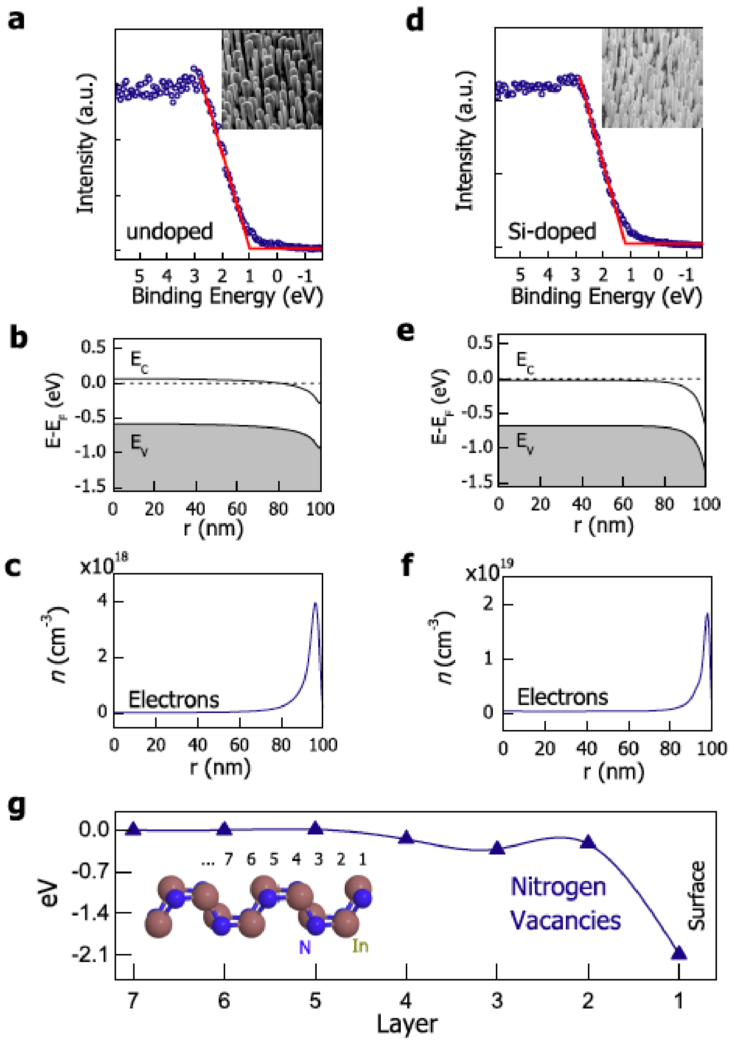

Figure 6-8 XPS and *ab*-initio calculation of InN nanowires with tapered morphology. (a) and (d) XPS spectra measured from the lateral surfaces (*m*-planes) of [0001]-oriented tapered non-doped and Si-doped InN nanowires. It can be seen that the near-surface E_F is located ~ 1 eV and 1.3 eV above the VBM in such tapered non-doped and Si-doped InN nanowires, respectively. The insets are SEM images (2×2 μm^2) of the corresponding nanowires. Self-consistent effective mass calculations of a 200 nm diameter InN nanowire with the segregated surface donors in the first two atomic layers: non-doped InN nanowires with ~0.35 eV surface band

bending (shown in (b)) and surface 2DEG of 6.25×10^{12} cm^{-2} (shown in (c)); Si-doped InN nanowires with ~0.65 eV surface band bending (shown in (e)) and 2DEG of 1.88×10^{13} cm^{-2} (shown in (f)). (g) Nitrogen vacancy formation energy relative to the bulk from *ab*-initio calculation.(*62*)

The variation in the near-surface E_F, depending on the surface morphology and growth conditions, has also been observed in Si-doped InN nanowires. Illustrated in Figure 6-8(d) is the angle-resolved XPS results measured on tapered Si-doped InN nanowires with a Si cell temperature at ~1250 °C (the inset of Figure 6-8(d) shows the SEM image of tapered Si-doped InN nanowires). The near-surface E_F is positioned at ~1.3 eV above the VBM, compared to the ~0.95 eV measured for non-tapered Si-doped InN nanowires with the same average Si-doping concentration (Figure 6-1(a)). Shown in Figure 6-8(e) and Figure 6-8(f), the resulting 2DEG formation at the lateral non-polar surfaces of tapered Si-doped InN nanowires can be precisely captured through the self-consistent effective mass calculation, by incorporating an *additional* surface donor density of ~1.88×10^{13} cm^{-2}.

Such high surface *n*-type doping is the cumulative result of both defect donors and Si dopants (as explained by Figure 6-1(d) and Figure 6-8(g)). The measured near-surface E_F of ~1.3 eV above the VBM (for tapered Si-doped InN nanowires) indicates the presence of a high-density surface 2DEG (~2×10^{13} cm^{-2}). This number is in quantitative agreement with the values commonly measured at the grown surfaces of *n*-type degenerate InN films and nanowires due to the presence of extensive surface defects.

In summary, it is shown, for the first time, that the surface charge properties (such as 2DEG formation), as well as the optical characteristics of semiconductor nanowires can be precisely tuned through the controlled *n*-type doping. The unprecedented tunability of the nanowire surface electrical and optical properties, by designing materials at the atomic scale, promises an entirely new avenue for the development of Si-integrated nanoscale electronic, photonic, and biochemical devices.

7. The realization of *p*-type InN nanowires

In this chapter, it is demonstrated, for the first time, that *p*-type InN nanowires can be realized by direct Mg doping. The presence of Mg-acceptors, *p*-type surface, and *p*-type conduction was clearly measured from the low-temperature PL experiments, XPS experiments, and nanowire field effect transistors, respectively. This progress provides a great promise to extend III-nitride nanophotonic devices into the IR spectrum range.

7.1. Evidence of the presence of Mg-acceptors in InN nanowires

The optical properties of as-grown Mg-doped InN nanowires are studied by the temperature variable micro-PL spectroscopy. Figure 7-1 shows the PL spectra of Mg-doped InN nanowires measured at 7 K under an excitation of 9 mW. The PL spectrum of non-doped InN nanowires, which is measured at 20 K and under the same excitation power, is also shown for a comparison. It can be seen that for non-doped InN nanowires, only a single PL peak appears at ~0.69 eV, which is consistent with the blue-shifted band-to-band PL emission peak due to the band filling effect in high-quality InN epilayers(*63*) and nanowires(*61*).

When the Mg-acceptors are incorporated (low-doped, with a Mg cell temperature of 190 °C), two PL emission peaks can be clearly distinguished with peak energies E_{PL}^{L} ~ 0.61 eV and E_{PL}^{H} ~ 0.67 eV. With increasing Mg doping (moderately-doped, with a Mg cell temperature of 210 °C), only the low-energy PL peak can be observed, which is shifted to E_{PL}^{3} ~ 0.59 eV. For highly Mg-doped InN nanowires (with a Mg cell temperature of 230 °C), PL emission is barely observed.

There are two important features revealed from Figure 7-1. Firstly, as Mg doping increases, the PL peak intensity decreases severely, e.g., compared with non-doped InN nanowires, the moderately Mg-doped InN nanowires exhibit a reduction of the PL peak intensity by ~300 times. This can be ascribed to the enhanced nonradiative recombination process due to the increased doping. Secondly, E_{PL}^{L} is absent in non-doped InN nanowires; we therefore suggest the low-energy PL peak (particularly E_{PL}^{L}, also E_{PL}^{3}) is associated with Mg-acceptors.

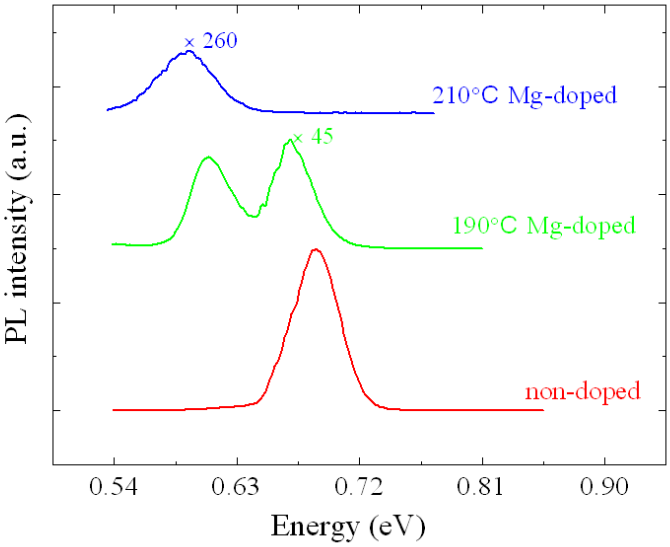

Figure 7-1 The PL spectra of Mg-doped InN nanowires measured at 7 K with an optical excitation of 9 mW. The PL spectrum of non-doped InN nanowires measured at 20 K under the same power is also shown as a comparison. The spectra were normalized by the PL peak intensity of the non-doped InN nanowires, and were vertically shifted for display purpose.

Actually, the energy separation between E_{PL}^{L} and E_{PL}^{H} is about 60 meV, which is consistent with the Mg ionization energy in InN.(*108, 109, 257*) Therefore, the mechanism responsible for E_{PL}^{L} could be the recombination process between electrons in the conduction band and holes at the Mg acceptor energy level.(*76, 77, 108, 109*) It is worth mentioning here that such low-energy PL peak was also observed before in *n*-type degenerate InN nanowires, which is suggested to come from the residual acceptor energy level with *unknown* doping sources.(*76, 77*) Here, the evolution of low-energy PL peaks is clearly controlled by Mg doping, hence is a Mg-acceptor associated effect.

7.1.1. Photoluminescence properties of Mg-doped InN nanowires

The power dependent PL properties of the low-doped sample were first investigated. As shown in Figure 7-2(a), at 0.1 mW excitation, only E_{PL}^{L} can be observed. This can be understood by the effect that under such low excitation power, the concentration of photo-generated electron-hole pairs is so low that most of the electrons recombine with holes at the Mg-acceptor energy level. As the excitation power increases, more electrons and holes are excited into the conduction and valence bands, which can lead to interband emission.

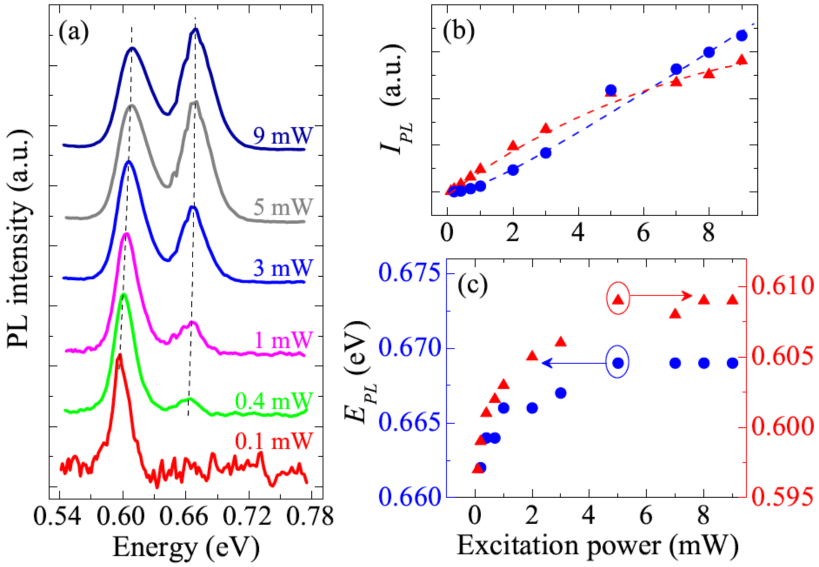

Figure 7-2 The PL properties of the low-doped sample with a Mg cell temperature of 190 °C measured at 7 K. Dashed curves in this figure are guide-for-eye. (a) The excitation power dependent PL spectra. (b) The excitation power dependent integrated PL intensity with $I_{PL}{}^{L}$ in filled red triangles and $I_{PL}{}^{L}$ in filled blue circles. (c) The extracted excitation power dependent PL peak energies with $E_{PL}{}^{L}$ in filled red triangles and $E_{PL}{}^{H}$ in filled blue circles.

More features of these two emission peaks can be revealed by the extracted excitation power dependent integrated PL intensity (I_{PL}). As shown in Figure 7-2 (b), both $I_{PL}{}^{L}$ and $I_{PL}{}^{H}$ increase with increasing the excitation power. However, they have different curvatures: $I_{PL}{}^{L}$ rises faster at low excitations, but exhibits a tendency of saturation at high excitations; while $I_{PL}{}^{H}$ increases slower at low excitations but takes off faster at high excitations, with no saturation trend. This distinct behavior is consistent with the fact that $I_{PL}{}^{L}$ is related to the Mg-acceptor energy level (with relatively low density of states) involved recombination and

$I_{PL}{}^{H}$ is due to band-to-band recombination (involving relatively high of density states in the valence band). Such change in the relative intensity between $I_{PL}{}^{L}$ and $I_{PL}{}^{H}$ is consistent with the redistribution of hole population at the Mg-acceptor energy level and the valence band.(*76*)

The power dependent PL peak energies are plotted in Figure 7-2(c), and both $E_{PL}{}^{L}$ and $E_{PL}{}^{H}$ exhibit a blueshift (~12 meV and ~7 meV, respectively) at low excitations and stay nearly constant at high excitations. It is *not likely* a band-filling effect wherein the peak energies keep shifting to higher energies.(*59, 61*) Similar excitation power dependent PL peak energies have been observed in Mg-doped InN epilayers, and were ascribed to the effects of valence-band Urbach tail.(*108*) Such valence-band Urbach tail effects, though being able to explain the band-to-band recombination, cannot explain the Mg-acceptor related recombination.

Here, we suggest $E_{PL}{}^{L}$ is due to the neutral donor-acceptor pair recombination (D^0A^0) via reaction: $D^0 + A^0 = h\nu + D^+ + A^-$, where $h\nu$ represents the energy of the emitted photon, and can be expressed by, $h\nu = E_g - E_A - E_D + e^2/(4\pi\varepsilon_0\varepsilon R)$, where R is the distance between D^+ and A^-. The last term is energy (E_C) due to Coulomb interaction between D^+ and A^- in the final state. Such interaction gives a reduction of the final state energy (or the emitted photon energy $h\nu$ is increased by E_C). The blueshift, in this case, can be ascribed to the recombination of distant (larger R) donor-acceptor pairs at low excitations and the recombination of nearby (smaller R) donor-acceptor pairs at high excitations.(*258*) The maximum peak energy shift with increasing the excitation power is therefore primarily limited by donor/acceptor concentration giving the same crystal structure and lattice constant.(*258*)

Such D^0A^0 recombination has been commonly observed in GaN thin films,(*258-261*) and the presence of defect donors (concurrently with Mg doping) can be ascribed to the self-compensation effect.(*259*) We propose a similar compensation effect in InN nanowires. Defects such as nitrogen vacancy or oxygen impurity can be introduced by Mg doping in InN, and they normally behave as *n*-type donors due to the extremely low conduction band minimum and high charge neutrality level.(*121*) These *n*-type donors were also found to be stable in Mg-doped InN.(*249*)

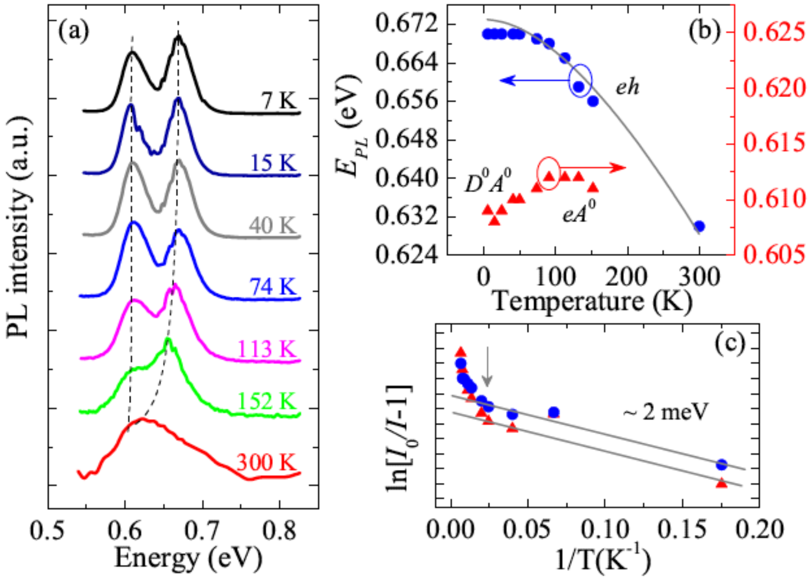

Figure 7-3 The PL properties of low-doped sample with a Mg cell temperature of 190 °C measured under 9 mW excitation. (a) The temperature dependent PL spectra. Dashed curves are guide-for-eye. (b) The extracted temperature dependent PL peak energies with E_{PL}^{L} in filled red triangles and E_{PL}^{H} in filled blue circles. Solid curve is a fit by Varshni's equation. (c) The normalized integrated PL intensities for both PL peaks as a function of the inverse temperature. Solid lines are linear fits.

We further investigate the temperature dependent PL properties of the low-doped sample under 9 mW excitation (see Figure 7-3(a)). Similar to the excitation power dependent PL spectra, the redistribution of hole population at the Mg-acceptor energy level and the valence band can also be observed here. As the temperature decreases, the peak intensity of the low-energy PL peak (I_{PL}^{L}) gets stronger, indicating Mg-acceptor related recombination starts to dominate. However, with further decreasing the temperature (below ~40 K), the Mg-acceptor energy level saturates so that band-to-band recombination dominates (I_{PL}^{H} gets relatively stronger).

The other important feature revealed from Figure 7-3(a) is, as the temperature increases, E_{PL}^{H} shows a clear redshift, which is consistent with the lattice expansion (or the shrinkage of bandgap), further confirming that the PL peak with E_{PL}^{H} is due to band-to-band recombination (*eh*). In this case, Varshni's equation, $E_g(T) = E_g(0) - \alpha T^2 / (\beta + T)$, is expected to be able to describe the temperature dependent E_{PL}^{H}. However, as can be seen from the extracted temperature dependent E_{PL}^{H} (Figure 7-3(b)), the dotted curve (a fit by Varshni's equation with parameters(*61*) of $E_g(0) = 0.673$eV, $\alpha = 0.38$ meV/K, and $\beta = 461$ K) can only describe the temperature dependent E_{PL}^{H} down to ~50 K. For $T < 50$ K, E_{PL}^{H} (=0.670 eV) is invariant with the temperature. This deviation is similar to that observed in InN films,(*262*) and can be ascribed to the recombination involving defect energy levels and/or band-tail states.

E_{PL}^{L}, in contrast, does not exhibit significant temperature dependence (see Figure 7-3(a)). The fact that E_{PL}^{L} is nearly invariant with the temperature is consistent with the characteristics of D^0A^0 recombination.(*259-261*) In addition, the extracted temperature dependent E_{PL}^{L} (Figure 7-3(b)) exhibits a clear, small rising trend above ~40 K. This is consistent with the transformation of D^0A^0 recombination into eA^0 recombination due to the thermal ionization of defect donors with increasing the temperature; and such transformation had also been clearly observed in GaN.(*261*)

The thermal quench of these two PL peaks are also investigated. Illustrated in Figure 7-3(c) is the plot of $\ln[I_0 / I - 1]$ as a function of $1/T$. Here, I_0 denotes I_{PL}^{L} (I_{PL}^{H}) at 0 K, and I represents I_{PL}^{L} (I_{PL}^{H}) at various temperatures. As can be seen, the activation energy (E_t) for the PL emission in the low-temperature regime (e.g., T < 40 K as marked by arrow) is very small ~2 meV, indicating the non-radiative recombination (or the PL quench) for both peaks is related to shallow defect states, which have energies on the order of $2E_t$ with respect to band edges. This is in qualitative agreement with the PL peak energy shift in the transformation from D^0A^0 to eA^0 (Figure 7-3(b)). It should be noted, however, that even though the donor states are shallow, it does not necessarily trigger the

Mott transition if background electron concentration is low. This is in contrast to the Mg-doped InN epilayers with high background electron concentration.(*108*)

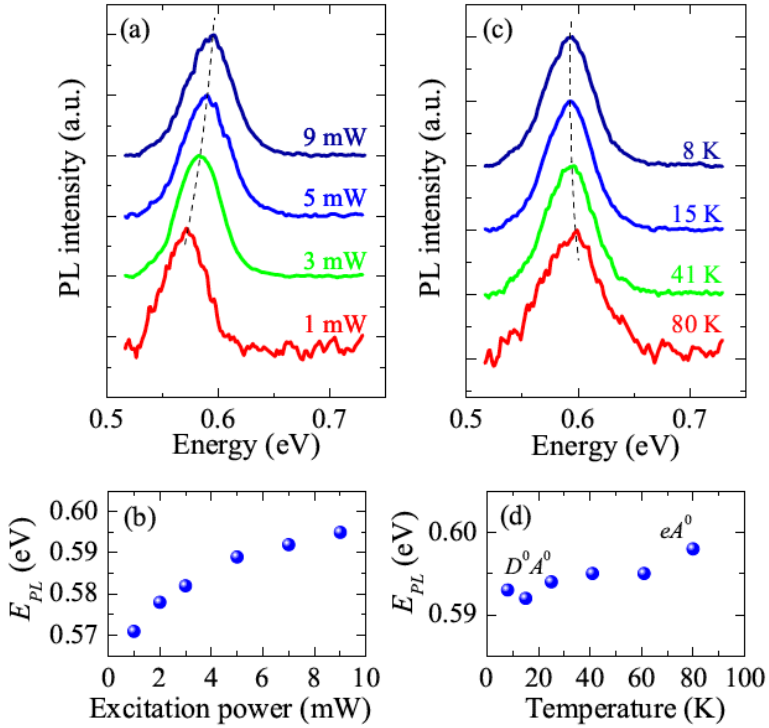

Figure 7-4 The PL properties of the high-doped sample with a Mg cell temperature of 210 °C. Dashed curves are guide-for-eye. (a) The excitation power dependent PL spectra measured at 8 K. (b) The extracted E_{PL}^3 as a function of the excitation power. (c) The temperature dependent PL spectra measured under 9 mW excitation. (d) E_{PL}^3 as a function of the temperature.

In the end, we pay attention to the high-doped sample. Figure 7-4(a) shows the power dependent PL properties; and only a single PL peak, with a peak energy (E_{PL}^3) of ~ 0.595 eV (under 9 mW excitation), appears. The presence of this single PL peak can be ascribed to the much-increased localized hole states at the Mg-acceptor energy level due to the increased Mg doping, so that the photo-generated electrons recombine mostly with holes at the Mg-acceptor energy level. In addition, under 9 mW excitation, E_{PL}^3 exhibits a redshift ~15 meV, compared to E_{PL}^L in the low-doped sample. Such red-shifted PL peak energy could originate from a collective effect of the bandgap narrowing due to the Mg doping induced many-body bandgap renormalization(*263, 264*) and the fact that defect donor states get deeper when Mg doping increases as discussed shortly.

Similar to the low-doped sample, the PL emission for the high-doped sample is suggested to be related to D^0A^0 recombination. The extracted E_{PL}^3 as a function of the excitation power is shown in Figure 7-4(b). The excitation power induced blueshift is ~25 meV in contrast to ~12 meV in the low-doped sample under the same excitation condition. This increased peak energy shift can be ascribed to the increased Mg acceptor concentration and the correspondingly increased donor concentration due to the self-compensation effect.

The temperature dependent PL spectra are shown in Figure 7-4(c), and they are nearly invariant with the temperature. This is similar to the low-doped sample and consistent with the temperature dependent characteristics of D^0A^0 recombination. In addition, the extracted E_{PL}^3 as a function of the temperature resembles that of the low-doped sample, and exhibits a rising trend as the temperature increases (see Figure 7-4(d)). Therefore, it can be ascribed to the transformation of D^0A^0 recombination to eA^0 recombination. The activation energy (E_t) is determined to be ~4 meV (figure not shown here), and this energy is consistent with the PL peak energy shift ($2E_t$) in Figure 7-4(d). The increase in the activation energy could be explained by the increase in the donor concentration due to the increased Mg doping (self-compensation effect), so that some donor states get deeper.

7.2. Evidence of *p*-type surface in Mg-doped InN nanowires

Next, the surface charge properties of Mg-doped InN nanowires are investigated by X-ray photoelectron spectroscopy (XPS). The results are shown in Figure 7-5. In contrast to previous studies of Mg-doped InN thin films where the surface electron accumulation is commonly observed,(*75, 108, 111, 112*) all the Mg-doped InN nanowires here do *not* exhibit any surface electron accumulation (the near-surface Fermi-level locates near or below the CBM). Another very important feature revealed from Figure 7-5 is that *p*-type surface can be observed in Mg-doped InN nanowires with a few doping levels. For instance, the highest Mg-doped InN nanowires (with a Mg cell temperature of 240 °C) exhibit a near-surface Fermi-level ~0.15 eV above the VBM, which is significantly below the intrinsic Fermi-level in InN (~0.38 eV, see Chapter 4). With this near-surface Fermi-level, the free hole concentration on the surface can be estimated to be on the order of 10^{16} cm^{-3}.

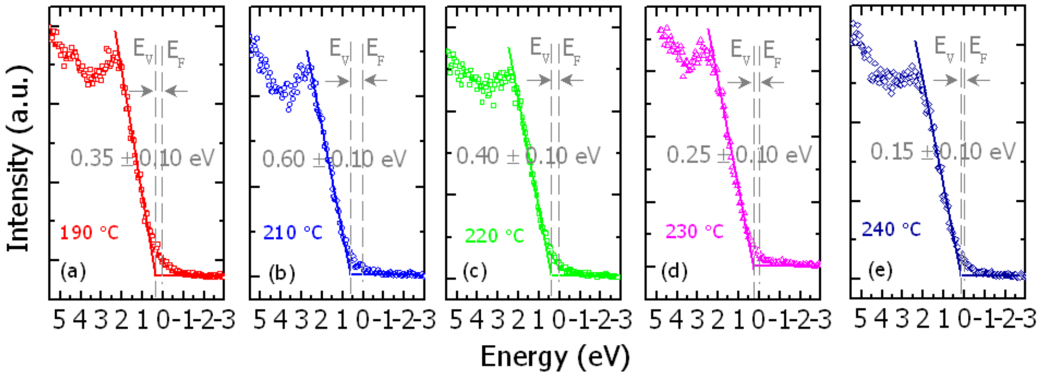

Figure 7-5 X-ray photoelectron spectroscopies of Mg-doped InN nanowires with different Mg doping concentrations. From left (a) to right (e) correspond to Mg cell temperatures of 190 °C, 210 °C, 220 °C, 230 °C, and 240 °C, respectively.

The surface electrical polarity can be then understood by considering the relative population of Mg-acceptors and *n*-type defect donors in the nanowire near-surface region. The migration of Mg-acceptors to surface will lead to a *p*-type surface;(*265, 266*) while the preferential incorporation of *n*-type defect donors such as V_N and O_N to the surface,(*62, 249, 267, 268*) and the possible evaporation of Mg dopants due to the high Mg desorption rate at the growth temperature, will promote a *n*-type surface.

7.3. Direct evidence of *p*-type conduction measured by single nanowire field effect transistor

The presence of free holes or *p*-type conduction can be directly measured by single nanowire field effect transistor. Figure 7-6 shows the study of a Mg-doped InN nanowire field effect transistor with a Mg cell temperature of 220 °C. The schematic plot of the device is shown in the inset.[34] It can be seen that when negative back-gate voltage is applied ($V_G < 0$), the source-drain current (I_{SD}) increases dramatically. When a small positive back-gate voltage ($V_G > 0$) is applied, I_{SD} remains more or less the same. Such *I-V* characteristics have been commonly observed in *p*-type nanowire field effect transistors,(*269-272*) thus strongly indicating the presence of *p*-type conduction in the presented Mg-doped InN nanowires.

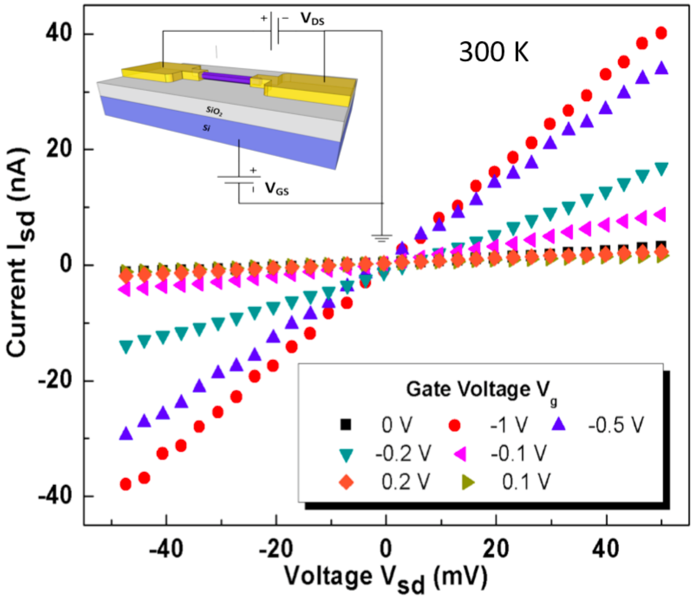

Figure 7-6 The source-drain current as a function of the source-drain voltage for a Mg-doped InN nanowire field effect transistor under a few back-gate voltages. The inset shows the schematic plot of the transistor device.

Furthermore, the I_{SD} - V_G dependence (with source-drain voltage $V_{SD} = 0.05$ V) is plotted in Figure 7-7, which clearly exhibits the increase in I_{SD} for $V_G < 0$. By the I_{SD} - V_G dependence, the free carrier (here it is free hole) mobility can be derived via $\mu = g_m \cdot L^2 / (C_{ox} \cdot V_{SD})$, where $g_m = dI_{SD} / dV_G$ and C_{ox} is the capacitance that can be calculated by $C_{ox} = 2\pi\varepsilon\varepsilon_0 L / \cosh^{-1}[(r + t_{ox}) / r]$ using the

---

[34] 3-point contacts are made to a single Mg-doped InN nanowire, trying to estimate contact resistance; while for the back-gate biasing study, any pair amongst these three contacts can be used.

cylinder-on-plate model.(*270*) For an oxide thickness t_{ox} = 100 nm, nanowire radius r = 100 nm, source-drain distance L = 1 μm, and taking the transconductance g_m estimated by the slope of the linear part in Figure 7-7, the hole mobility is estimated to be ~100 $\mathrm{cm^2/V \cdot s}$. This number is comparable to the reported values in InN thin films.(*110, 235*) With this free hole mobility, the free hole concentration can be calculated to be on the order of 10^{15} $\mathrm{cm^{-3}}$ via $1/(\rho_{total} - \rho_{contact}) = ne\mu$.

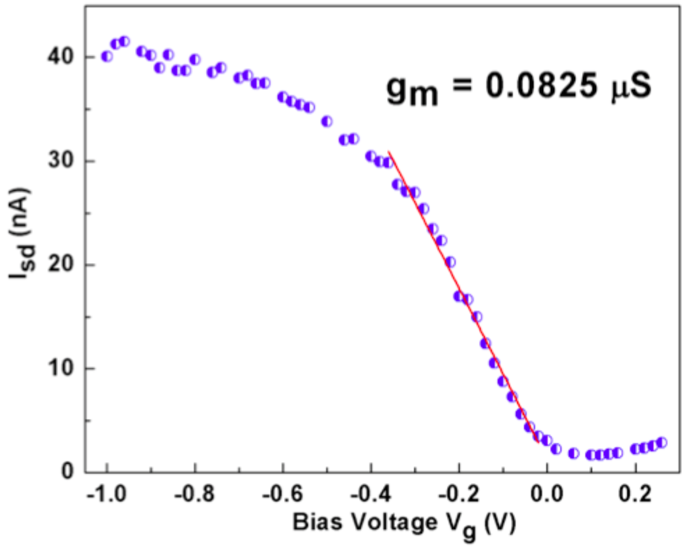

Figure 7-7 The source-drain current as a function of the back-gate voltage with source-drain voltage of 0.05 V.

The other feature shown in Figure 7-7 is the increase of I_{SD} when $V_G > 0.2$ V, which can be related to the appearance of *n*-type inversion layer. With the threshold condition $\phi_s = 2\phi_{Fp}$, where ϕ_s is the surface potential and $\phi_{Fp} = (kT/e) \cdot \ln(p_0/n_i)$, and taking $p_0 = 10^{15}$ $\mathrm{cm^{-3}}$ and $n_i = 10^{13}$ $\mathrm{cm^{-3}}$, we have $\phi_s = 2\phi_{Fp} = 0.24$ V; this value sets the lower limit for the *n*-type inversion layer threshold voltage.

7.3.1. Discussions

With this free hole concentration (on the order of 10^{15} $\mathrm{cm^{-3}}$, under a Mg cell temperature of 220 °C), and taking the valence band effective density of states on the order of 10^{19} cm^{-3} (hole effective mass $m_p^* = 0.65m_0$),(*111, 235*) the Fermi-level in the bulk region with respect to the VBM can be estimated to be ~0.24 eV. Combing the near-surface Fermi-level of ~0.40 eV (Figure 7-5(c)), it indicates a downward band bending about 0.16 eV. Keeping in mind that in InN the intrinsic Fermi-level is ~0.38 eV (see Chapter 4), this indicates that the near-surface region of the Mg-doped InN nanowires with this doping level is neutral while the bulk region is *p*-type. With the use of a higher Mg cell temperature, large free hole concentration and *p*-type surface, as indicated by the XPS spectra (Figure 7-5(d) and (e)), are expected.

In addition, it is noted that, for Mg-doped InN thin films grown with a Mg cell temperature of 220 °C, the Mg dopant concentration is estimated to be on the order of 10^{19} cm^{-3} by secondary ion mass spectroscopy (SIMS) as well as Mg flux measurements and analysis. This number is essentially 4 orders of magnitude higher compared with the estimated free hole concentration (10^{15} cm^{-3}). A few factors could account for the low free hole concentration. Firstly, taking Mg-acceptor ionization energy ~60 meV at 300 K,(*108, 109*) the thermally excited free hole concentration (by Arrhenius process) is estimated to be on the order of 10^{18} cm^{-3}; this sets the upper boundary of free hole concentration at this doping level. Secondly, the free hole concentration will be further reduced by defect donors. As shown in recent studies,(*249, 267, 268*) defects species such as V_N and O_N are predicted to be present in *p*-type materials, which will compensate Mg-acceptors and reduce free hole concentration.(*265, 266*)

Furthermore, a fundamental difference between doping Mg into InN thin films and nanowires is the significantly enhanced Mg evaporation in the former. During the MBE growth, the substrate temperature (450 to 500 °C) is much higher than the Mg cell temperature. This will make Mg adatoms evaporate from the surface. For planar structures, this effect may not be significant since the top surface of planar structures is directly exposed to incoming Mg flux. In this case, even if there is Mg adatom evaporation, it will be immediately compensated by the impinged Mg adatoms, which makes it possible to realize high Mg doping in the near-surface region. The situation is different, however, for nanowire structures. For the growth of Mg-doped InN nanowires, as the growth time increases, due to the shadow effect of the surrounding nanowires, Mg adatoms may not reach the nanowire sidewalls. As a result, the evaporated Mg adatoms (from the sidewalls) cannot be compensated by the impinged Mg adatoms, thereby leading to a significantly reduced Mg dopant incorporation in nanowire structures.

In summary, *p*-type doping in InN nanowires is realized and discussed in this chapter, and this is the first realization of *p*-type conduction in In-containing narrow bandgap semiconductor nanowires by direct doping. The achievement of *p*-type InN nanowires, as well as the revealed surface charge properties paves the way for InN-based nanoelectronic and nanophotonic devices.

8. InN nanowire photodetectors

As elaborated from Chapter 4 to Chapter 7, intrinsic InN nanowires with controlled surface charge properties, as well as *p*-type InN nanowires can be achieved. Some immediate applications include nanowire photodetectors and solar cells by utilizing InN nanowire *p-n* or *p-i-n* diodes, which can function as high-speed photoreceivers for the emerging Si photonics, or as sub-cells of InGaN-based full-solar-spectrum multijunction photovoltaic devices. In this chapter, InN nanowire *p-i-n* photodiodes, which have a light response up to the telecommunication wavelength range, are demonstrated. Such photodiodes can be potential photovoltaic mode photodetectors on Si platform.

8.1. A brief introduction to photodetectors

Nature has provided numerous examples of sophisticated photodetection systems, from the beetle's pit organ that can react to wavelengths of several micrometers, to our eyes in the visible spectrum range. All these natural systems have great features, e.g., small, flexible, power efficient, lightweight, and easy to use, which have always been the guides for us to design high performance photodetection devices. That being said, the research development activities have been intensively focused on minimizing the photodetector size, increasing the responsivity and bandwidth, as well as reducing the operational voltage, response time and the noise level.

The currently employed photodetectors are mostly based on photodiodes, which in general have three operation modes:

a) **Photovoltaic mode.** In this case, there is *no* applied bias. The photocurrent is created by the built-in electrical field of a *p-n* (or *p-i-n*) junction. This is essentially the photovoltaic effect, and the basis for solar cells. *The unbiased operation of photodetectors based on photovoltaic effect offers high sensitivity, low dark current, as well as long-term stability for many dc and low-to-moderate speed* *applications*. However, since there is no applied bias, the electron transient time (which affects the detector speed) is largely determined by the intrinsic electron drift mobility of a material.

b) **Photoconductive mode.** In this case, the photodetector is operated with a reverse bias applied, which drastically increases the response speed at the cost of the increased noise level.

c) **Avalanche mode.** In this case, a much larger bias is required for the operation, so that the *p-n* junction avalanche breakdown occurs, leading to a significantly amplified signal level.

There are also other types of photodetectors as listed in Table 8-1, and the typical values of response time and internal gain of the conventional photodetectors are also listed in Table 8-1.

Table 8-1 Typical values of response time and internal gain of the conventional photodetectors.(*273*)

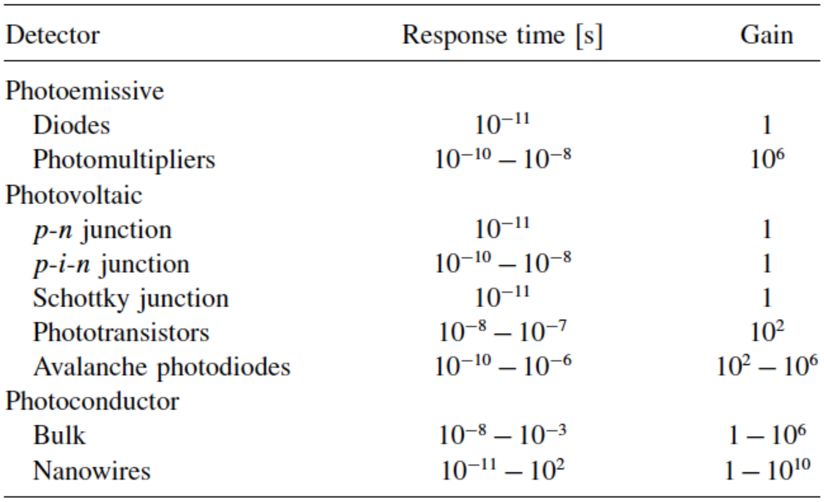

Detector	Response time [s]	Gain
Photoemissive		
Diodes	10^{-11}	1
Photomultipliers	$10^{-10} - 10^{-8}$	10^{6}
Photovoltaic		
p-n junction	10^{-11}	1
p-i-n junction	$10^{-10} - 10^{-8}$	1
Schottky junction	10^{-11}	1
Phototransistors	$10^{-8} - 10^{-7}$	10^{2}
Avalanche photodiodes	$10^{-10} - 10^{-6}$	$10^{2} - 10^{6}$
Photoconductor		
Bulk	$10^{-8} - 10^{-3}$	$1 - 10^{6}$
Nanowires	$10^{-11} - 10^{2}$	$1 - 10^{10}$

8.1.1. Photodetectors for optical communication applications

A very important application of photodetectors is the emerging chip-level optical communication. In this regard, it is of great importance to develop ultrafast photodetectors that can operate at ~1.5 μm wavelength range, as well as can be monolithically integrated on Si in a CMOS-compatible process. The use of Ge for high-speed detectors in the wavelength range from 1.3 to 1.6 μm on Si has been intensively investigated.(*274-278*) Even though the epitaxial-grown Ge on Si has much improved performance compared with Ge crystals,(*278*) the device performance has still been limited, to a large extent, by the relatively large lattice mismatch (~4.2%) between Ge and Si.

Similarly, the photodetectors based on group III-V compound semiconductors on Si, such as InGaAs(*279-281*) and InGaAs/InP(*282*), which operate in the range of 1.3 to 1.6 μm, or GaInAsSb/GaSb, which operate in the range of 1.8 to 2.5 μm,(*279*) face the same lattice mismatch challenge. Admitting group III-V compound semiconductor photodetectors can offer extremely high-efficiency photodetection, in general the performance of electronic and photonic devices based on group III-V compound semiconductors on Si has been severely limited by the generation and propagation of dislocation that is driven by the large difference in lattice constant (4-8%) and thermal expansion coefficient (>250%) between most group III-V compound semiconductors and Si, leading to extremely short lifetime and, ultimately, poor device performance. In this regard, significant efforts have been devoted to integrating group III-V optoelectronics to Si.(*283, 284*)

8.2. Nanowires as new building blocks for the emerging electronic and photonic devices

The dominant role of Si in modern industry requires all the practical devices are amenable for the integration with Si. Such integration was traditionally realized by heterogeneous integration of multiple single crystal semiconductors with different electrical and optical properties onto a single substrate, such as photodetectors based on Ge crystals.(*277*) However, this approach is normally costly and with low-performance due to large interface defects, vacancies, and traps caused by material mismatch. In this regard, the monolithic integration on Si substrate with epitaxy technique has drawn considerable attention.(*284*) By using epitaxial growth technique, the interface defects, vacancies, and traps are significantly reduced so that device performance can be improved. However, the lattice- and thermal- mismatches among different materials become the bottleneck to further improve device performance. New architectures are needed for better device performance.(*273, 285*)

The impact caused by lattice and thermal mismatches, fortunately, can be efficiently reduced in nanowires due to the large surface area, thereby leading to the much improved device performance. Furthermore, the small footprint of nanowires renders themselves as promising candidates for the device-level integration with Si CMOS technology. Moreover, nanowires have many other advantages such as enhanced light absorption and trapping/confinement so that photosensitivity can be enhanced significantly.(*273, 285*) Additionally, nanowire photodetectors offer the possibility to separate optical absorption and carrier transport paths. Driven by these advantages, nanowires and their heterostructures have been widely investigated as optoelectronic components for the emerging nanoscale devices in the past decade, such as nanowire photodetectors, lasers, and solar cells.(*273, 285*)

8.2.1. Basic principles and the current status on nanowire photodetectors

The currently investigated nanowire photodetectors basically can be divided into two major categories. They are:

Nanowire photoconductor – This is the simplest configuration of nanowire photodetectors. As illustrated in Figure 8-1(a), when the light illumination I_0 is applied to a nanowire with a bias V, a change in conductivity will occur via, $\Delta\sigma(t)=\sigma_{light}(t)-\sigma_{dark}(0)=e(\mu_n\Delta n(t)+n\Delta\mu_n(t))$, where the dark condition is set at $t = 0$. This will give a photocurrent density according to $J_{PC}=\Delta\sigma\cdot F$ (where F is the applied electrical field), and photosensing is realized. Nanowires, due to large surface area, normally have excellent photoconductive properties (e.g., light absorption), and therefore, have a great potential for optoelectronic devices.

Nanowire photodiode – Besides the photodetectors based on nanowire photoconductors, other one-dimensional or quasi-one-dimensional structures that consist of semiconductors, metals, and superconductors are also being investigated.(*169*) Additionally, conventional semiconductor *p-n*, or *p-i-n* diodes are being replaced by their nanowire counter-partners; and significant efforts have been devoted to growing nanowire axial junctions, radial junctions, and superlattices.(*286-289*) This has become another important area being investigated intensively for nanowire photodetectors. Such homo- or hetero-junctions are schematically shown in Figure 8-1(b) to (e).

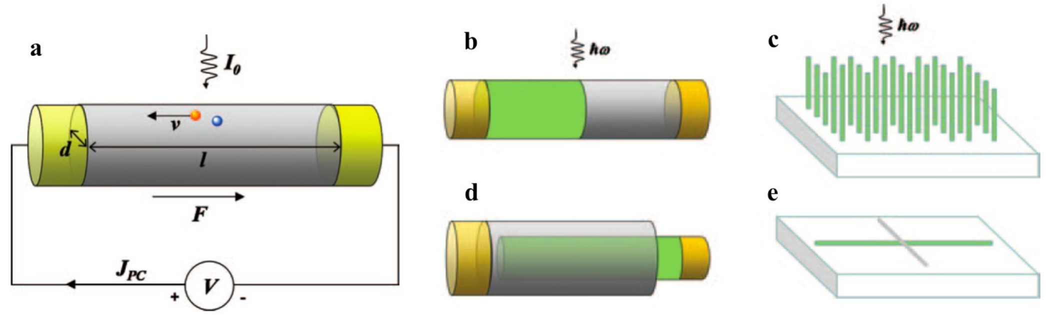

Figure 8-1 (a) Nanowire photoconductor with light illumination (I_0). J_{PC} is the photocurrent density, F is the applied electric field, and v is the electron drift velocity. From (b) to (e): an axial nanowire junction, axial nanowire junction arrays grown on certain substrate, a core/shell or radial nanowire junction, and a crossed nanowire junction by pick/place dispersing.(*273*)

In addition, to realize practical device applications, nanowires have to be integrated to certain substrate. The integration can be technically realized by two common and important approaches: (a) direct growth of semiconductor nanowires on the substrate(*285*) and (b) *pick/place transfer* of nanowires(*196, 285, 287, 288, 290-293*). The advantage of the former approach is the seamless integration with the substrate, while the latter gives a wide range of integration possibility such as integrating onto flexible substrates for the emerging flexible electronic and photonic devices.[35](*196*) The schematic plot for each approach is illustrated in Figure 8-2.

---

[35] This is due to the growth of semiconductor nanowires on flexible substrate is challenging at present.

Top:

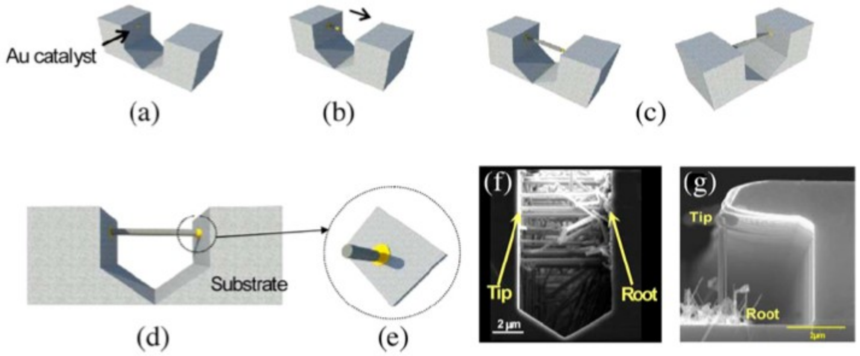

Bottom:

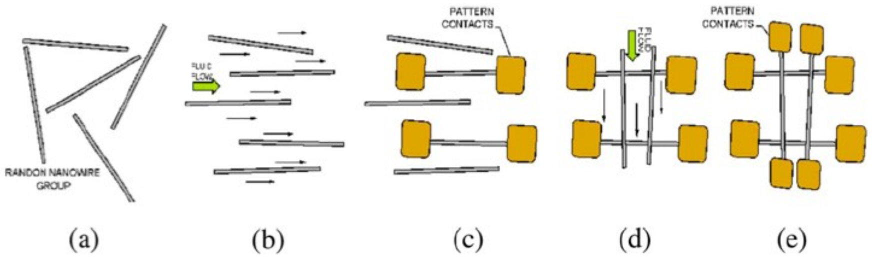

Figure 8-2 Nanowire device integration techniques. Top: (a) to (e) show the integration by direct growth with the bridge growth technique, and (f) and (e) show the SEM images of the bridged nanowires.(*285*) Bottom: (a) to (e) show the nanowire integration to foreign substrates controlled by liquid flow, through which either single nanowire device, or nanowire *p-n* junction device can be fabricated.(*273*)

The current status on nanowire photodetectors – Compared with the mature planar structure photodetectors, such as the commercialized InGaAs, or InSb photodetectors with high responsivity (~1 A/W), the nanowire photodetectors are still at a fundamental research stage. For example, a lot of efforts are still spent on understanding the photocarrier dynamics of Group III-V semiconductor nanowires,(*273*) instead of developing practical Si-integrated photodetectors. Furthermore, the currently investigated nanowire photodetectors typically possess a low responsivity (A/W), and such light response is limited to the UV spectrum range. For example, ZnO-based nanowire photodetectors only exhibit a responsivity of ~0.009 to ~0.07 A/W under UV light illumination.(*273, 285*) Developing nanowire photodetectors that can be integrated to Si CMOS technology, and operate in a longer wavelength, especially in the telecommunication wavelength range is urgent.

8.2.2. InN nanowires as a promising optoelectronic component

Recently, InN-based nanowire heterostructures have emerged as a highly promising candidate for high performance nanophotonic devices on Si.(*58, 59*) By virtue of the effective strain relaxation to the lateral surface, nearly dislocation-free III-nitride nanowire heterostructures can be monolithically grown on Si platform.(*131, 291, 294, 295*) Moreover, InGaN ternary compounds exhibit extraordinary attributes, including the tunable bandgap energy from 0.7 eV to 3.4 eV, extremely large absorption coefficient (~10^5 cm^{-1}) in the visible spectrum range, and very high electron saturation velocity (~10^8 cm/s), that are ideally suited for applications in the chip-level high-speed photoreceivers.(*4*)

The currently employed photodetectors all face the *efficiency-speed trade off*. The absorption coefficient of the active layer in the present photodectors is typically ~10^4 cm^{-1}. Therefore, in order to improve the incident light absorption hence the sensitivity and quantum efficiency, the active layer has to be thicker compared with materials with larger absorption coefficient. In this case, as the cost, the photo-generated electrons will have to travel a longer distance so that the detection speed is lower.

InN, on the other hand, possesses a large absorption coefficient ~10^5 cm^{-1} (in the visible spectrum range), which means compared to materials with lower absorption coefficient, a thin active layer made with InN will absorb more incident light. Furthermore, InN has very large electron drift mobility at room temperature as well as large saturation velocity, which means even for a thick active layer made with InN, the electron transient time is still shorter, compared with the currently employed photodetector materials. In this regard, InN is a very promising material for high-sensitivity, ultrahigh-speed photodetectors.

Meanwhile, to date, the semiconductor nanowires used for photodetector studies are generally grown with the use of metal-catalyst (such as Au). In this case, foreign metal atoms will distort the electrical and optical properties of the semiconductor nanowires, and hence impact device performance. InN nanowires, however, can be grown on Si substrate by catalyst-free process through MBE. More importantly, as demonstrated in Chapter 2, high-quality InN nanowires can be grown on amorphous template, which is a big step to remove the dependence of nanowires on substrate. Additionally, InN nanowires are generally grown at low temperatures, which is compatible with CMOS thermal budget.

In the end, for nanowire device, one of the most important factors that need to be carefully controlled is the surface charge properties, which are normally problematic due to the large surface area of nanowires. However, as discussed from Chapter 4 to Chapter 6, it can be seen that the surface charge properties of InN nanowires are completely controllable. This immediately makes InN nanowires an attractive candidate for a number of electronic and photonic devices. In the rest of this chapter, we demonstrate InN nanowire *p-i-n* photodiode that has a light response up to the telecommunication wavelength range, and such InN nanowire photodiode can be potentially used as a high-speed photovoltaic mode photodetector on Si platform.

8.3. InN nanowire photodiode

8.3.1. The photodiode structure design and fabrication

There are a number of factors considered for the diode structure design. First of all, in order to minimize the influence of surface electron accumulation (e.g., the light and surface accumulated electron could create the plasmonic state so that the light is screened on the surface), and considering the top surface is semi-polar or polar (with the presence of surface electron accumulation), no Si-donors were employed in the design. Secondly, in order to maximize the light absorption, long non-doped region is employed. Therefore, the diode structure is: a *p* region in the bottom followed by a long *i* region in the middle, then a very short *n* region on the top (due to the electron accumulation on the top surface of InN nanowires) in the axial direction, as illustrated in Figure 8-3(a). Thirdly, *p*-type Si substrate (*not n*-type Si substrate) is utilized for the transport and collection of holes through the bottom *p*-type section. Lastly, in terms of the fabrication process, we used polyimide (PI) to protect the nanowire surface (e.g., to avoid contamination), and metal-grid contacts on the top to maximize the light absorption (see the inset of Figure 8-3(b)).

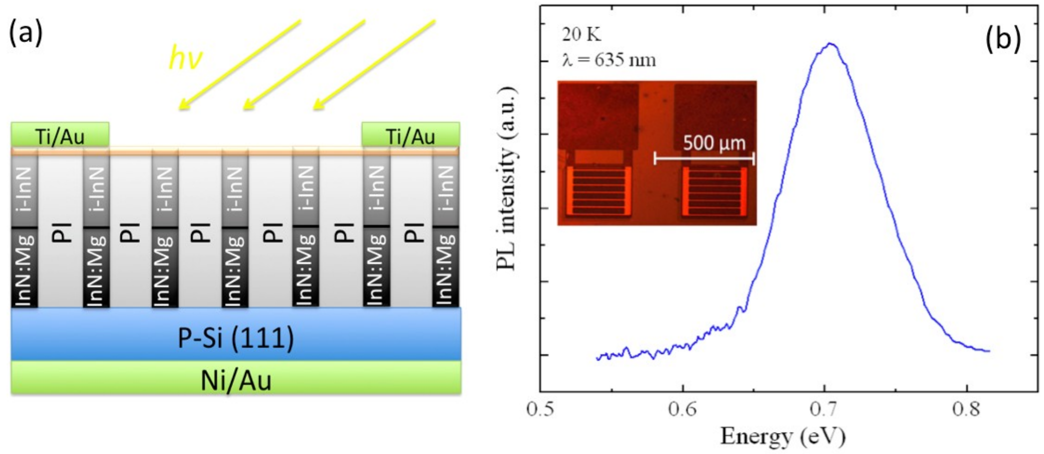

Figure 8-3 (a) A schematic illustration of the InN nanowire photodiode structure. (b) The PL spectrum of the diode measured at 20 K with red laser under 9 mW excitation, and the inset shows the top view of devices with size of 0.3 by 0.3 mm^2.

The detailed structure and fabrication procedures are:

Structure – The substrate used for this structure is Boron-doped Si (111) with a resistivity of 0.01-0.02 Ω.cm. The Mg cell temperature is 210 °C, and the length of Mg-doped region is ~400 nm. The length of non-doped region is ~400 nm. The thickness of *n*-type region is presumably a few nanometers due to the surface electron accumulation.(*80*)

Fabrication procedures – The Ni/Au metal layers were first deposited onto the backside of Si substrate with an e-beam evaporator. The thicknesses for Ni and Au layers are 10 nm and 30 nm, respectively. After that, a PI resist layer was spin-coated to fully cover the InN nanowires. Then, reactive-ion etching (RIE) using O_2 plasma was applied to the sample until the top surface of the nanowires were revealed. The sample was subsequently patterned into cells (called as "device") of various sizes (including 1 by 1 mm^2, 0.5 by 0.5 mm^2, 0.3 by 0.3 mm^2, and 0.1 by 0.1 mm^2) by standard photolithography procedures (the inset of

Figure 8-3(b) shows an example of devices with size of 0.3 by 0.3 mm^2). Thin Ti (5 nm)/Au (5 nm) metal layers were then deposited onto the top of the nanowires to make electrical contacts, after which a thick Au layer in a grid manner (as shown in the inset of Figure 8-3(b)) was made for wire bonding. All the metal contacts were annealed at ~400 °C for 1 minute under a nitrogen atmosphere.

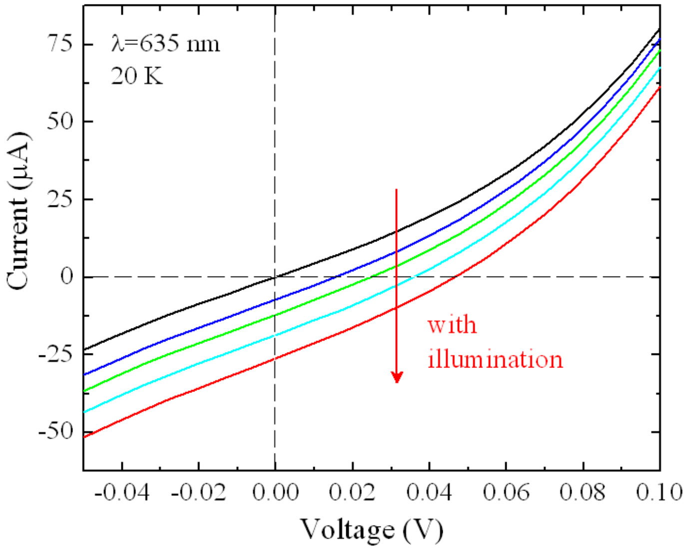

Figure 8-4 *I-V* characteristics of a device with size of 0.5 by 0.5 mm^2 measured at 20 K under dark (the black curve) and red laser (the color curves) illumination with different powers. The arrow denotes the direction of increasing the light intensity.

8.3.2. Optical response of the photodiode

We have performed detailed studies of the light response of the photodiode at low temperatures. The experimental setup is basically modified from the temperature variable PL setup as introduced in Chapter 3, but uses a larger beam size. An additional Keithley 2400 source meter is connected to measure the *I-V* characteristics under dark and illumination conditions. The light sources used have wavelengths of 635 nm, 1064 nm, 1309 nm, and 1580 nm.

Photoresponse was first studied by measuring the low-temperature *I-V* characteristics under dark and with red laser (λ = 635 nm) illumination. As illustrated in Figure 8-4, with red laser illumination the *I-V* curves shift downward, indicating that in the reverse (and zero) bias condition the electrodes are collecting the photo-generated electrons and holes. For a device with size of

0.5 by 0.5 mm^2 (shown in Figure 8-4), the photocurrent density at *zero-bias* condition is ~10 mA/cm^2 with maximum optical power. Further studies over a few devices with different sizes indicate that the photocurrent density varies from 10 mA/cm^2 to 40 mA/cm^2.

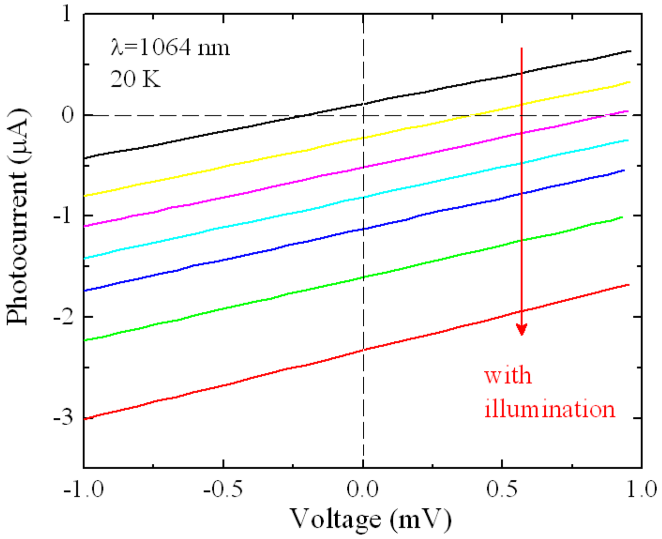

Figure 8-5 *I-V* characteristics of a device with size of 0.5 by 0.5 mm^2 measured at 20 K under dark (the black curve) and infrared laser (the color curves) illumination with different powers. The arrow denotes the direction of increasing the light intensity.

We have further investigated the light response of the *same* device with a light source having a wavelength of λ = 1064 nm. As illustrated in Figure 8-5, a photoresponse similar to that under red laser illumination was observed. Namely, with the light illumination the *I-V* curves shift downward. The corresponding *zero-bias* photocurrent density in this case is calculated to be ~1 mA/cm^2.

Such photoresponse was also observed under light illumination with longer wavelengths (λ = 1309 nm and 1580 nm) at 20 K. The *zero-bias* photocurrent density in this case was estimated to be ~10 μA/cm^2 and ~5 μA/cm^2 for λ = 1309 nm and 1580 nm, respectively. The light response in this telecommunication wavelength range immediately rules out the influence from Si substrate, since the photo energies corresponding to these two wavelengths are significantly smaller compared with the bandgap energy of Si (~1 eV, which is ~1024 nm).

In addition, it should be noted that the light absorption at these two telecommunication wavelengths is very small, and *highly dependent* on the investigated sample quality. For *n*-type degenerate InN, the light absorption at these wavelengths is almost zero. Therefore, the measured light response at these two wavelengths here essentially suggests the superior quality of the presented InN nanowire structures.

8.3.3. High-speed InN nanowire photovoltaic mode photodetector: Discussions and next-phase work

Up to here, a clear photoresponse up to telecommunication wavelength range is demonstrated. We propose such InN nanowire photodiode can be potentially used as a photovoltaic mode photodetector.

Response speed – For the structure shown in Figure 8-3(a), the hole concentration is on the order of 10^{15} cm^{-3} (as estimated in Chapter 7), and assuming accumulated electron density on the top surface is on the order of 10^{19} cm^{-3}, then the built-in potential is estimated to be ~0.6 V. Assuming free charges in intrinsic region are completely depleted, then the width of the depletion region is ~400 nm. This will give a built-in electric field ~12.5 kV/cm, and the electron velocity in Wurtzite InN at this electric field is ~2×10^{7} cm/s.(*64*) Based on these numbers, the electron transient time can be estimated to be ~2 ps. Therefore such photodiode can be operated as a photovoltaic mode photodetector with a modulation frequency about 250 GHz, if the nanowire capacitance and other device parameters can be optimized.

Strategy of carrier confinement – In general, the prompt photocurrent density (J_{prompt}) can be estimated via $J_{prompt} = e\int_0^d \Phi_0 e^{-\alpha x}\alpha\, dx = e\Phi_0(1-e^{-\alpha d})$,[36] where Φ_0 is photon flux area density (# cm^{-2} s^{-1}), α is the absorption coefficient, *d* is the depletion region width, and *e* is the electrical charge unit. For the photodiode as shown in Figure 8-3(a) and under red laser illumination with an optical power of 8

---

[36] Note here we discuss the prompt photocurrent at *zero* bias, and the reverse bias changes the depletion width (*d*), hence changes the prompt photocurrent.

mW and a spot size ~50 µm, J_{prompt} is calculated to be on the order of 10^3 A/cm^2. This number is about 4 orders of magnitude larger than the experimentally measured value (less than 100 mA/cm^2). A few factors could account for this huge difference.

The first factor that needs to be considered is the electron-hole recombination in the depletion region, however, considering the electron transient time (less than 10 picoseconds) is much shorter compared with the carrier lifetime (a few hundred picoseconds to a few nanoseconds), this could only affect J_{prompt} slightly. Actually, the most important factor that degrades J_{prompt} severely is the diffusion of the photo-generated electrons and holes to nanowire surface. Albeit the advantages of large absorption coefficient and electron saturation velocity, InN has large surface recombination velocity that is on the order of 10^5 cm/s.(*69*) The consequence is that the photo-generated electrons and holes will tend to diffuse to the nanowire surface and recombine nonradiatively at surface defects (Shockley-Read-Hall process), which drastically reduces J_{prompt} and the photodetector performance.

We therefore propose an important strategy to improve the performance of InN nanowire photodetector, i.e., the surface passivation, such as using InGaN shell to passivate InN nanowire core, to confine photo-generated carriers in InN nanowire bulk region. This will be a very important part of the future work.

In summary, InN nanowire *p-i-n* photodiodes, which exhibit a photoresponse from the visible to the near-infrared spectrum range, are demonstrated. This provides a very promising route for the photodetection in the near-infrared spectrum range, as well as for telecommunication applications based on InN nanowires on Si platform. Nevertheless, detailed future work is needed, to further characterize the photodetector characteristics such as responsivity and dark current.

9. Conclusions and future work

InN nanowires have emerged as a promising candidate for a range of nanophotonic and nanoelectronic devices, due to the narrow bandgap and extremely large electron mobility. However, the achievement of intrinsic and *p*-type InN nanowires, as well as a fundamental understanding of the surface charge properties has remained elusive *prior* to this thesis work, which severely limits the practical applications of InN nanowires.

In this thesis work, it is demonstrated that *intrinsic* InN nanowires can be achieved by a novel MBE technique, with the near-surface Fermi-level located well below the CBM. More importantly, it is further demonstrated that the surface charge properties, including the surface electron accumulation, surface band bending, as well as the PL characteristics can be *tuned* through the controlled *n*-type doping.

This revolutionary progress provides a solid foundation for the realization of *p*-type InN nanowires. The presence of Mg-acceptors is clearly evidenced by the PL spectra, and *p*-type surface is clearly measured by the XPS experiments. More importantly, the first direct evidence of *p*-type conduction is provided by the single nanowire field effect transistor measurements.

With the achievement of intrinsic and *p*-type InN nanowires, InN nanowire *p-i-n* photodiodes are demonstrated on Si platform, which exhibit a photoresponse from the visible to the near-infrared spectrum range. This offers an entirely new avenue for the near-infrared nanoelectronic and nanophotonic devices on Si platform.

9.1. Potential device applications: An overview

This thesis work immediately leads to a number of electronic and photonic devices based on InN nanowires. Firstly, it is of a great importance to perform a detailed study on the proposed photovoltaic mode InN nanowire photodetectors, to characterize the photodetector characteristics, as well as to further optimize the fabrication process and improve the device performance. Secondly, this thesis work naturally lays the foundation for InN nanowire solar cells/In(Ga)N multijunction solar cells. Thirdly, the InN nanowire *p-i-n* junction can also be used to design high-efficiency LEDs in the infrared spectrum range.

Moreover, nanowires, considering their geometry, could be natural optical cavities in themselves. Nanowire lasers have been demonstrated in other III-nitride systems such as GaN,(*296*) as well as group II-VI materials such as ZnO.(*297*) It would be of great interest to test the lasing of InN nanowires with large diameters. Considering the emission wavelength of InN, it would be suitable for chip-level optical communication applications. Meanwhile, coupling InN nanowires/quantum dots with rolling-up microtubes(*298*) could be another strategy to achieve lasing from InN nanowires. In addition, nanoelectronic devices such as InN nanowire thermoelectric devices, and low-power, ultrahigh-speed nanowire transistors are of great interest to explore.

Up to here, it should be noted that, albeit the advantages of nanowires, there exist drawbacks, which, to a large extent, originate from the large surface-to-bulk volume ratio in nanowires.[37] For example, the surface nonradiative recombination is enhanced due to large surface-to-bulk volume ratio. In addition, large surface states could severely reduce the current injection efficiency in nanowire LEDs, which is believed to be one of the most important factors limiting the efficiency of InGaN/GaN nanowire LEDs.(*205*) In this regard, employing nanowire core-shell structures is of critical importance to further improve device performance.

9.2. Ultrahigh-speed InN nanowire photodetectors on Si: Example I

Compared to conventional Ge and InGaAs-based materials, InN exhibits significantly larger absorption coefficient in the optical communication wavelength range (1.3 – 1.65 μm) and higher carrier saturation velocity, rendering it an excellent candidate for ultrahigh-speed, high responsivity detectors.(*4*) The

---

[37] This large surface-to-bulk volume ratio sometimes becomes problematic, which not only limits practical device applications but also makes it hard to understand the fundamental electrical and optical properties of semiconductor nanowires.

use of nanowires can further enhance the operation bandwidth due to the greatly reduced parasitic capacitance and carrier transient time, promising the detection of optical signal at or above 100 Gb/s.(*169, 273, 285*) We therefore propose to develop ultrahigh-speed InN nanowire photodetectors and detector arrays on Si platform.

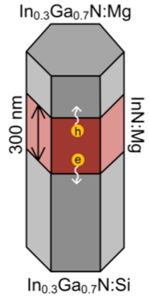

Figure 9-1 A schematic plot of the proposed ~1.55 µm InN-based nanowire photodetectors.

While significant progress has been made in nanowire photodetectors, the achievement of high speed operation has not been reported.(*285*) Illustrated in Figure 9-1, the proposed nanowire photodetectors consist of *p*- and *n*-doped $In_{0.3}Ga_{0.6}N$ cladding layers and a relatively thin (~300 nm) InN active region. Upon illumination (λ ~1.55 µm), electrons and holes are generated in the narrow-bandgap InN (~0.65 eV) intrinsic region, and are subsequently collected by the *n*- and *p*-contacts, respectively. Fast extraction of electron hole pairs from the intrinsic region defines the response time, which can be as low as 10^{-11} s for nanowire devices.(*273*)

One of the primary limiting factors for achieving ultrahigh-speed operation is related to the relatively poor hole transport in the active region, due to the large effective mass and low mobility. In this regard, we will incorporate the special technique of *p*-type doping in the nanowire photodetector active region. With a relatively low (~5×10^{16} cm^{-2}) Mg dopant incorporation, the hole transient time can be significantly reduced without elevating dark current and degrading the device responsivity, thereby leading to InN nanowire photodetectors with further enhanced bandwidth. The optimal doping concentration will be calculated and correlated with experimental results. Meanwhile, the device performance including dark current, responsivity will be investigated. The dependence of device performance on the nanowire diameter and active region thickness will also be studied.

Work will also be conducted on the modeling and performance simulation of integrated nanowire and Si waveguide systems, wherein light is laterally coupled to the nanowire photodetector from an adjacent Si/SiO_2 waveguide. In this configuration, the light absorption path and the charge carrier collection path are separated. Consequently, the device responsivity can be significantly enhanced by increasing the nanowire diameter while using a relatively thin active region, to achieve high-speed operation.

With the successful demonstration of single InN nanowire photodetectors on foreign substrate (means *not* Si), we will further investigate the design, epitaxial growth, fabrication and characterization of large-area vertical InN nanowire photodetectors integrated with Si waveguide on Si platform.

9.3. InN nanowire lasers on Si: Example II

In order to realize electrically injected lasers on Si, heterogeneous integration of group III-V materials with Si has been intensively investigated. However, conventional planar devices on Si generally exhibit very high threshold current (requiring high power consumption) and extremely short lifetime. In this regard, we will further explore InGaN/GaN core-shell nanoscale heterostructures and propose to demonstrate nanowire lasers monolithically grown on Si that can exhibit ultralow threshold current and ultrahigh operation speed.

Although nanowire devices have been intensively investigated, near infrared III-nitride nanowire lasers have *not* been demonstrated to date.(*72, 295-297, 299*) Additionally, the achievement of chip-level nanowire lasers is generally limited by small saturation gain and relatively low optical confinement factor associated with the small modal volume in the nanowire active region. To reduce the threshold gain as well as to achieve high performance lasing, we propose to investigate InGaN-based core-shell nanowire heterostructures. Illustrated in Figure 9-2, $In_{0.9}Ga_{0.1}N$ active region is embedded in $In_{0.4}Ga_{0.6}N$ cladding layers.

Additionally, the nanowire heterostructure is further covered by a thin (~15 – 30 nm), large bandgap $In_{0.5}Ga_{0.5}N$ shell, thereby leading to a strong carrier confinement in the nanowire active region.

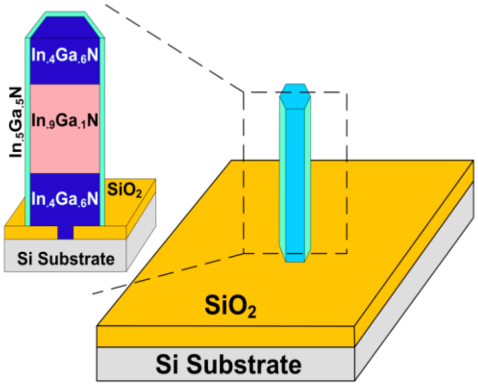

Figure 9-2 The proposed InGaN core-shell nanowire lasers on Si platform.

The nanowires will be grown directly on Si substrate using the SAG technique. In this approach, the presence of a SiO_2 layer can drastically reduce the optical loss through Si substrate. The nanowire laser performance, including the threshold current and output power will be optimized by varying the nanowire diameter, the thickness of active region, as well as the thickness of the SiO_2 layer. We will further study the dependence of optical mode profiles and emission characteristics on the surface morphology of InGaN nanowire heterostructures.

We also propose to develop electrically injected nanowire plasmonic lasers. It has been demonstrated that a very large optical confinement factor can be achieved in nanowire devices with the use of appropriate plasmonic structures, such as a thin metallic layer covering the nanowire surface.(*300-303*) With the use of this technique, the optical confinement will be significantly enhanced in both non-tapered and tapered nanowire heterostructures. Additionally, the direct integration of nanowire lasers with Si waveguide will be explored. The laser performance, including the threshold current, quantum efficiency, and output power will be studied in details and will be correlated with the design and growth parameters.

References

1. S. Strite and H. Morkoc, GaN, AlN, and InN: A review. *Journal of Vacuum Science & Technology B: Microelectronics and Nanometer Structures* **10**, 1237 (1992).
2. A. G. Bhuiyan *et al.*, Indium nitride (InN): A review on growth, characterization, and properties. *Journal of Applied Physics* **94**, 2779 (2003).
3. W. Walukiewicz *et al.*, Structure and electronic properties of InN and In-rich group III-nitride alloys. *Journal of Physics D: Applied Physics* **39**, R83 (2006).
4. J. Wu, When group-III nitrides go infrared: New properties and perspectives. *Journal of Applied Physics* **106**, 011101 (2009).
5. F. A. Ponce and D. P. Bour, Nitride-based semiconductors for blue and green light-emitting devices. *Nature* **386**, 27 (1997).
6. M. H. Crawford, LEDs for Solid-State Lighting: Performance Challenges and Recent Advances. *IEEE Journal of Selected Topics in Quantum Electronics* **15**, 1028 (2009).
7. S. Nakamura *et al.*, Candela-class high-brightness InGaN/AlGaN double-heterostructure blue-light-emitting diodes. *Applied Physics Letters* **64**, 1687 (1994).
8. S. Nakamura *et al.*, High-Brightness InGaN Blue, Green and Yellow Light-Emitting Diodes with Quantum Well Structures. *Japanese Journal of Applied Physics* **34**, L797 (1995).
9. T. Yamada and T. Mukai, Superbright green InGaN single-quantum-well-structure light-emitting diodes. *Japanese Journal of Applied Physics* **34**, 1332 (1995).
10. F. Hide *et al.*, White light from InGaN/conjugated polymer hybrid light-emitting diodes. *Applied Physics Letters* **70**, 2664 (1997).
11. S. Nakamura, The Roles of Structural Imperfections in InGaN-Based Blue Light-Emitting Diodes and Laser Diodes. *Science* **281**, 956 (1998).
12. T. Mukai *et al.*, Characteristics of InGaN-Based UV/Blue/Green/Amber/Red Light-Emitting Diodes. *Japanese Journal of Applied Physics* **38**, 3976 (1999).
13. W. S. Wong *et al.*, Fabrication of thin-film InGaN light-emitting diode membranes by laser lift-off. *Applied Physics Letters* **75**, 1360 (1999).
14. J. J. Wierer *et al.*, InGaN/GaN quantum-well heterostructure light-emitting diodes employing photonic crystal structures. *Applied Physics Letters* **84**, 3885 (2004).
15. S. Nakamura *et al.*, InGaN-Based Multi-Quantum-Well-Structure Laser Diodes. *Japanese Journal of Applied Physics* **35**, 74 (1996).
16. S. Nakamura *et al.*, Room-temperature continuous-wave operation of InGaN multi-quantum-well structure laser diodes with a lifetime of 27 hours. *Applied Physics Letters* **70**, 1417 (1997).

17. Y. Narukawa *et al.*, Role of self-formed InGaN quantum dots for exciton localization in the purple laser diode emitting at 420 nm. *Applied Physics Letters* **70**, 981 (1997).
18. S. Nakamura *et al.*, InGaN/GaN/AlGaN-based laser diodes with modulation-doped strained-layer superlattices grown on an epitaxially laterally overgrown GaN substrate. *Applied Physics Letters* **72**, 211 (1998).
19. F. Della Sala *et al.*, Free-carrier screening of polarization fields in wurtzite GaN/InGaN laser structures. *Applied Physics Letters* **74**, 2002 (1999).
20. S. Nakamura *et al.*, *The Blue Laser Diode: The Complete Story*. (Springer, 2000).
21. D. Queren *et al.*, 500 nm electrically driven InGaN based laser diodes. *Applied Physics Letters* **94**, 081119 (2009).
22. A. Osinsky *et al.*, Low noise p-π-n GaN ultraviolet photodetectors. *Applied Physics Letters* **71**, 2334 (1997).
23. F. Binet *et al.*, Mechanisms of recombination in GaN photodetectors. *Applied Physics Letters* **69**, 1202 (1996).
24. G. Y. Xu *et al.*, High speed, low noise ultraviolet photodetectors based on GaN p-i-n and AlGaN(p)-GaN(i)-GaN(n)structures. *Applied Physics Letters* **71**, 2154 (1997).
25. E. Miyazaki *et al.*, Using a light-emitting diode as a high-speed, wavelength selective photodetector. *Review of Scientific Instruments* **69**, 3751 (1998).
26. F. Omnès *et al.*, Metalorganic vapor-phase epitaxy-grown AlGaN materials for visible-blind ultraviolet photodetector applications. *Journal of Applied Physics* **86**, 5286 (1999).
27. E. Munoz *et al.*, III nitrides and UV detection. *Journal of Physics: Condensed Matter* **13**, 7115 (2001).
28. Y.-Z. Chiou *et al.*, High Detectivity InGaN–GaN Multiquantum Well p–n Junction Photodiodes. *IEEE Journal of Quantum Electronoics* **5**, 681 (2003).
29. L. W. Ji *et al.*, InGaN quantum dot photodetectors. *Solid-State Electronics* **47**, 1753 (2003).
30. R. McClintock *et al.*, High quantum efficiency AlGaN solar-blind p-i-n photodiodes. *Applied Physics Letters* **84**, 1248 (2004).
31. A. Vardi *et al.*, Near infrared quantum cascade detector in GaN∕AlGaN∕AlN heterostructures. *Applied Physics Letters* **92**, 011112 (2008).
32. J. Pereiro *et al.*, Optimization of InGaN–GaN MQW Photodetector Structures for High-Responsivity Performance. *IEEE Journal of Quantum Electronoics* **45**, 6 (2009).
33. J. Wu *et al.*, Superior radiation resistance of In1−xGaxN alloys: Full-solar-spectrum photovoltaic material system. *Journal of Applied Physics* **94**, 6477 (2003).
34. O. Jani *et al.*, Design and characterization of GaN∕InGaN solar cells. *Applied Physics Letters* **91**, 132117 (2007).

35. C. J. Neufeld *et al.*, High quantum efficiency InGaN/GaN solar cells with 2.95 eV band gap. *Applied Physics Letters* **93**, 143502 (2008).
36. X. Zheng *et al.*, High-quality InGaN⁄GaN heterojunctions and their photovoltaic effects. *Applied Physics Letters* **93**, 261108 (2008).
37. X.-m. Cai *et al.*, Fabrication and characterization of InGaN p-i-n homojunction solar cell. *Applied Physics Letters* **95**, 173504 (2009).
38. A. Yamamoto *et al.*, Recent advances in InN-based solar cells: status and challenges in InGaN and InAlN solar cells. *physica status solidi (c)* **7**, 1309 (2010).
39. A. G. Bhuiyan *et al.*, InGaN Solar Cells: Present State of the Art and Important Challenges. *IEEE Journal of Photovotaics* **2**, 276 (2012).
40. M. Asif Khan *et al.*, High electron mobility transistor based on a GaN-AlxGa1−xN heterojunction. *Applied Physics Letters* **63**, 1214 (1993).
41. M. Asif Khan *et al.*, Microwave performance of a 0.25 μm gate AlGaN/GaN heterostructure field effect transistor. *Applied Physics Letters* **65**, 1121 (1994).
42. Y. Zhang and J. Singh, Charge control and mobility studies for an AlGaN/GaN high electron mobility transistor. *Journal of Applied Physics* **85**, 587 (1999).
43. M. A. Khan *et al.*, AlGaN/GaN Metal Oxide Semiconductor Heterostructure Field Effect Transistor. *IEEE Electron Device Letters* **21**, 63 (2000).
44. P. D. Ye *et al.*, GaN metal-oxide-semiconductor high-electron-mobility-transistor with atomic layer deposited Al2O3 as gate dielectric. *Applied Physics Letters* **86**, 063501 (2005).
45. T. Palacios *et al.*, AlGaN/GaN High Electron Mobility Transistors With InGaN Back-Barriers. *IEEE Electron Device Letters* **27**, 13 (2006).
46. D. Starikov *et al.*, paper presented at the Sensors for Industry Conference, 2002.
47. S. J. Chang *et al.*, GaN-Based p-i-n Sensors With ITO Contacts. *IEEE Sensors Journal* **6**, 2 (2006).
48. J. L. Pau *et al.*, Optical sensors based on III-nitride photodetectors for flame sensing and combustion monitoring. *Applied Optics* **45**, 7498 (2006).
49. S. Paul *et al.*, in *The 14th International Meeting on Chemical Sensors*. (2012), pp. 653.
50. D.-H. Kim *et al.*, Inorganic semiconductor nanomaterials for flexible and stretchable bio-integrated electronics. *NPG Asia Materials* **4**, e15 (2012).
51. Z. Fan *et al.*, Three-dimensional nanopillar-array photovoltaics on low-cost and flexible substrates. *Nature Matererials* **8**, 648 (2009).
52. J. A. Rogers *et al.*, Synthesis, assembly and applications of semiconductor nanomembranes. *Nature* **477**, 45 (2011).
53. J. H. Choi *et al.*, Nearly single-crystalline GaN light-emitting diodes on amorphous glass substrates. *Nature Photonics* **5**, 763 (2011).
54. T. Matsuoka *et al.*, Optical bandgap energy of wurtzite InN. *Applied Physics Letters* **81**, 1246 (2002).

55. J. Wu *et al.*, Unusual properties of the fundamental band gap of InN. *Applied Physics Letters* **80**, 3967 (2002).
56. J. Wu *et al.*, Effects of the narrow band gap on the properties of InN. *Physical Review B* **66**, 201403 (2002).
57. V. Yu. Davydov *et al.*, Absorption and Emission of Hexagonal InN: Evidence of Narrow Fundamental Band Gap. *Physica Status Solidi (b)* **229**, r1 (2002).
58. Y. L. Chang *et al.*, Molecular beam epitaxial growth and characterization of non-tapered InN nanowires on Si(111). *Nanotechnology* **20**, 345203 (2009).
59. Y. L. Chang *et al.*, Photoluminescence Properties of a Nearly Intrinsic Single InN Nanowire. *Advanced Functional Materials* **20**, 4146 (2010).
60. S. Zhao *et al.*, Observation of phonon sideband emission in intrinsic InN nanowires: a photoluminescence and micro-Raman scattering study. *Nanotechnology* **23**, 415706 (2012).
61. S. Zhao *et al.*, Understanding the role of Si doping on surface charge and optical properties: Photoluminescence study of intrinsic and Si-doped InN nanowires. *Physical Review B* **85**, 245313 (2012).
62. S. Zhao *et al.*, Tuning the surface charge properties of epitaxial InN nanowires. *Nano letters* **12**, 2877 (2012).
63. M. E. Holtz *et al.*, Influence of phonons on the temperature dependence of photoluminescence in InN with low carrier concentration. *Journal of Applied Physics* **105**, 063702 (2009).
64. V. M. Polyakov *et al.*, Low-field and high-field electron transport in zinc blende InN. *Applied Physics Letters* **94**, 022102 (2009).
65. X. Wang *et al.*, High-Electron-Mobility InN Layers Grown by Boundary-Temperature-Controlled Epitaxy. *Applied Physics Express* **5**, 015502 (2012).
66. S. Wang *et al.*, Monte Carlo calculation of electron diffusion coefficient in wurtzite indium nitride. *Applied Physics Letters* **100**, 142105 (2012).
67. S. Aydogu *et al.*, InN and ln1−xGaxN: calculation of hall mobilities and effects of alloy disorder and dislocation scatterings. *Materials Science in Semiconductor Processing* **15**, 347 (2012).
68. J. R. Meyer and F. J. Bartoli, About InN mobility theoretical calculations. *Physical Review B* **36**, 5989 (1987).
69. E. F. Schubert, *Light-Emitting Diodes, 2nd edition*. Cambridge University Press (2006).
70. J. Y. Tsao *et al.*, Solid-State Lighting: An Integrated Human Factors, Technology, and Economic Perspective. *Proceedings of the IEEE* **98**, 1162 (2010).
71. D. Wang *et al.*, Wafer-level photocatalytic water splitting on GaN nanowire arrays grown by molecular beam epitaxy. *Nano letters* **11**, 2353 (2011).
72. S. Fathololoumi *et al.*, Self-organized In(Ga)N nanowire heterostructures and optoelectronic device applications. *Nanoscience & Nanotechnology Asia* **1**, 123 (2011).

73. Y. Enya *et al.*, 531 nm Green Lasing of InGaN Based Laser Diodes on Semi-Polar {20-21} Free-Standing GaN Substrates. *Applied Physics Express* **2**, 082101 (2009).
74. G. F. Brown *et al.*, Probing and modulating surface electron accumulation in InN by the electrolyte gated Hall effect. *Applied Physics Letters* **93**, 262105 (2008).
75. P. A. Anderson *et al.*, Buried p-type layers in Mg-doped InN. *Applied Physics Letters* **89**, 184104 (2006).
76. A. Klochikhin *et al.*, Acceptor states in the photoluminescence spectra of n-InN. *Physical Review B* **71**, 195207 (2005).
77. B. Arnaudov *et al.*, Energy position of near-band-edge emission spectra of InN epitaxial layers with different doping levels. *Physical Review B* **69**, 115216 (2004).
78. S. P. Fu *et al.*, Anomalous Optical Properties of InN Nanobelts: Evidence of Surface Band Bending and Photoelastic Effects. *Advanced Materials* **19**, 4524 (2007).
79. S. P. Fu, *et al.*, Recombination mechanism of photoluminescence in InN epilayers. *Solid State Communications* **137**, 203 (2006).
80. I. Mahboob *et al.*, Intrinsic Electron Accumulation at Clean InN Surfaces. *Physical Review Letters* **92**, 036804 (2004).
81. I. Mahboob *et al.*, Origin of electron accumulation at wurtzite InN surfaces. *Physical Review B* **69**, R201307 (2004).
82. L. Piper *et al.*, Temperature invariance of InN electron accumulation. *Physical Review B* **70**, 115333 (2004).
83. T. D. Veal *et al.*, Indium nitride: Evidence of electron accumulation. *Journal of Vacuum Science & Technology B: Microelectronics and Nanometer Structures* **22**, 2175 (2004).
84. L. F. J. Piper *et al.*, Origin of the n-type conductivity of InN: The role of positively charged dislocations. *Applied Physics Letters* **88**, 252109 (2006).
85. P. D. C. King *et al.*, Universality of electron accumulation at wurtzite c- and a-plane and zinc-blende InN surfaces. *Applied Physics Letters* **91**, 092101 (2007).
86. M. Feneberg *et al.*, Mahan excitons in degenerate wurtzite InN: Photoluminescence spectroscopy and reflectivity measurements. *Physical Review B* **77**, 245207 (2008).
87. A. Mohanta *et al.*, Carrier recombination dynamics in Si doped InN thin films. *Journal of Applied Physics* **110**, 023703 (2011).
88. C. Rauch *et al.*, In-vacancies in Si-doped InN. *Physica Status Solidi (a)* **207**, 1083 (2010).
89. S. P. Fu *et al.*, Photoluminescent properties of InN epifilms. *Semiconductor Science and Technology* **21**, 244 (2006).
90. G. D. Mahan, Excitons in Degenerate Semiconductors. *Physical Review* **153**, 882 (1967).

91. Y. M. Chang *et al.*, Coherent longitudinal optical phonon and plasmon coupling in the near-surface region of InN. *Applied Physics Letters* **85**, 5224 (2004).
92. V. Yu. Davydov *et al.*, Experimental and theoretical studies of phonons in hexagonal InN. *Applied Physics Letters* **75**, 3297 (1999).
93. K. Jeganathan *et al.*, Raman scattering on intrinsic surface electron accumulation of InN nanowires. *Applied Physics Letters* **97**, 093104 (2010).
94. S. Lazic *et al.*, Raman scattering by longitudinal optical phonons in InN nanocolumns grown on Si(111) and Si(001) substrates. *Physica E: Low-dimensional Systems and Nanostructures* **40**, 2087 (2008).
95. J. Pomeroy *et al.*, Evidence for phonon-plasmon interaction in InN by Raman spectroscopy. *Physical Review B* **75**, 035205 (2007).
96. H. Lu *et al.*, Effect of an AlN buffer layer on the epitaxial growth of InN by molecular-beam epitaxy. *Applied Physics Letters* **79**, 1489 (2001).
97. D. C. Look *et al.*, Donor and acceptor concentrations in degenerate InN. *Applied Physics Letters* **80**, 258 (2002).
98. C.-T. Kuo *et al.*, Is electron accumulation universal at InN polar surfaces? *Applied Physics Letters* **98**, 052101 (2011).
99. E. Calleja *et al.*, Evidence of electron accumulation at nonpolar surfaces of InN nanocolumns. *Applied Physics Letters* **90**, 262110 (2007).
100. C.-L. Wu *et al.*, Absence of Fermi-Level Pinning at Cleaved Nonpolar InN Surfaces. *Physical Review Letters* **101**, 106803 (2008).
101. H. Eisele and P. Ebert, Non-polar group-III nitride semiconductor surfaces. *Physica Status Solidi -Rapid Research Letters*, 1-11 (2012).
102. P. Ebert *et al.*, Direct measurement of the band gap and Fermi level position at InN(1120). *Applied Physics Letters* **98**, 062103 (2011).
103. J. H. Chai *et al.*, Optical and electrical characteristics of Mn-doped InN grown by plasma-assisted molecular beam epitaxy. *Physica Status Solidi (a)* **209**, 95 (2012).
104. J. Wang *et al.*, InN doped with Zn: Bulk and surface investigation from first principles. *Solid State Communications* **152**, 1168 (2012).
105. A. Yoshikawa *et al.*, Recent advances and challenges for successful p-type control of InN films with Mg acceptor doping by molecular beam epitaxy. *Physica Status Solidi (a)* **207**, 1011 (2010).
106. C. G. Van de Walle *et al.*, Controlling the conductivity of InN. *Physica Status Solidi (a)* **207**, 1024 (2010).
107. M. A. Mayer *et al.*, Electrical and optical properties of p-type InN. *Journal of Applied Physics* **110**, 123707 (2011).
108. X. Wang *et al.*, Growth and properties of Mg-doped In-polar InN films. *Applied Physics Letters* **90**, 201913 (2007).
109. N. Khan *et al.*, Mg acceptor level in InN epilayers probed by photoluminescence. *Applied Physics Letters* **91**, 012101 (2007).
110. X. Wang *et al.*, Hole mobility in Mg-doped p-type InN films. *Applied Physics Letters* **92**, 132108 (2008).

111. K. Wang *et al.*, Mg doped InN and confirmation of free holes in InN. *Applied Physics Letters* **98**, 042104 (2011).
112. J. W. Ager *et al.*, Mg-doped InN and InGaN – Photoluminescence, capacitance–voltage and thermopower measurements. *Physica Status Solidi (b)* **245**, 873 (2008).
113. X. Wang *et al.*, Systematic study on p-type doping control of InN with different Mg concentrations in both In and N polarities. *Applied Physics Letters* **91**, 242111 (2007).
114. L. H. Dmowski *et al.*, Search for free holes in InN:Mg-interplay between surface layer and Mg-acceptor doped interior. *Journal of Applied Physics* **105**, 123713 (2009).
115. L. H. Dmowski *et al.*, Coexistence of free holes and electrons in InN:Mg with In- and N-growth polarities. *Journal of Applied Physics* **111**, 093719 (2012).
116. T. A. Komissarova and S. V. Ivanov, Comment on "Hole transport and photoluminescence in Mg-doped InN" [Journal of Applied Physiscs **107**, 113712 (2010)]. *arXiv:1101.1494v1* (2011).
117. M. Moseley *et al.*, Transient atomic behavior and surface kinetics of GaN. *Journal of Applied Physics* **106**, 014905 (2009).
118. P. D. C. King *et al.*, Surface Electron Accumulation and the Charge Neutrality Level in In2O3. *Physical Review Letters* **101**, 116808 (2008).
119. L. Piper *et al.*, Observation of quantized subband states and evidence for surface electron accumulation in CdO from angle-resolved photoemission spectroscopy. *Physical Review B* **78**, 165127 (2008).
120. C. G. Van de Walle and J. Neugebauer, Universal alignment of hydrogen levels in semiconductors, insulators and solutions. *Nature* **423**, 626 (2003).
121. P. D. C. King *et al.*, Determination of the branch-point energy of InN: Chemical trends in common-cation and common-anion semiconductors. *Physical Review B* **77**, 045316 (2008).
122. V. Darakchieva *et al.*, Electron accumulation at nonpolar and semipolar surfaces of wurtzite InN from generalized infrared ellipsometry. *Applied Physics Letters* **95**, 202103 (2009).
123. L. Colakerol *et al.*, Observation of an inverted band structure near the surface of InN. *Europhysics Letters* **83**, 47003 (2008).
124. M. Noguchi *et al.*, Intrinsic electron accumulation layers on reconstructed clean InAs(100) surfaces. *Physical Review Letters* **66**, 2243 (1991).
125. C. G. Van de Walle and D. Segev, Microscopic origins of surface states on nitride surfaces. *Journal of Applied Physics* **101**, 081704 (2007).
126. T. Stoica *et al.*, Photoluminescence and intrinsic properties of MBE-grown InN nanowires. *Nano letters* **6**, 1541 (2006).
127. T. Richter *et al.*, Electrical transport properties of single undoped and n-type doped InN nanowires. *Nanotechnology* **20**, 405206 (2009).
128. F. Werner *et al.*, Electrical conductivity of InN nanowires and the influence of the native indium oxide formed at their surface. *Nano letters* **9**, 1567 (2009).

129. C. H. Shen *et al.*, Near-infrared photoluminescence from vertical InN nanorod arrays grown on silicon: Effects of surface electron accumulation layer. *Applied Physics Letters* **88**, 253104 (2006).
130. J. Segura-Ruiz *et al.*, Inhomogeneous free-electron distribution in InN nanowires: Photoluminescence excitation experiments. *Physical Review B* **82**, 125319 (2010).
131. F. Glas, Critical dimensions for the plastic relaxation of strained axial heterostructures in free-standing nanowires. *Physical Review B* **74**, r121302 (2006).
132. E. Calleja *et al.*, Growth, morphology, and structural properties of group-III-nitride nanocolumns and nanodisks. *Physica Status Solidi (b)* **244**, 2816 (2007).
133. J. Ristić *et al.*, On the mechanisms of spontaneous growth of III-nitride nanocolumns by plasma-assisted molecular beam epitaxy. *Journal of Crystal Growth* **310**, 4035 (2008).
134. H. Xiang *et al.*, Strain relaxation and band-gap tunability in ternary InxGa1−xN nanowires. *Physical Review B* **78**, 193301 (2008).
135. M. Knelangen *et al.*, In situ analysis of strain relaxation during catalyst-free nucleation and growth of GaN nanowires. *Nanotechnology* **21**, 245705 (2010).
136. G. E. Moore, Progress in digital integrated electronics. *Electron Devices Meeting* **21**, 11 (1975).
137. G. E. Moore, Lithography and the future of Moore's law. *Proceedings of SPIE* **2438**, 2 (1995).
138. R. R. Schaller, Moore's law: past, present and future. *IEEE Spectrum* **34**, 52 (1997).
139. T. Tang *et al.*, Synthesis and characterization of single-crystal indium nitride nanowires. *Journal of Materials Research* **19**, 423 (2004).
140. M. C. Johnson *et al.*, Growth and morphology of 0.80 eV photoemitting indium nitride nanowires. *Applied Physics Letters* **85**, 5670 (2004).
141. C. H. Liang *et al.*, Selective-area growth of indium nitride nanowires on gold-patterned Si(100) substrates. *Applied Physics Letters* **81**, 22 (2002).
142. N. Wang *et al.*, Growth of nanowires. *Materials Science and Engineering: Reports* **60**, 1 (2008).
143. J. Zhang *et al.*, Vapor–solid growth route to single-crystalline indium nitride nanowires. *Journal of Materials Chemistry* **12**, 802 (2002).
144. T. Stoica *et al.*, *IEEE Journal of Selected Topics in Quantum Electronics* **17**, 859 (2011).
145. J. Grandal *et al.*, InN nanocolumns grown by plasma-assisted molecular beam epitaxy on A-plane GaN templates. *Applied Physics Letters* **94**, 221908 (2009).
146. J. Segura-Ruiz *et al.*, Optical studies of MBE-grown InN nanocolumns: Evidence of surface electron accumulation. *Physical Review B* **79**, 115305 (2009).

147. M. A. Sánchez-García *et al.*, Epitaxial growth and characterization of InN nanorods and compact layers on silicon substrates. *Physica Status Solidi (b)* **243**, 1490 (2006).
148. R. Cuscó *et al.*, Temperature dependence of Mg-H local vibrational modes in heavily doped InN:Mg. *Journal of Applied Physics* **112**, 053528 (2012).
149. R. Cuscó *et al.*, Probing the electron density in undoped, Si-doped, and Mg-doped InN nanowires by means of Raman scattering. *Applied Physics Letters* **97**, 221906 (2010); E. O. Schafer-Nolte *et al.*, Enhanced light scattering of the forbidden longitudinal optical phonon mode studied by micro-Raman spectroscopy on single InN nanowires. *Nanotechnology* **21**, 315702 (2010)
150. R. Cuscó *et al.*, Raman scattering study of background electron density in InN: a hydrodynamical approach to the LO-phonon-plasmon coupled modes. *Journal of physics: Condensed matter* **21**, 415801 (2009).
151. G. Cheng *et al.*, Electronic properties of InN nanowires. *Applied Physics Letters* **87**, 253103 (2005).
152. V. M. Polyakov and F. Schwierz, Monte Carlo calculation of two-dimensional electron gas mobility in InN-based heterostructures. *Journal of Applied Physics* **101**, 033703 (2007).
153. V. M. Polyakov and F. Schwierz, Influence of interface roughness on two-dimensional electron gas streaming transport in GaN-based heterostructures. *Journal of Applied Physics* **100**, 103704 (2006).
154. V. M. Polyakov and F. Schwierz, Low-field electron mobility in wurtzite InN. *Applied Physics Letters* **88**, 032101 (2006).
155. I. M. Tiginyanu *et al.*, Luminescence of GaN nanocolumns obtained by photon-assisted anodic etching. *Applied Physics Letters* **83**, 1551 (2003).
156. M. Endo *et al.*, Reactive ion beam etching of GaN and AlGaN/GaN for nanostructure fabrication using methane-based gas mixtures. *Japanese Journal of Applied Physics* **41**, 2689 (2002).
157. S.-Y. Park *et al.*, Fabrication of nanowires with high aspect ratios utilized by dry etching with SF6:C4F8 and self-limiting thermal oxidation on Si substrate. *Journal of Vacuum Science & Technology B: Microelectronics and Nanometer Structures* **28**, 763 (2010).
158. M. Q. He *et al.*, Growth of large-scale GaN nanowires and tubes by direct reaction of Ga with NH3. *Applied Physics Letters* **77**, 3731 (2000).
159. J. Zhang *et al.*, Micro-Raman investigation of GaN nanowires prepared by direct reaction Ga with NH3. *Chemical Physics Letters* **345**, 372 (2001).
160. M. S. Hu *et al.*, Sharp Infrared Emission from Single-Crystalline Indium Nitride Nanobelts Prepared Using Guided-Stream Thermal Chemical Vapor Deposition. *Advanced Functional Materials* **16**, 537 (2006).
161. Z. Cai *et al.*, Synthesis and Properties of High-Quality InN Nanowires and Nanonetworks. *Journal of Electronic Materials* **37**, 585 (2008).
162. L.-W. Yin *et al.*, Growth of Single-Crystal Indium Nitride Nanotubes and Nanowires by a Controlled-Carbonitridation Reaction Route. *Advanced Materials* **16**, 1833 (2004).

163. M. He and S. Noor Mohammad, Novelty and versatility of self-catalytic nanowire growth: A case study with InN nanowires. *Journal of Vacuum Science & Technology B: Microelectronics and Nanometer Structures* **25**, 940 (2007).
164. H. Liu and G. Cheng, Indium Predeposition-Enabled Vapor–Liquid–Solid Growth of InN Nanowires. *Applied Physics Express* **4**, 105002 (2011).
165. J. Zhang *et al.*, Controllable Growth of InN Nanostructures. *Journal of Nanoengineering and Nanomanufacturing* **2**, 112 (2012).
166. S. Vaddiraju *et al.*, Mechanisms of 1D crystal growth in reactive vapor transport: indium nitride nanowires. *Nano letters* **5**, 1625 (2005).
167. M. Lei *et al.*, Catalyst-free chemical vapor deposition route to InN nanowires and their cathodoluminescence properties. *Journal of Alloys and Compounds* **535**, 50 (2012).
168. T.-T. Kang *et al.*, InN nanoflowers grown by metal organic chemical vapor deposition. *Applied Physics Letters* **89**, 071113 (2006).
169. W. Lu and C. M. Lieber, Semiconductor nanowires. *Journal of Physics D: Applied Physics* **39**, r387 (2006).
170. L. Geelhaar *et al.*, Properties of GaN Nanowires Grown by Molecular Beam Epitaxy. *IEEE Journal of Selected Topics in Quantum Electronics* **17**, 878 (2011).
171. K. A. Bertness *et al.*, GaN Nanowires Grown by Molecular Beam Epitaxy. *IEEE Journal of Selected Topics in Quantum Electronics* **17**, 847 (2011).
172. C. K. Chao *et al.*, Catalyst-free growth of indium nitride nanorods by chemical-beam epitaxy. *Applied Physics Letters* **88**, 233111 (2006).
173. T. Shioda *et al.*, Selective area metal-organic vapor-phase epitaxy of InN, GaN and InGaN covering whole composition range. *Journal of Crystal Growth* **311**, 2809 (2009).
174. G. Liu *et al.*, Selective area epitaxy of ultra-high density InGaN quantum dots by diblock copolymer lithography. *Nanoscale Research Letters* **6**, 342 (2011).
175. D. Kapolnek *et al.*, Anisotropic epitaxial lateral growth in GaN selective area epitaxy. *Applied Physics Letters* **71**, 1204 (1997).
176. H. Fang *et al.*, Analysis of mass transport mechanism in InGaN epitaxy on ridge shaped selective area growth GaN by metal organic chemical vapor deposition. *Journal of Applied Physics* **103**, 014908 (2008).
177. T. Henry *et al.*, Directed Growth of Horizontally Aligned Gallium Nitride Nanowires for Nanoelectromechanical Resonator Arrays. *Nano letters* **7**, 3315 (2007).
178. D. Tsivion *et al.*, Guided growth of millimeter-long horizontal nanowires with controlled orientations. *Science* **333**, 1003 (2011).
179. J. Kamimura *et al.*, Dislocation reduction via selective-area growth of InN accompanied by lateral growth by rf-plasma-assisted molecular-beam epitaxy. *Applied Physics Letters* **97**, 141913 (2010).
180. T. Schumann *et al.*, Selective-area catalyst-free MBE growth of GaN nanowires using a patterned oxide layer. *Nanotechnology* **22**, 095603 (2011).

181. K. Kishino *et al.*, Improved Ti-mask selective-area growth (SAG) by rf-plasma-assisted molecular beam epitaxy demonstrating extremely uniform GaN nanocolumn arrays. *Journal of Crystal Growth* **311**, 2063 (2009).
182. M. C. Plante and R. R. LaPierre, Growth mechanisms of GaAs nanowires by gas source molecular beam epitaxy. *Journal of Crystal Growth* **286**, 394 (2006).
183. A. I. Persson *et al.*, Solid-phase diffusion mechanism for GaAs nanowire growth. *Nature materials* **3**, 677 (2004).
184. R. S. Wagner and W. C. Ellis, Vapor-liquid-solid mechanism of single crystal growth. *Applied Physics Letters* **4**, 89 (1964).
185. Y. Y. Cao and G. W. Yang, Vertical or Horizontal: Understanding Nanowire Orientation and Growth from Substrates. *The Journal of Physical Chemistry C* **116**, 6233 (2012).
186. B. A. Wacaser *et al.*, Preferential Interface Nucleation: An Expansion of the VLS Growth Mechanism for Nanowires. *Advanced Materials* **21**, 153 (2009).
187. J. Liu *et al.*, Charge transport and trapping in InN nanowires investigated by scanning probe microscopy. *Journal of Applied Physics* **106**, 124907 (2009).
188. K. Goodman *et al.*, Molecular beam epitaxial growth of gallium nitride nanowires on atomic layer deposited aluminum oxide. *Journal of Crystal Growth* **334**, 113 (2011).
189. K. Bertness *et al.*, Mechanism for spontaneous growth of GaN nanowires with molecular beam epitaxy. *Journal of Crystal Growth* **310**, 3154 (2008).
190. R. K. Debnath *et al.*, Mechanism of molecular beam epitaxy growth of GaN nanowires on Si(111). *Applied Physics Letters* **90**, 123117 (2007).
191. T. Stoica *et al.*, Interface and wetting layer effect on the catalyst-free nucleation and growth of GaN nanowires. *Small* **4**, 751 (2008).
192. V. Consonni *et al.*, Nucleation mechanisms of self-induced GaN nanowires grown on an amorphous interlayer. *Physical Review B* **83**, 035310 (2011).
193. V. Dubrovskii *et al.*, Theoretical analysis of the vapor-liquid-solid mechanism of nanowire growth during molecular beam epitaxy. *Physical Review E* **73**, 021603 (2006).
194. J. Grandal *et al.*, Accommodation mechanism of InN nanocolumns grown on Si(111) substrates by molecular beam epitaxy. *Applied Physics Letters* **91**, 021902 (2007).
195. C. Chèze *et al.*, Different growth rates for catalyst-induced and self-induced GaN nanowires. *Applied Physics Letters* **97**, 153105 (2010).
196. M. C. McAlpine *et al.*, High-Performance Nanowire Electronics and Photonics on Glass and Plastic Substrates. *Nano Letters* **3**, 1531 (2003).
197. N. C. Vega *et al.*, ZnO nanowire co-growth on SiO2 and C by carbothermal reduction and vapour advection. *Nanotechnology* **23**, 275602 (2012).

198. A. Shadi *et al.*, Growth of InAs nanowires on SiO2 substrates: Nucleation, evolution, and the role of Au nanoparticles. *The Journal of Physical Chemistry C* **111**, 13331 (2007).
199. F. Jabeen *et al.*, Growth of III–V semiconductor nanowires by molecular beam epitaxy. *Microelectronics Journal* **40**, 442 (2009).
200. A. T. Hui *et al.*, High-performance indium phosphide nanowires synthesized on amorphous substrates: from formation mechanism to optical and electrical transport measurements. *Journal of Materials Chemistry* **22**, 10704 (2012).
201. N. Han *et al.*, Facile synthesis and growth mechanism of Ni-catalyzed GaAs nanowires on non-crystalline substrates. *Nanotechnology* **22**, 285607 (2011).
202. S. Han *et al.*, Controlled growth of gallium nitride single-crystal nanowires using a chemical vapor deposition method. *Journal of Materials Research* **18**, 245 (2003).
203. D. Comedi *et al.*, Randomly oriented ZnO nanowires grown on amorphous SiO2 by metal-catalyzed vapour deposition. *Journal of Alloys and Compounds* **495**, 439 (2010).
204. R. Calarco *et al.*, Nucleation and Growth of GaN Nanowires on Si(111) Performed by Molecular Beam Epitaxy. *Nano Letters* **7**, 2248 (2007).
205. H. P. T. Nguyen *et al.*, p-Type modulation doped InGaN/GaN dot-in-a-wire white-light-emitting diodes monolithically grown on Si(111). *Nano Letters* **11**, 1919 (2011).
206. K. S. A. Butcher *et al.*, Initial Experiments in the Migration Enhanced Afterglow Growth of Gallium and Indium Nitride. *Physica Status Solidi (c)* **9**, 1070 (2012).
207. K. S. A. Butcher *et al.*, InN Grown by Migration Enhanced Afterglow. *Physica Status Solidi (a)* **209**, 41 (2012).
208. K. S. A. Butcher *et al.*, Gallium Nitride Film Growth using a Plasma Based Migration Enhanced Afterglow (MEAglow) CVD System. *Japanese Journal of Applied Physics* **51**, 01AF02 (2012).
209. T. Schmidt *et al.*, Excitation-power dependence of the near-band-edge photoluminescence of semiconductors. *Physical Review B* **45**, 8989 (1992).
210. M. Moret *et al.*, The determination of the bulk residual doping in indium nitride films using photoluminescence. *Applied Physics Letters* **95**, 031910 (2009).
211. A. Smekal, Zur quantentheorie der dispersion. *Naturwissenschaften* **11**, 873 (1923).
212. C. V. Raman and K. S. Krishnan, A new type of secondary radiation. *Nature* **121**, 501 (1928).
213. H. Harima, Properties of GaN and related compounds studied by means of Raman scattering. *Journal of Physics: Condensed Matter* **14**, r967 (2002).
214. J. W. Pomeroy *et al.*, Phonon lifetimes and phonon decay in InN. *Applied Physics Letters* **86**, 223501 (2005).

215. S. Lazić *et al.*, Phonon-plasmon coupling in electron surface accumulation layers in InN nanocolumns. *Physical Review B* **76**, 205319 (2007).
216. A. Kasic *et al.*, Effective electron mass and phonon modes in n-type hexagonal InN. *Physical Review B* **65**, 115206 (2002).
217. V. Yu. Davydov *et al.*, Selective excitation of E1(LO) and A1(LO) phonons with large wave vectors in the Raman spectra of hexagonal InN. *Physical Review B* **80**, r081204 (2009).
218. V. Yu. Davydov *et al.*, Experimental and theoretical studies of lattice dynamics of Mg-doped InN. *Applied Physics Letters* **91**, 111917 (2007).
219. T. Inushima *et al.*, Phonon structure of InN grown by atomic layer epitaxy. *Solid state communications* **110**, 491 (1999).
220. Y. Taniyasu *et al.*, Mg doping for p-type AlInN lattice-matched to GaN. *Applied Physics Letters* **101**, 082113 (2012).
221. O. Bierwagen and J. S. Speck, Mg acceptor doping of In2O3 and overcompensation by oxygen vacancies. *Applied Physics Letters* **101**, 102107 (2012).
222. A. Rose, Space-Charge-Limited Currents in Solids. *Physical Review* **97**, 1538 (1955).
223. M. Lampert, Simplified Theory of Space-Charge-Limited Currents in an Insulator with Traps. *Physical Review* **103**, 1648 (1956).
224. P. Mark and W. Helfrich, Space-Charge-Limited Currents in Organic Crystals. *Journal of Applied Physics* **33**, 205 (1962).
225. W. I. Park *et al.*, Fabrication and electrical characteristics of high-performance ZnO nanorod field-effect transistors. *Applied Physics Letters* **85**, 5052 (2004).
226. A. Motayed *et al.*, Diameter dependent transport properties of gallium nitride nanowire field effect transistors. *Applied Physics Letters* **90**, 043104 (2007).
227. N. Gupta *et al.*, Temperature-dependent electron mobility in InAs nanowires. *arXiv:1210.3665v1, pre-print* (2012).
228. A. A. Talin *et al.*, Unusually Strong Space-Charge-Limited Current in Thin Wires. *Physical Review Letters* **101**, 076802 (2008).
229. A. A. Talin *et al.*, Transport characterization in nanowires using an electrical nanoprobe. *Semiconductor Science and Technology* **25**, 024015 (2010).
230. O. Salehzadeh *et al.*, Rectifying characteristics of Te-doped GaAs nanowires. *Applied Physics Letters* **99**, 182102 (2011).
231. W. Xu *et al.*, Charge transport and trap characterization in individual GaSb nanowires. *Journal of Applied Physics* **111**, 104515 (2012).
232. A. M. Katzenmeyer *et al.*, Observation of Space-Charge-Limited Transport in InAs Nanowires. *IEEE Transactions on Nanotechnology* **10**, 92 (2011).
233. B. S. Simpkins *et al.*, Space-charge-limited currents and trap characterization in coaxial AlGaN/GaN nanowires. *Journal of Applied Physics* **110**, 044303 (2011).

234. M. Millot *et al.*, Determination of effective mass in InN by high-field oscillatory magnetoabsorption spectroscopy. *Physical Review B* **83**, (2011).
235. N. Ma *et al.*, Hole mobility in wurtzite InN. *Applied Physics Letters* **98**, 192114 (2011).
236. T. Nagata *et al.*, Surface structure and chemical states of a-plane and c-plane InN films. *Applied Physics Letters* **95**, 132104 (2009).
237. F. Assad *et al.*, The drift-diffusion equation revisited. *Solid-State Electronics* **42**, 283 (1998).
238. J. B. Schlager *et al.*, Polarization-resolved photoluminescence study of individual GaN nanowires grown by catalyst-free molecular beam epitaxy. *Applied Physics Letters* **88**, 213106 (2006).
239. T. B. Hoang *et al.*, Observation of free exciton photoluminescence emission from single wurtzite GaAs nanowires. *Applied Physics Letters* **94**, 133105 (2009).
240. A. Mishra *et al.*, Polarization and temperature dependence of photoluminescence from zincblende and wurtzite InP nanowires. *Applied Physics Letters* **91**, 263104 (2007).
241. L. V. Titova *et al.*, Temperature dependence of photoluminescence from single core-shell GaAs–AlGaAs nanowires. *Applied Physics Letters* **89**, 173126 (2006).
242. A. Chiari *et al.*, Temperature Dependence of the Photoluminescence in GaAs-GaAlAs Multiple Quantum Well Structures. *Physica Status Solidi (b)* **147**, 421 (1988).
243. S. Breuer *et al.*, Suitability of Au- and self-assisted GaAs nanowires for optoelectronic applications. *Nano letters* **11**, 1276 (2011).
244. D. Y. Song *et al.*, The influence of phonons on the optical properties of GaN. *Journal of Applied Physics* **100**, 113504 (2006).
245. T. Inushima *et al.*, Optical properties of Si-doped InN grown on sapphire (0001). *Physical Review B* **68**, 235204 (2003).
246. A. D. Schricker *et al.*, Space charge limited currents and trap concentrations in GaAs nanowires. *Nanotechnology* **17**, 2681 (2006).
247. Y. Gu and L. J. Lauhon, Space-charge-limited current in nanowires depleted by oxygen adsorption. *Applied Physics Letters* **89**, 143102 (2006).
248. T. D. Moustakas, The role of extended defects on the performance of optoelectronic devices in nitride semiconductors. *Physica Status Solidi (a)* **210**, 169 (2013).
249. X. Duan and C. Stampfl, Defect complexes and cluster doping of InN: First-principles investigations. *Physical Review B* **79**, 035207 (2009).
250. S. A. Dayeh *et al.*, Transport coefficients of InAs nanowires as a function of diameter. *Small* **5**, 77 (2009).
251. G. Kresse and D. Joubert, From ultrasoft pseudopotentials to the projector augmented-wave method. *Physical Review B* **59**, 1758 (1999).
252. J. C. Ho *et al.*, Controlled nanoscale doping of semiconductors via molecular monolayers. *Nature materials* **7**, 62 (2008).

253. D. E. Perea *et al.*, Direct measurement of dopant distribution in an individual vapour-liquid-solid nanowire. *Nature nanotechnology* **4**, 315 (2009).
254. J. E. Allen *et al.*, Nonuniform Nanowire Doping Profiles Revealed by Quantitative Scanning Photocurrent Microscopy. *Advanced Materials* **21**, 3067 (2009).
255. E. Koren *et al.*, Measurement of active dopant distribution and diffusion in individual silicon nanowires. *Nano Letters* **10**, 1163 (2010).
256. P. Xie *et al.*, Diameter-dependent dopant location in silicon and germanium nanowires. *Proceedings of the National Academy of Sciences* **106**, 15254 (2009).
257. M. Fujiwara *et al.*, Dependence of Mg acceptor levels in InN on doping density and temperature. *Journal of Applied Physics* **110**, 093505 (2011).
258. U. Kaufmann *et al.*, Nature of the 2.8 eV photoluminescence band in Mg doped GaN. *Applied Physics Letters* **72**, 1326 (1998).
259. U. Kaufmann *et al.*, Origin of defect-related photoluminescence bands in doped and nominally undoped GaN. *Physical Review B* **59**, 5561 (1999).
260. A. K. Viswanath *et al.*, Magnesium acceptor levels in GaN studied by photoluminescence. *Journal of Applied Physics* **83**, 2272 (1998).
261. M. Leroux *et al.*, Temperature quenching of photoluminescence intensities in undoped and doped GaN. *Journal of Applied Physics* **86**, 3721 (1999).
262. W. C. Ke *et al.*, Photoluminescence properties of self-assembled InN dots embedded in GaN grown by metal organic vapor phase epitaxy. *Applied Physics Letters* **88**, 191913 (2006).
263. R. Kudrawiec *et al.*, Photoreflectance spectroscopy of the band bending and the energy gap for Mg-doped InN layers. *Physica Status Solidi (c)* **6**, S739 (2009).
264. R. Kudrawiec *et al.*, Photoreflectance of InN and InN:Mg layers: An evidence of Fermi level shift toward the valence band upon Mg doping in InN. *Applied Physics Letters* **93**, 131917 (2008).
265. T. Akiyama *et al.*, Structures and electronic states of Mg incorporated into InN surfaces: First-principles pseudopotential calculations. *Physical Review B* **80**, 075316 (2009).
266. J.-H. Song *et al.*, Stabilization of Bulk p-Type and Surface n-Type Carriers in Mg-Doped InN {0001} Films. *Physical Review Letters* **101**, 186801 (2008).
267. X. Duan and C. Stampfl, Nitrogen vacancies in InN: Vacancy clustering and metallic bonding from first principles. *Physical Review B* **77**, 115207 (2008).
268. C. Stampfl *et al.*, Native defects and impurities in InN: First-principles studies using the local-density approximation and self interaction and relaxation-corrected pseudopotentials. *Physical Review B* **61**, r7846 (2000).
269. Z. Zhong *et al.*, Synthesis of p-Type Gallium Nitride Nanowires for Electronic and Photonic Nanodevices. *Nano Letters* **3**, 343 (2003).

270. D. Wang *et al.*, Germanium nanowire field-effect transistors with SiO2 and high-k HfO2 gate dielectrics. *Applied Physics Letters* **83**, 2432 (2003).
271. L. Liao *et al.*, Multifunctional CuO nanowire devices: p-type field effect transistors and CO gas sensors. *Nanotechnology* **20**, 085203 (2009).
272. J.-P. Colinge *et al.*, Nanowire transistors without junctions. *Nature nanotechnology* **5**, 225 (2010).
273. C. Soci *et al.*, Nanowire Photodetectors. *Journal of Nanoscience and Nanotechnology* **10**, 1430 (2010).
274. D. Ahn *et al.*, High performance, waveguide integrated Ge photodetectors. *Optics Express* **15**, 3916 (2007).
275. L. Vivien *et al.*, High speed and high responsivity germanium photodetector integrated in a Silicon-On- Insulator microwaveguide. *Optics Express* **15**, 9843 (2007).
276. L. Colace *et al.*, Ge-on-Si Approaches to the Detection of Near-Infrared Light. *IEEE Journal of Quantum Electronics* **35**, 1843 (1999).
277. L. Colace *et al.*, A Near-Infrared Digital Camera in Polycrystalline Germanium Integrated on Silicon. *IEEE Journal of Quantum Electronics* **43**, 311 (2007).
278. J. Michel *et al.*, High-performance Ge-on-Si photodetectors. *Nature Photonics* **4**, 527 (2010).
279. J. E. Bowers and C. Burrus, Ultrawide-Band Long-Wavelength p-i-n Photodetectors. *Journal of Lightwave Technology* **5**, 1339 (1987).
280. Y. Gao *et al.*, High-Speed Normal-Incidence p-i-n InGaAs Photodetectors Grown on Silicon Substrates by MOCVD. *IEEE Photonics Technology Letters* **24**, 237 (2012).
281. F. E. Ejeckam *et al.*, High-performance InGaAs photodetectors on Si and GaAs substrates. *Applied Physics Letters* **67**, 3936 (1995).
282. M. Herrscher *et al.*, Epitaxial liftoff InGaAs/lnP MSM photodetectors on Si. *Electronics Letters* **31**, 1383 (1995).
283. D. L. Mathine, The Integration of III–V Optoelectronics with Silicon Circuitry. *IEEE Journal of Selected Topics in Quantum Electronics* **3**, 952 (1997).
284. K. Tomioka *et al.*, III–V Nanowires on Si Substrate: Selective-Area Growth and Device Applications. *IEEE Journal of Selected Topics in Quantum Electronics* **17**, 1112 (2011).
285. V. Logeeswaran *et al.*, A Perspective on Nanowire Photodetectors: Current Status, Future Challenges, and Opportunities. *IEEE Journal of Selected Topics in Quantum Electronics* **17**, 1002 (2011).
286. L. Samuelson *et al.*, Semiconductor nanowires for 0D and 1D physics and applications. *Physica E* **25**, 313 (2004).
287. L. J. Lauhon *et al.*, Epitaxial core–shell and core–multishell nanowire heterostructures. *Nature* **420**, 57 (2002).
288. M. S. Gudiksen *et al.*, Growth of nanowire superlattice structures for nanoscale photonics and electronics. *Nature* **415**, 617 (2002).

289. J. Hu *et al.*, Chemistry and Physics in One Dimension: Synthesis and Properties of Nanowires and Nanotubes. *Accounts of Chemial Research* **32**, 435 (1999).
290. Y. Li *et al.*, Nanowire electronic and optoelectronic devices. *Materials Today* **9**, 18 (2006).
291. Y. Huang *et al.*, Nanowires for integrated multicolor nanophotonics. *Small* **1**, 142 (2005).
292. O. Hayden *et al.*, Nanoscale avalanche photodiodes for highly sensitive and spatially resolved photon detection. *Nature materials* **5**, 352 (2006).
293. J. Wang *et al.*, Highly polarized photoluminescence and photodetection from single indium phosphide nanowires. *Science* **293**, 1455 (2001).
294. L. C. Chuang *et al.*, Critical diameter for III-V nanowires grown on lattice-mismatched substrates. *Applied Physics Letters* **90**, 043115 (2007).
295. R. Chen *et al.*, Nanolasers grown on silicon. *Nature photonics* **5**, 170 (2011).
296. J. C. Johnson *et al.*, Single gallium nitride nanowire lasers. *Nature materials* **1**, 106 (2002).
297. M. H. Huang *et al.*, Room-temperature ultraviolet nanowire nanolasers. *Science* **292**, 1897 (2001).
298. Z. Tian *et al.*, Single rolled-up InGaAs/GaAs quantum dot microtubes integrated with silicon-on-insulator waveguides. *Optics Express* **19**, 12164 (2011).
299. Y. J. Lu *et al.*, Plasmonic nanolaser using epitaxially grown silver film. *Science* **337**, 450 (2012).
300. R. F. Oulton *et al.*, Plasmon lasers at deep subwavelength scale. *Nature* **461**, 629 (2009).
301. A. L. Pyayt *et al.*, Integration of photonic and silver nanowire plasmonic waveguides. *Nature nanotechnology* **3**, 660 (2008).
302. E. Ozbay, Plasmonics: merging photonics and electronics at nanoscale dimensions. *Science* **311**, 189 (2006).
303. H. A. Atwater and A. Polman, Plasmonics for improved photovoltaic devices. *Nature Materials* **9**, 205 (2010).